ISSN 1580-2949
UDK 669+666+678+53 MTAEC9, 41(6)255–330(2007)

| MATER. TEHNOL. | LETNIK VOLUME 41 | ŠTEV. NO. 6 | STR. P. 255–330 | LJUBLJANA SLOVENIJA | NOV.-DEC. 2007 |
|---|---|---|---|---|---|

# VSEBINA – CONTENTS

*IZVIRNI ZNANSTVENI ČLANKI – ORIGINAL SCIENTIFIC ARTICLES*

UDK 539.42:539.4:669
Original scientific article/Izvirni znanstveni članek

ISSN 1580-2949
MTAEC9, 41(6)257(2007)

# A NEW VERSION OF THE THEORY OF DUCTILITY AND CREEP UNDER CYCLIC LOADING

## NOVA VERZIJA TEORIJE O DUKTILNOSTI IN LEZENJU PRI CIKLIČNI OBREMENITVI

**Leonid B. Getsov[1], M. G. Kabelevskiy[2]**

[1]St. Petersburg State Technical University, Russia
[2]ZNIITMASh, Moscow, Russia
guetsov@online.ru

*Prejem rokopisa – received: 2007-04-06; sprejem za objavo – accepted for publication: 2007-10-18*

The model of deformation for isotropic metallic materials aimed at obtaining an increased accuracy for forecasting their behavior during complex cyclical loading, in particular cyclic loading where a significant creep role is played in the processes of creep, was developed. As with the majority of models, this new model has applicability limitations and the reliability of use for calculations is acceptable only for cases of small differences in loading from the proportionality.

Key words: metallic materials, cyclic loading, creep deformation, modelling, reliability

Razvit je bil model o deformaciji izotropnih kovinskih materialov s ciljem, da bi se dosegla večja natančnost pri napovedi vedenja pri kompleksni ciklični obremenitvi, še posebej v primeru pomembne vloge procesov lezenja. Kot pri večini modelov ima tudi novi model omejitve pri uporabi in zanesljivost uporabe izračunov je sprejemljiva samo za primer, ko se obremenitev malo odmika od proporcionalnosti.

Ključne besede: kovinski material, ciklična obremenitev, deformacija z lezenjem, modeliranje, zanesljivost, natančnost

## 1 INTRODUCTION

Several models have been developed so far [1], and some of them are in commercial use as software packages, for example, ANSYS, MARC, NASTRAN, ABAQUS, LUSAS, LS-DYNA, COSMOS, ALGOR. However, these models fail to adequately describe the case of complex cyclic loading, when creep processes also play an important role.

In analyzing the lines of access to the development of a theoretical explanation for the straining under cyclic non-isothermal loading, which is necessary for practical calculations of the strain-stressed state (SSS), the authors stood at a crossroads. It was possible to use structural and physical models, which made it possible to describe a wide range of peculiarities of a material's behaviour under complex loading using a rather small number of experimental material parameters [2]. It is worth noting that the deformation and the instantaneous plastic deformations are not separated and their interconnection is included as a property of the developed model. Analogous models have not provided sufficient reliability for a quantitative calculation since the monotonic change in the material properties differs from the experimental values. It was also clear that a modification of the traditional models for plastic flow and the different creep theories, as applied to specific loadings to achieve good accuracy with the calculation, would require a large number of basic experiments to obtain an acceptable fit for a description of real material behaviour. We chose the first solution because of its obvious advantages.

The model of deformation for isotropic metallic materials was designed to make a very accurate prediction of their behavior. This article looks at the case of complex cyclical loading.

## 2 THEORY

1. The variations in non-isothermal theories of plastic flow and of the theory of work hardening during creep will be included in the analysis [3], allowing us to consider the mutual effect of the two forms of deformation within the framework of the traditional approach. In rating the correctness of these proposals, we will start from the necessity of fulfilling the following requirements:

a) a description on a non-isothermal cyclic deformation;
b) a consideration of the cyclic instability of the material properties;
c) a description of the conditions of deformation for complex loading, in particular of alternating sign;
d) a consideration of the mutual influence of time-dependent and time-independent deformation.

The approach based on the separation of irreversible deformation into time-dependent and time-independent has a physical basis.

2. We will assume that the total material deformation consists of the elastic deformation $r_{ij}$, the creep deformations $p_{ij}$, and the plasticity $\varepsilon_{ij}$, [4], thus:

$$e_{ij} = r_{ij} + p_{ij} + \varepsilon_{ij} \quad (1)$$

In the formulation of the rules of deformation we will consider the effect of accumulated plastic deformation

on the creep and of the temperature-time prehistory on the elasto-plastic properties. Although the assumption that only the second invariant of the tensor of stresses enters into the relationship for the increase of the deformation and stresses, it is only a special case of the relationship recommended for the description of the complex stressing of bodies [5]. At present this is a traditional approach. This conclusion is related to the fact that with comparatively small plastic deformations, it provides, as a rule, quite good agreement with experimental data for many cases when plastic deformation occurs during stress that is not very different from the uniaxial.

Having accepted the hypothesis of work hardening that, in particular, means the neglecting of processes of the reverse elastic secondary effect and assuming that the recurrence of loading and preliminary plastic deformation affects only the scalar properties, we may write the equation for creep rate for cyclic loading with an alternating sign:

$$p_{ij}^{(n)} = F(\overline{p}^{(0)}, \overline{p}^{(1)}, \ldots, \overline{p}^{(n)}, \overline{\varepsilon}^{(0)}, \overline{\varepsilon}^{(1)}, \ldots, \ldots, \overline{\varepsilon}^{(n-1)}, \overline{\varepsilon}^{(n)}, \overline{\sigma}, n, T)\frac{S_{ij}}{\overline{\sigma}} \quad (2)$$

Here, $S_{ij}$ are the components of the deviator of the stresses, $\overline{\sigma}$ is the intensity of the stresses, and $\overline{\varepsilon}^{(n)}$ and $\overline{p}^{(n)}$ are the intensities of the plastic deformation and the creep deformation determined from the equations

$$\overline{p}^{(n)} = \int_{t_{n-1}}^{t_n} \left(\frac{2}{3}\dot{p}_{ij}\dot{p}_{ij}\right)^{1/2} \mathrm{d}t \quad (3)$$

$$\overline{\varepsilon}^{(n)} = \int_{t_{n-1}}^{t_n} \left(\frac{2}{3}\dot{\varepsilon}_{ij}\dot{\varepsilon}_{ij}\right)^{1/2} \mathrm{d}t \quad (4)$$

where $n$ is the number of the half cycle

$$p_{ij}\Delta p_{ij} \geq 0 \quad (5)$$

Experiments relating to uniaxial stressing [6] showed that by counting the creep deformations during cyclic loading from the start of a half cycle, the curves of the irreversible deformations accumulated during the non-steady creep are similar to the creep curves for the initial condition. In general, the coefficient of similarity depends on the number of the half cycle, the time, the amount of creep deformation accumulated per half cycle, and the temperature. The rate of steady creep is virtually independent of the number of half cycles.

Comparatively small previous creep and instantaneous plastic deformations 0.2–5.0 % may have a substantial influence on the creep rate. Plastic deformations of the opposite sign accelerate the creep of high-temperature materials of different classes (the Bauschinger effect in creep), while plastic deformations of the same sign can accelerate or retard creep, depending upon their size and the type of material.

In cases when the material is submitted to elasto-plastic steady-stage creep the deformation of the opposite sign, further creep, as a rule, starts with the non-steady stage.

An analysis of the experimental data on cyclic creep makes it possible to select two variations of the concretization of Eq. (2).

The first approach is based on the use of the graph in **Figure 1**, based on the assumption that the effect of plastic deformations on the creep rate may be considered with an appropriate change of the value of creep deformation in the relationship $\dot{p} = f(p,\sigma)$. In this case, in the plastic deformation $\varepsilon_{pl}$ for the total deformation $p$, corresponding to the point $k$, we have a creep rate that corresponds to the point $b$, the point $d$, and not to the point $b$. For $p = 0$ the value of $p$ corresponds to the point $e$.

The material cyclic creep instability will be considered with the use of the function $\varphi$ of the number of cycles [5]. In this case

$$\dot{p} = f(\overline{\overline{p}}, \overline{\sigma}) \quad (6a)$$

Here

$$\overline{\overline{p}} = p + \left[1 - \widetilde{\psi}_1(\overline{\varepsilon}^{+})\widetilde{\psi}_2(\overline{\varepsilon}^{-})\varphi(n, \overline{p}^{(n-1)})\right]\overline{p}_n$$

where $\overline{p}_n$ is the intensity of the creep deformation accumulated as a result of non-steady creep; $\overline{\psi}_1$, $\overline{\psi}_2$, and $\varepsilon$ are functions taking into consideration the effect of plastic deformations and the number of cycles and satisfying the following conditions: for $\overline{\varepsilon}^{+} = 0\ \widetilde{\psi}_1 = 1$; for $\overline{\varepsilon}^{-} = 0\ \widetilde{\psi}_2 = 1$; for $n = 1\ \widetilde{\varphi} = 1$. $\overline{\varepsilon}^{+}$ and $\overline{\varepsilon}^{-}$ are the sum

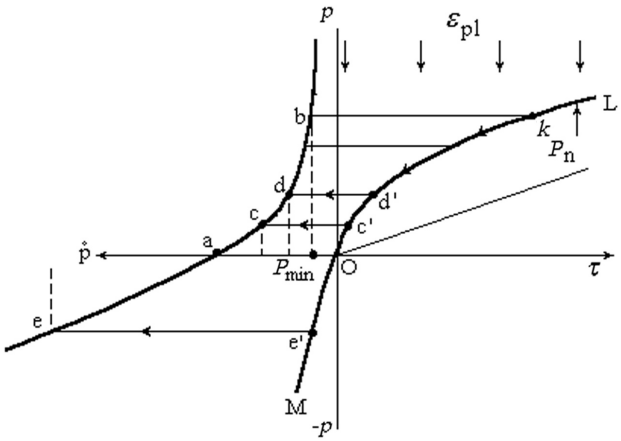


**Figure 1:** Graph for taking into consideration the effect of plastic deformation on the creep rate: OL is the creep curve $p = f(\tau)$; OM is the tangent to the creep curve at $\tau = 0$; a, b are the relations between the creep rate and the accumulated creep deformation; ae is the tangent to the curve ab at the point a; $p_n$ is the creep deformation in the non-steady stage. The arrows show the method of determining the effect of $\varepsilon_{pl}$ on $\dot{p}$.

**Slika 1:** Grafikon za upoštevanje vpliva plastične deformacije na hitrost lezenja. OL-krivulja lezenja $p = f(\tau)$; OM-tangenta na krivuljo lezenja v točki $\tau = 0$; a, b-odnos hitrosti lezenja in nakopičene deformacije z lezenjem; ae-tangenta na krivuljo ab v točki a; $p_n$-deformacija z lezenjem v nestabilnem stanju. Puščice prikazujejo metodo določitve vpliva $\varepsilon_{pl}$ na $\dot{p}$.

of the intensities of the plastic deformations in those half cycles where $\Delta\varepsilon_{ij}^{(n)}\dot{p}_{ij}^{(n)} > 0$ and $\Delta\varepsilon_{ij}^{(n)}\dot{p}_{ij}^{(n)} < 0$;

$$\Delta\dot{\varepsilon}_{ij}^{(n)} = \int_{t_{n-1}}^{t_n} e_{ij}\,\mathrm{d}t \tag{7}$$

The problem of the use of Eq. (6a) is related to the correctness of the extrapolation of the relationship $\dot{p} = f(p,\sigma)$ in the area of negative values of $p$.

The second possible approach to the treatment of existing data provides, as a solution of Eq. (2), the following expression

$$\dot{\overline{p}}^{(n)} = \left[\dot{\overline{p}}_{\min} + \varphi(n,t,\overline{p}^{(n-1)}(p_0 - p_{\min}\right] \tag{6b}$$

where $\dot{\overline{p}}_{\min}$ is the steady-stage creep rate; $\dot{\overline{p}}_{\min} = f(\overline{\sigma},T)$; $\dot{\overline{p}}_0$ is the initial creep rate of the material, calculated according to the theory of work hardening; $\dot{\overline{p}}_0 = f(\overline{\sigma},T,\overline{p})$; $\varphi(n,t,\overline{p}^{(n-1)})$ is a function considering the effect of the number of cycles on the non-steady creep; $\psi_1(\overline{\varepsilon}^+,\tau)$ and $\psi_2(\overline{\varepsilon}^-,\tau)$ are functions considering the effect of plastic deformations; $t$ and $\tau$ are the times counted from the start of the cycle and the moment of the start of the plastic deformation.

The form of the functions $\dot{\overline{p}}_{\min}$ and $\dot{\overline{p}}_0$ may be determined in creep tests under conditions of the uniaxial stressed condition at constant values of the stresses and the temperature.

In Equations (2) and (6) the effect of the temperature at which the instantaneous plastic deformation was accumulated on creep rate is neglected. Such an effect is possible; however, the existing experimental results indicate that it is insignificant.

3. We will describe the instantaneous plastic deformations for non-isothermal cyclic deformation of alternating sign with the incremental theory of thermoplasticity with a **piecewise-spherical** surface [3], modified by applying a relationship for the accumulated creep deformation. Let us assume that the original material is isotropic in the space of the deviators of stresses and it has the paths of the cyclic load for each point of the body given by the cone with a small spatial angle $\alpha$ (**Figure 2**). The area where the vector deviator of stresses during the whole load cycle must be found is cross-hatched.

For the $k$-th half cycle we have

$$f_k = \sqrt{S_{ij}S_{ij}} - r(\overline{\varepsilon}^{(0)},\overline{\varepsilon}^{(1)},\ldots,\overline{\varepsilon}^{(k-1)},\overline{\varepsilon}^{(k)},\ \overline{p}^{(0)},\overline{p}^{(1)},\ldots,\overline{p}^{(k)},k,T) = 0 \tag{8}$$

where the plastic work hardening does not depend on the temperature prehistory. As for creep, the number of the half cycle is increased per unit with a breakdown in the condition

$$\varepsilon_{ij}\Delta\varepsilon_{ij} \geq 0 \tag{9}$$

where

$$\Delta\varepsilon_{ij} = \sqrt{\frac{2}{3}}\Delta\varepsilon\frac{S_{ij}}{R} \tag{10}$$

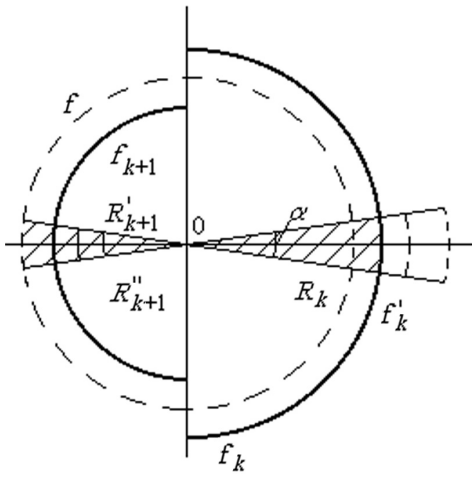


**Figure 2:** Graph of the surface of flow during cyclic loading: f) original surface of flow; $f_k$, $f_{k+1}$) parts of the surface after the $k$-th and the ($k$+1)-th half cycles; $R'_{k+1}$ and $R''_{k+1}$) radius of the surface of flow in the ($k$+1)-th half cycle with the related increase of stresses in the $k$-th half cycle.

**Slika 2:** Grafikon za površino lezenja pri ciklični obremenitvi: f) izvirna površina lezenja; $f_k$, $f_{k+1}$) deli površine po $k$ in ($k$+1) polovičnem ciklu; $R'_{k+1}$ in $R''_{k+1}$) polmer površine lezenja pri ($k$+1) polovičnem ciklu z od njega odvisnim povečanjem napetosti pri $k$ polovičnem ciklu

$\Delta\overline{\varepsilon}$ is the intensity of the increase in deformations.

A determination of the radius of the surface of flow $R$ is significantly easier, applying for the material and temperature $T$, the generalized diagrams of cyclic deformation representing the relationships between the increases in stresses and deformations counted from the start of a given half cycle and independent of the amplitude of the cycle deformation.

If we assume that between the increase of stresses and the accumulation of plastic deformation in a given half cycle at a given temperature and constant values of $\overline{p}$ a single relationship exists, we can determine the value of the radius of the surface of flow as an algebraic sum of its value in the zero half cycle and its increase in the subsequent half cycles:

$$R_k = R_0 + \sum_{i=1}^{k}\Delta R_i \tag{11}$$

The treatment of the results of the experiments made for uniaxial stressing showed that a small creep deformation increases the yield strength of a material in cases when the directions of deformation coincide (**Figure 3**), and decrease it when the directions of deformation in creep and in instantaneous elastoplastic deformation are opposite.

We can assume that the creep deformation $\overline{p}$ influences the value of the radius of the surface of flow by an additional plastic deformation of $\overline{\overline{\varepsilon}} = (\overline{p}/\varepsilon_c)\varepsilon_t$, where $\varepsilon_c$ and $\varepsilon_t$ are the deformation capacity of the material for creep and short-term tension. In this case, the expression for the surface of flow is written in the form:

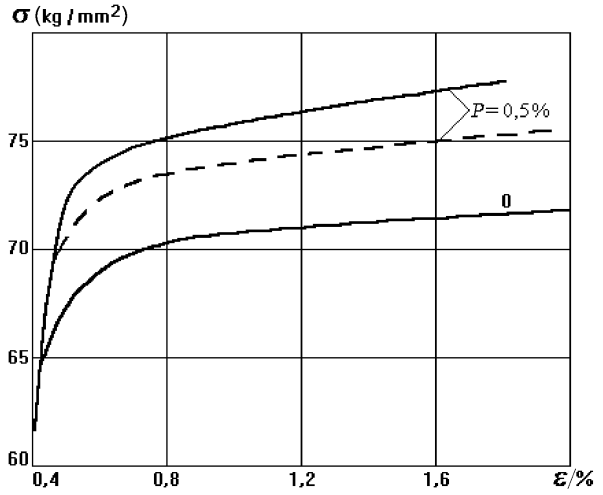


**Figure 3:** Effect of creep on the resistance of 25Kh2M1F steel to instantaneous deformation at 550 °C. Full lines are the experimental results; dashed line is the calculated.

**Slika 3:** Vpliv lezenja na odpornost jekla 25Kh2M1F proti hipni deformaciji pri 550 °C, polne črte – eksperimentalne meritve; črtkane črte – izračunano

$$f_k = \sqrt{S_{ij} S_{ij}} - r\left( \bar{\varepsilon}^{(0)} + \frac{\bar{p}}{\varepsilon_c}\varepsilon_t, \bar{\varepsilon}^{(1)} + \frac{\bar{p}^{(1)}}{\varepsilon_c}\varepsilon_t, \ldots \right.$$
$$\left. \ldots, \bar{\varepsilon}^{(k)} + \frac{\bar{p}^{k}}{\varepsilon_c}\varepsilon_t, k, T \right) = 0 \qquad (12)$$

A comparison of the calculated curve (the dashed line in **Figure 3**) with the experimental (the solid lines) confirms the acceptability of this assumption. (The calculated curve for $p$ = 0,5 % was obtained from the curve for $p$ = 0 by replacement to the left by the value $\varepsilon = (p/\varepsilon_c)\varepsilon_t$.)

This form of surface flow makes it possible to explain, in particular, the phenomenon of plastic deformations for a creep test cycle with alternating sign and stresses lower than the elastic limit of the original material [6].

Equations (1), (6), and (12), the expanded equations of the equilibrium and the consistency of the deformation of uniform medium and also the necessary boundary conditions make it possible to calculate the stressed-strained condition of a body in an arbitrary program of cyclic loading and heating by a step method. At the same time, Eq. (6) and (12) satisfy the requirements given earlier.

It was shown in [7] that the calculation for stresses and deformations during the loading stage may be developed as a solution to the problem of the deformation theory of plasticity with varying the parameters of elasticity [4]. The process of determining successive approximations for the stresses and deformations is carried out with the separation of the deformation into elastic and an increase in the instantaneous plastic deformation and creep according to Eqs. (6) and (12) using the method of successive approximations.

As a parameter of change of materials properties related to its cyclic instability by a change of cyclic loading in place of the number of semi-cycles, the path of cyclic creep, $\lambda_1$, and the path of cyclic plastic deformation $\lambda_2$, should be accepted. Let us assume that the cyclic creep and its increment are determined by the equations:

$$\lambda_1 = \int d\varepsilon_p - \varepsilon_p; d\varepsilon_p = (2/3 \cdot d\varepsilon_{pij} \cdot d\varepsilon_{pij})^{0.5};$$
$$\varepsilon_p = (2/3 \cdot \varepsilon_{pij} \cdot \varepsilon_{pij})^{0.5}$$
$$\lambda_1 = \int dp - p; dp = (2/3 \cdot dp_{pij} \cdot dp_{pij})^{0.5}; \qquad (13)$$
$$p = (2/3 \cdot p_{pij} \cdot p_{pij})^{0.5}$$

$$\Delta\lambda_i = \lambda_i^{(k)} - \lambda_i^{(k-1)} \geq 0 \qquad (14)$$

Here, the following requirements must be met:

$$\frac{\partial\lambda_i^{(k)}}{\partial\tau} > 0 \text{ at } t < t_k \; ; \frac{\partial\lambda_i^{(k)}}{\partial\tau} = 0 \text{ at } t > t_k \qquad (15)$$

By satisfying conditions (14) and (15), the value of n increases by unity.

The increments of the inelastic deformation and the values of the intensity of the inelastic deformation are determined from the equations:

$$d\varepsilon_{ij}^{\aleph} = d\varepsilon_{pij} + dp_{ij}; \; \varepsilon^{\aleph} = (2/3 \cdot \varepsilon_{ij}^{\aleph} \cdot \varepsilon_{ij}^{\aleph})^{0.5}$$

4. An estimation procedure for the material characteristics and design procedure of creep curves for some typical examples of uniaxial loading with cyclic creep at varying temperatures can be applied. The proposed method can be used to calculate the strains at all three stages of creep for heat-resistant steels and alloys with an arbitrary law of change in the stress and temperature at the working temperatures at which the material is structurally stable. The method cannot be used for calculations at the third stage of creep in materials that are fractured after necking or in cases of compression or alternating loading of materials with a highly anisotropic initial creep resistance (in tension and compression).

The duration of the creep process during one cycle may range from a minute to hundreds of hours. In developing the method, we analyzed data on creep and stress relaxation in 20 grades of heat-resistant steels and alloys in a uniaxial stress state.

## 3 COVERNING EQUATIONS

The method is based on a creep theory of the following type [8]

$$\dot{p} = f(\sigma, p, T, \varepsilon_{pl}, \lambda_1) \qquad (17)$$

where $\lambda = \int (|dp| - dp)$ is the path of cyclic creep.

Tests involving a single loading are approximated with the following analytical formula:

$$p = F(\sigma, T, \varepsilon_{pl}, t) \qquad (18)$$

The relation for creep rate in the same tests can be determined by differentiating Eq. (18):

$$\dot{p} = \frac{\mathrm{d}F}{\mathrm{d}t} = \Phi(\sigma,T,\varepsilon_{\mathrm{pl}},t) \tag{19}$$

The behaviour of the material by complex loading programs is assumed to be described by creep theory (17); thus, it is obvious that the required relationship $p = f(\sigma,p,T,\varepsilon_{\mathrm{pl}},\lambda)$ should be obtained by excluding $t$ from Eqs. (18) and (19). However, this cannot be done analytically in a general form with the present form of Eq. (19); it is therefore proposed that in the solution of any specific problem, the value of function [17] should be found numerically by excluding $t$ from Eqs. (18) and (19) at each step of the integration over time. For alternating loading and the absence of instantaneous plastic strains, the specific form of Eq. (18) to describe the creep curves in the first and second stages is:

$$p = A\sigma^k\left[1-\exp(-C\sigma^l t)\right] + B\sigma^m t \tag{20}$$

where $A,B,C,k,l,m$ are coefficients that are constant for a given test temperature. To describe the third creep stage, we replace the stresses in Eq. (20) with the ratio $\sigma/(l - p/\varepsilon_f)$, where $\varepsilon_f$ is the strain at failure.

The change of the creep curve is, for the case of plastic deformation, accounted for by replacing (20) with the expression:

$$p = A\sigma^k\left\{1-\exp\left[(-C\sigma^l(t-t_a)\right]\right\}S(\varepsilon_{\mathrm{pl}}) + B\sigma^m(t-t_a) \tag{21}$$

where $t_a$ is the time to the last plastic deformation. Here, we have in mind, not creep that is accompanied by a continuous change of instantaneous plastic strain, but the effect of discrete instantaneous plastic strain at the moment of the application of the plastic deformation $\varepsilon_{\mathrm{pl}}$.

When the plastic strain $\varepsilon_{\mathrm{pl}}$ is accumulated under stress in creep tests, the effect of $\varepsilon_{\mathrm{pl}}$ is automatically accounted for with the coefficients $A,B,C,k,l,m$.

The values of the function $S$, describing the effect of plastic strain on creep, depend on the sign of $\varepsilon_{\mathrm{pl}}$. The form of the function $S(\varepsilon_{\mathrm{pl}})$ describing the effect of plastic strain on creep rate, dependent on the sign of $\varepsilon_{\mathrm{pl}}$, is determined from a series of tests with different values of $\varepsilon_{\mathrm{pl}}$ and is either specified exactly or given by the approximating function:

$$S(\varepsilon_{\mathrm{pl}}) = 1 + h\varepsilon_{\mathrm{pl}}^q \tag{22}$$

It has been established that the values of the material parameters $h$ and $q$ are slightly dependent on the stress level. The dependence of $\dot{p}$ on the sign of the stresses is taken into account as follows:

$$\dot{p} = f(|\sigma|)\operatorname{sign}\sigma \tag{23}$$

The effect of cyclic loading on the creep rate is considered with inclusion of the function $f_1(\lambda)$ in Eq. (19) as a multiplier:

$$p = A\sigma^k\left\{1-\exp\left[(-C\sigma^l(t-t_a)\right]\right\}\cdot \cdot S(\varepsilon_{\mathrm{pl}})f_1(\lambda) + B\sigma^m(t-t_a) \tag{24}$$

where $t_a$ is the time to the last plastic deformation or to the last change in the stress sign.

The function $f_1(\lambda)$ is determined from tests in cyclic loading with constant cycle parameters: under these conditions, $f_1(\lambda) = f_2(k)$, where $k$ is the number of the cycle. For k = 1, $f_2(k) = f_1(\lambda) = 1$.

Thus, with the chosen test temperatures, $T_i$ ($i$ = 1 ... $N$), we have the following expressions for $p$ and $\dot{p}$:

$$\dot{p} = \left\{A_i C_i\left(\frac{|\sigma|}{1-\frac{|p|}{\varepsilon_{\mathrm{fi}}}}\right)^{k_i+l_i}\exp\left[-C_i\left(\frac{|\sigma|}{1-\frac{|p|}{\varepsilon_{\mathrm{fi}}}}\right)^{l_i}(t-t_a)\right]S(\varepsilon_{\mathrm{pl}},\operatorname{sign}(\varepsilon_{\mathrm{pl}},\sigma))f_1(\lambda) + B_i\left(\frac{|\sigma|}{1-\frac{|p|}{\varepsilon_{\mathrm{fi}}}}\right)^{m_i}\right\}\operatorname{sign}\sigma \tag{25}$$

$$\dot{p} = \left\{A_i\left(\frac{|\sigma|}{1-\frac{|p|}{\varepsilon_{\mathrm{fi}}}}\right)^{k_i}\left\{1-\exp\left[-C_i\left(\frac{|\sigma|}{1-\frac{|p|}{\varepsilon_{\mathrm{fi}}}}\right)^{l_i}(t-t_a)\right]\right\}S(\varepsilon_{\mathrm{pl}},\operatorname{sign}(\varepsilon_{\mathrm{pl}},\sigma))f_1(\lambda) + B_i\left(\frac{|\sigma|}{1-\frac{|p|}{\varepsilon_{\mathrm{fi}}}}\right)^{m_i}\right\}\operatorname{sign}\sigma \tag{26}$$

To find $\dot{p}$ with a known value of $p$ at each step of the integration in accordance with (17), it is necessary to exclude the parameter $t - t_a$ from these equations.

The value of $\dot{p}$ with an arbitrary temperature $T$ is determined by interpolating the values of $\dot{p}$, found using the above-described method with several of the nearest values of $T_i$.

As an additional material parameter we consider the limiting temperature $T_0$: at $\dot{T} \le T_0$, $p = 0$.

If the calculations are performed with a change of sign for the stress $\sigma$ at any number of times (i.e., when the continuous function $\sigma$ passes through zero), the value of $\dot{p}$ changes as follows.

Instead of (17) we have

$$\dot{p} = f(\sigma,p-a,T,\varepsilon_{\mathrm{pl}},\lambda_1) \tag{17a}$$

where $a$ is the creep accumulated up to the moment of the change in the sign of the stresses.

We should additionally assume that for a complex stress state the cyclic loading and the preliminary plastic deformation affects only the scalar properties of the materials. Then, instead of (17) we can write [9]

$$\dot{p}_{ij}^{(n)} = F(\overline{p}^{(0)},\overline{p}^{(1)},\ldots,\overline{p}^{(n-1)},\overline{p}^{(n)},\overline{\varepsilon}^{(0)},\overline{\varepsilon}^{(1)},\ldots, \ldots,\overline{\varepsilon}^{(n-1)},\overline{\varepsilon}^{(n)},\overline{\sigma},\lambda,T)\frac{S_{ij}}{\overline{\sigma}} \tag{27}$$

Here, $S_{ij}$ are the components of the stress deviator; $\overline{\sigma}$ is the stress intensity; $\overline{p}^{(n)}$ and $\overline{\varepsilon}^{(n)}$ are the intensities of the creep strain and (non-creep) plastic strain:

$$\overline{p}^{(n)} = \int_{t_{n-1}}^{t_n}\left(\frac{2}{3}\dot{p}_{ij}\dot{p}_{ij}\right)^{1/2}\mathrm{d}\tau;\ \overline{\varepsilon}^{(n)} = \int_{t_{n-1}}^{t_n}\left(\frac{2}{3}\dot{\varepsilon}_{ij}\dot{\varepsilon}_{ij}\right)^{1/2}\mathrm{d}\tau \tag{28}$$

where $n$ is the number of half-cycles.

## 4 METHOD OF DETERMINING THE MATERIAL'S CHARACTERISTICS

The system of equations (18–20) contains several material constants

$$\begin{array}{ccccccccc} A_1 & B_1 & C_1 & k_1 & l_1 & m_1 & \varepsilon_{p1}(t) & h_1 & q_1 \\ A_2 & B_2 & C_2 & k_2 & l_2 & m_2 & \varepsilon_{p2}(t) & h_2 & q_2 \\ . & . & . & . & . & . & . & . & . \\ A_N & B_N & C_N & k_N & l_N & m_N & \varepsilon_{pN}(t) & h_N & q_N \end{array}$$

$T_0$ and the functions $S[\varepsilon_{pl}, \mathrm{sign}(\varepsilon_{pl},\sigma)]$, $f_1(\lambda)$.

The constants $A_i,B_i,C_i,k_i,l_i,m_i$ are determined from an analysis of the creep data for uniaxial stress in the first and second stages at $N$ temperatures $T_i$ and several (at least six) stresses.

We select three numbers, $a$, $b$ and $c$, determining the first and second creep stages for each experimental creep curve (**Figure 4**).

The data on $a$, $b$ and $c$ for different values of $\sigma$ and $T$ = const are used to find the values of $A$, $B$, $C$, $k$, $l$, $m$, applying the method of least squares and the basis of the following power relations:

$$a = A\sigma^k ; b = B\sigma^k ; c = C\sigma^l \qquad (29)$$

The parameters $h_i$ and $q_i$ of the function $S(\varepsilon_{pl})$ are determined with the analysis of the results of creep tests at $n$ temperatures $T_i$, one stress for each value of $T_i$, and several values of preliminary plastic strain $\varepsilon_{pl}$ within the range from –3 % to –5 % to +3 % to + 5 % (at least three values $\varepsilon_{pl} < 0$, three values $\varepsilon_{pl} > 0$, and $\varepsilon_{pl} = 0$).

For materials with the function $S(\varepsilon_{pl})$ depending on the stress level, it is better if the results of the determination of $S(\varepsilon_{pl})$ are obtained using exact specifications for the values of $S(\varepsilon_{pl},\sigma)$.

The function $f_1(\lambda)$ is found with the analysis of results of the creep tests with alternating loading in the program shown in **Figure 5** and the determination of the dependence on the cycle (the creep strain accumulated within a half-cycle) **Figure 6**.

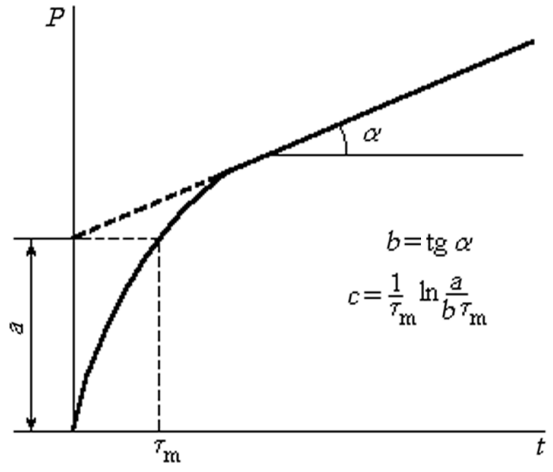


**Figure 4:** Creep curve
**Slika 4:** Krivulja lezenja

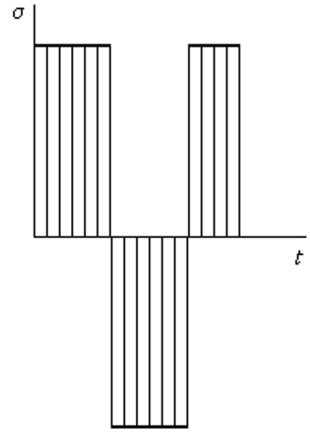


**Figure 5:** Diagram of loading of the specimens
**Slika 5:** Diagram obremenitve preizkušancev

## 5 EXAMPLES OF THE CALCULATION

The values of the coefficients in Eqs. (25) and (26) for the alloy KhN70VMYuT (EI765) are shown in **Table 1**.

The creep strain that occurs with an arbitrary law of change of stress, temperature, and instantaneous plastic strain is determined by the numerical integration of Eqs. (17) and (17a) using the fourth-order Runge-Kutt method and a computer algorithm. The algorithm can be obtained without a computer by using a simple law of

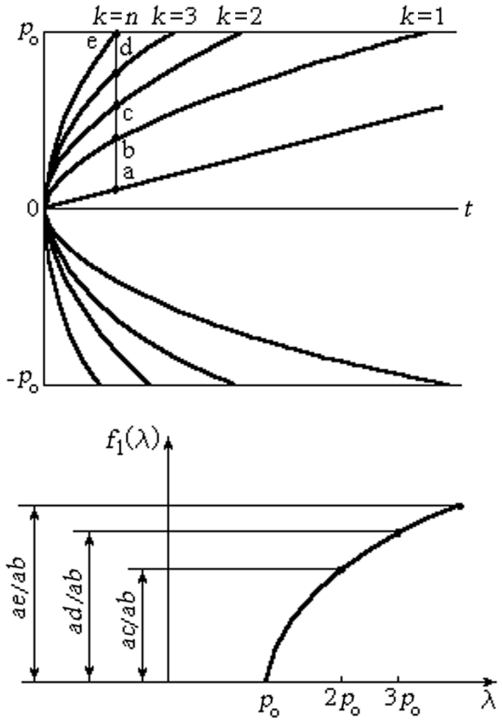


**Figure 6:** Method for determining the function $f_1$ ($\lambda$) from cyclic creep curves.
**Slika 6:** Metoda za določitev funkcije $f_1$ ($\lambda$) iz krivulje cikličnega lezenja

**Table 1:** Parameters of the creep resistance of the alloy EI765
**Tabela 1:** Parametri odpornosti proti lezenju za zlitino E1765

| Temp., $T$/°C | $\varepsilon_n$/% | $\varepsilon_p$/% | $h_1$ | $l_1$ | $f_2(15)$ | $\sigma_y$/(kg/mm$^2$) | Stress level | –lg A | –lg B | –lg C | $k_0$ | $l_0$ | $m$ |
|---|---|---|---|---|---|---|---|---|---|---|---|---|---|
| 650 | 8 | 17 | – | – | – | – | $\sigma < \sigma_y$ | 22,3 | 37,9 | 12,96 | 10,3 | 7,63 | 18,75 |
| 700 | 8-14 | 14 | 26 | 0,5 | – | 64,5 | $\sigma < \sigma_y$ | 13,62 | 16,3 | 9 | 5,56 | 5,92 | 7,41 |
| | | | | | | | $\sigma > \sigma_y$ | 27,7 | 39,2 | 9 | 13,33 | 5,92 | 20 |
| 750 | 13-15 | 16 | 350 | 1,3 | 4 | 55,6 | $\sigma < \sigma_y$ | 5,8 | 16,62 | 2,8 | 1,14 | 2,68 | 8,33 |
| | | | | | | | $\sigma > \sigma_y$ | 18,4 | 28,9 | 2,8 | 8,33 | 2,68 | 15,38 |

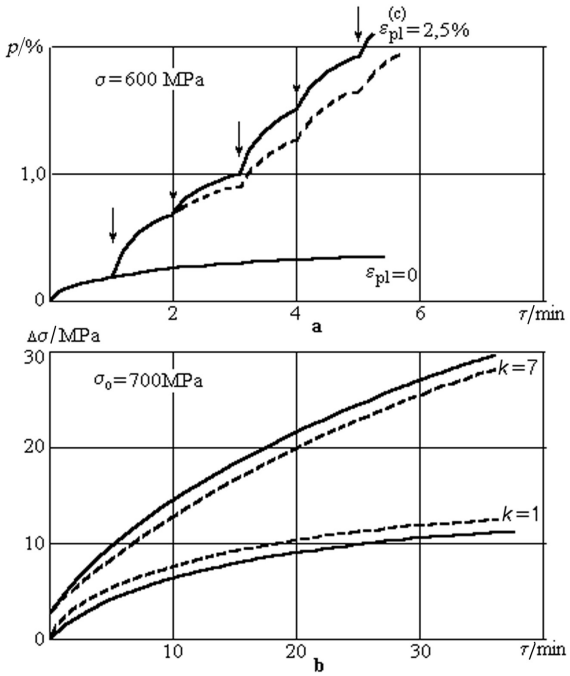


**Figure 7:** Experimental (full lines) and theoretical (dashed lines) curves describing the effect of cyclic plastic deformation on the creep resistance (a) and the relaxation (b) for the alloy EI765 at 700 °C
**Slika 7:** Eksperimentalne (cele črte) in teoretične (črtkane črte) krivulje, ki opisujejo vpliv ciklične plastične deformacije na odpornost proti lezenju (a) in relaksacijo (b) pri 700 °C za zlitino EI765

the change in stress $\sigma(t)$, temperature $T(t)$, and plastic strain $\varepsilon_{pl}(t)$.

As examples of the calculation, the following variants were analysed [6,10]: creep during the first and third stages ($\sigma$ = const, $T$ = const); for a temperature change ($\sigma$ = const); for an alternating stress ($T$ = const); for conditions of cyclic plastic deformation ($\sigma$ = const, $T$ = const); for cyclic creep with alternating plastic strain; with plastic strain and a changing stress ($T$ = const); for alternating stress during a changing temperature. Also, the stress relaxation with $\sigma_0 < \sigma_y$; with $\sigma_0 > \sigma_y$ and additional preliminary plastic deformation; with additional loadings and cyclic plastic strain were examined.

The analysis of the agreement for theoretical and experimental data for twenty different grades of steels and alloys showed that the proposed creep model and the method of determining its parameters were valid (see **Figure 7**, for example).

The studies [11,12] proposed variants of the above method for calculating the creep to determine the stress-strain state of blades (uniaxial stress state) and disks (complex stress state) with multiple starts of gas-turbine engines.

## 6 CONCLUSION

The variations in aniso-thermal theories of plastic flow and of the theory of work hardening in creep with structural parameters have been considered, making it possible to include the mutual effect of two forms of deformations within the framework of the traditional approach.

## 7 REFERENCES

[1] Handbook of Materials Behavior Models. Editor Jean Lemaitre. Academic Press, 2001, 900 p
[2] D. A. Gokhfeld, O. S. Sadakov, The plasticity and creep of elements constructions by repeated loadings (in Russian), Moscow, 1984, 256 p
[3] Yu. N. Rabotnov, Creep problems in structural members, North-Holland, 1969, 750 p
[4] I. A. Birger, B. F. Shorr et al., The high temperature strength of machine parts (in Russian), Mashinostroenie, Moscow, 1975, 454 p
[5] G. S. Pisarenko, A. A. Lebedev, Deformation and strength of materials in the complex stressed condition (in Russian), Naukova Dumka, Kiev, 1976, 415 p
[6] L. B. Getsov, Materials and strength of gas turbine parts (in Russian), M: Nauka, 1996, 591 p
[7] M. G. Kabelevskii, Mechanika. Tverdogo. Tela, (**1972**) 1, 169–174
[8] L. B. Getsov, Strength of materials, (**1978**) 2, 22
[9] L. B. Getsov, M. G. Kabelevskii, Strength of materials, (**1978**) 6, 44
[10] A. M. Borzdyka, L. B. Getsov, Stress relaxation in metals and alloys (in Russian), Metallurgia, Moscow, 1978, 255 p
[11] L. B. Getsov, V. K. Dondoshanskii, Sudovye Energ. Ustanovki, (**1975**) 7, 56
[12] M. G. Kabelevskii, L. B. Getsov, Mashinovedenie, (**1977**) 4, 82

UDK 669'71'3'1:620.17
Original scientific article/Izvirni znanstveni članek

ISSN 1580-2949
MTAEC9, 41(6)265(2007)

# THERMOELECTRICAL PROPERTIES OF A MONOCRYSTALLINE $Al_{64}Cu_{23}Fe_{13}$ QUASICRYSTAL

## TERMOELEKTRIČNE LASTNOSTI MONOKRISTALNEGA KVAZIKRISTALA $Al_{64}Cu_{23}Fe_{13}$

**Igor Smiljanić[1], Ante Bilušić[1,2], Željko Bihar[1], Jagoda Lukatela[1], Boran Leontić[1], Janez Dolinšek[3], Ana Smontara[1]**

[1]Institute of Physics, Bijenička 46, HR-10000 Zagreb, Croatia
[2]Faculty of Natural Sciences, University of Split, N. Tesle 12, HR-21000 Split, Croatia
[3]J. Stefan Institute, Jamova 39, SI-1000 Ljubljana, Slovenia
ismiljanic@ifs.hr

*Prejem rokopisa – received: 2007-07-12; sprejem za objavo – accepted for publication: 2007-08-01*

We performed investigations of the electrical resistivity, thermopower and thermal conductivity of a monocrystalline *i*-$Al_{64}Cu_{23}Fe_{13}$ as well as a polycrystalline *i*-$Al_{63}Cu_{25}Fe_{12}$ icosahedral quasicrystal, for comparison. The electrical resistivity of both samples, the monocrystalline *i*-$Al_{64}Cu_{23}Fe_{13}$ and the polycrystalline *i*-$Al_{63}Cu_{25}Fe_{12}$, exhibits a negative temperature coefficient with $\rho_{4K}$ = 3950 μΩ cm and $\rho_{4K}$= 4900 μΩ cm, and the ratio $\rho_{4K}/\rho_{300K}$ = 1.8, $\rho_{4K}/\rho_{300K}$ = 1.7, respectively. The thermopowers are large and have a negative sign. In addition, the thermopower of the monocrystalline *i*-$Al_{64}Cu_{23}Fe_{13}$ exhibits a sign reversal at $T$ = 278 K. The thermal conductivity is anomalously low, of the order of 1 W/mK at room temperature, with a slightly different temperature variation at low temperatures. On the basis of these results, we concluded that there are no systematic differences between the high-quality monocrystalline and polycrystalline icosahedral *i*-Al-Cu-Fe quasicrystals. Moreover, the reported transport properties of *i*-Al-Cu-Fe appear to be intrinsic to this family of icosahedral quasicrystals.

Keywords: quasicrystals; *i*-AlCuFe, physical properties, resistivity, thermal conductivity

Raziskali smo električno prevodnost, termonapetost in toplotno prevodnost monokristalnega *i*-$Al_{64}Cu_{23}Fe_{13}$ in za primerjavo tudi polikristalnega ikozaedričnega kvazikristala *i*-$Al_{63}Cu_{25}Fe_{12}$. Električna upornost obeh vzorcev ima negativen temperaturni koeficient z $\rho_{4K}$ = 3950 μΩ cm in $\rho_{4K}$ = 4900 μΩ cm, ter razmerje $\rho_{4K}/\rho_{300K}$ = 1.8, $\rho_{4K}/\rho_{300K}$ = 1.7. Termonapetosti so velike in z negativnim predznakom, termonapetost monokristalnega *i*-$Al_{64}Cu_{23}Fe_{13}$ pa ima spremembo predznaka pri $T$ = 278 K. Toplotna prevodnost je anormalno majhna, je reda velikosti 1 W/mK pri sobni temperaturi in z nekoliko drugačno temperaturno odvisnostjo pri nizki temperaturi. Na podlagi rezultatov meritev sklepamo, da ni sistematične razlike med visokokakovostnima monokristalnima in mnogokristalnima ikozaedričnima kvazikristaloma *i*-Al-Cu-Fe. Poleg tega so transportne lastnosti *i*-Al-Cu-Fe značilne za to družino ikozaedričnih kvazikristalov.

Ključne besede: kvazikristali, *i*-AlCuFe, fizikalne lastnosti, upornost, toplotna prevodnost

## 1 INTRODUCTION

The family of icosahedral *i*-Al-Cu-Fe quasicrystals is currently one of the most studied, due to its excellent thermal stability. Most studies reported so far were performed on polycrystalline samples, and include investigations of the electrical resistivity and magnetoresistance,[1-9] thermoelectric power,[9-12] thermal conductivity,[2,9,13] magnetism,[3,8,14] and Hall coefficient.[1,5,7,8] Though polycrystalline samples may acquire quite a high structural perfection through a proper thermal annealing procedure, rapid quenching to room temperature after annealing inevitably results in a strained material that also contains high thermal vacancy concentration for the room temperature conditions (i.e., the quenched-in vacancy concentration is in equilibrium for the much higher temperature of annealing). In addition, grain boundaries may hinder the propagation of electrons and phonons, thus affecting long-range electrical and heat-transport phenomena. In order to test for the true intrinsic properties of *i*-Al-Cu-Fe quasicrystals, it is desirable to compare the physical properties of the polycrystalline material with those measured on high-quality monocrystalline samples, where structural imperfections are largely absent. Therefore, we have performed a study by investigating the electrical resistivity, the thermoelectric power and the thermal conductivity of a monocrystalline *i*-$Al_{64}Cu_{23}Fe_{13}$ and a polycrystalline *i*-$Al_{63}Cu_{25}Fe_{12}$ quasicrystal.

## 2 EXPERIMENTAL PROCEDURE

We investigated two samples with slightly different compositions, a monocrystalline *i*-$Al_{64}Cu_{23}Fe_{13}$ (in the following text abbreviated as *i*-$Al_{64}Cu_{23}Fe_{13}$) and a polycrystalline *i*-$Al_{63}Cu_{25}Fe_{12}$ icosahedral quasicrystal (in the following text abbreviated as *i*-$Al_{63}Cu_{25}Fe_{12}$). The *i*-$Al_{63}Cu_{25}Fe_{12}$ were made from large polycrystalline ingots prepared by conventional casting and subsequent annealing, and it was verified with X-ray diffraction that the samples are single-phase icosahedral. A large monocrystalline *i*-$Al_{64}Cu_{23}Fe_{13}$ quasicrystal was prepared by the Czochralski technique and annealing removed the strains. It has an almost phason-free quasicrystalline structure and shows superior quasicrystallinity on both the macro- and microscopic scales. The samples were

shaped in the form of a prism, with dimensions 3.9 mm × 1.5 mm × 1.4 mm (*i*-$Al_{64}Cu_{23}Fe_{13}$) and 7.2 mm × 1.6 mm × 1.2 mm (*i*-$Al_{63}Cu_{25}Fe_{12}$). The electrical resistivity was measured by a standard four-probe technique with applied currents of 0.1 mA to 1 mA, while the thermoelectric power was measured with respect to high-purity gold lead wires, using a deferential technique. The thermal conductivity was measured using an absolute steady-state heat-flow method. The thermal flux was generated by a 1 kΩ $RuO_2$ chip-resistor glued to one end of the sample, while the other end was attached to a copper heat sink. The temperature gradient across the sample was monitored by a chromel-constantan differential thermocouple.

## 3 RESULTS AND ANALYSIS

### *3.1 Electrical resistivity and thermopower*

The electrical resistivity ($\rho(T)$) and thermopower ($S(T)$) of *i*-$Al_{64}Cu_{23}Fe_{13}$ and *i*-$Al_{63}Cu_{25}Fe_{12}$ were measured in the temperature range from 4 K to 300 K. The results are shown in **Figure 1** and **Figure 2**. The resistivities of *i*-$Al_{64}Cu_{23}Fe_{13}$ and *i*-$Al_{63}Cu_{25}Fe_{12}$ exhibit a negative temperature coefficient, the room temperature values are $\rho_{300K}$ = 2200 μΩ cm and $\rho_{300K}$ = 2900 μΩ cm respectively and the total increases of resistivity is by factors of $R = \rho_{4K}/\rho_{300K} = 1.8$ and $R = \rho_{4K}/\rho_{300K} = 1.7$, respectively. In addition, $\rho(T)$ of the *i*-$Al_{64}Cu_{23}Fe_{13}$ exhibits a weakly pronounced maximum with the peak value $\rho_{300K}$= 4040 μΩcm, at 20 K. The thermopowers $S(T)$ are, in general, large and, in addition, exhibit an interesting feature of a sign reversal (**Figure 2**) in the case of *i*-$Al_{64}Cu_{23}Fe_{13}$. Below 120 K, $S(T)$ is negative with a negative slope, whereas around 120 K it exhibits a minimum and the slope is reversed. Consequently, the

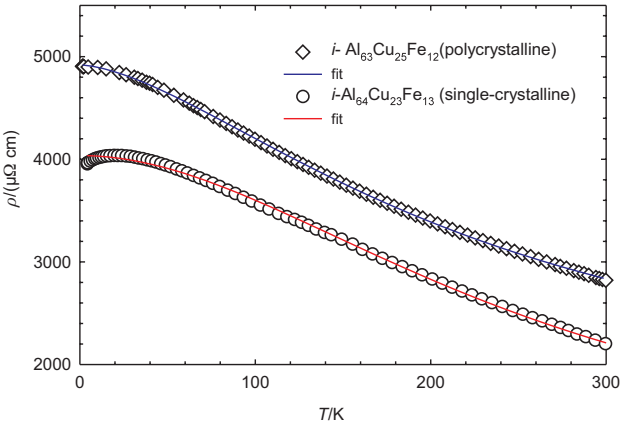


**Figure 1:** Electrical resistivity of the polycrystalline *i*-$Al_{63}Cu_{25}Fe_{12}$ and monocrystalline *i*-$Al_{64}Cu_{23}Fe_{13}$, respectively. The fits (solid lines) of $\rho(T)$ and $S(T)$ were made simultaneously with the Kubo-Greenwood formalism using the spectral resistivity function $\rho(\varepsilon)$.

**Slika 1:** Električna upornost polikristalnega *i*-$Al_{63}Cu_{25}Fe_{12}$ in monokristalnega *i*-$Al_{64}Cu_{23}Fe_{13}$. Približek (cele črte) $\rho(T)$ in $S(T)$ je napravljen istočasno s Kubo-Greenwood formalizmom z uporabo funkcije spektralne upornosti $\rho(\varepsilon)$

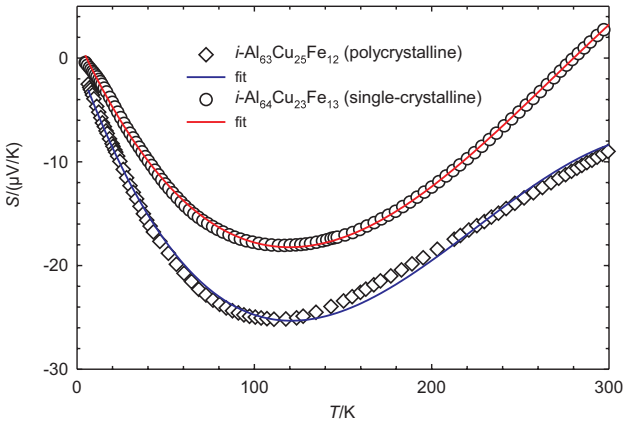


**Figure 2:** Thermopower of the monocrystalline *i*-$Al_{64}Cu_{23}Fe_{13}$ and the polycrystalline *i*-$Al_{63}Cu_{25}Fe_{12}$, respectively. The fits (solid lines) of $\rho(T)$ and $S(T)$ were made simultaneously with the Kubo-Greenwood formalism using the spectral resistivity function $\rho(\varepsilon)$.

**Slika 2:** Termonapetost monokristalnega *i*-$Al_{64}Cu_{23}Fe_{13}$ in polikristalnega *i*-$Al_{63}Cu_{25}Fe_{12}$. Približek (cele črte) za $\rho(T)$ in $S(T)$ je pripravljen istočasno s Kubo-Greenwood formalizmom in z uporabo funkcije spektralne upornosti $\rho(\varepsilon)$

$S(T)$ of *i*-$Al_{64}Cu_{23}Fe_{13}$ changes sign to positive at $T$ = 278 K.

For the analysis of $\rho(T)$ and $S(T)$ we used the spectral resistivity model of Landauro and Solbrig,[11,12,16] where both quantities are analyzed simultaneously by presuming a specific structure- and composition-related form of the energy-dependent spectral resistivity function $\rho(\varepsilon)$ (or its inverse, the spectral conductivity $\sigma(\varepsilon)=1/\rho(\varepsilon)$). Using the Kubo-Greenwood formalism, the temperature-dependent electrical conductivity is calculated according to

$$\sigma(T) = \int \mathrm{d}\varepsilon\sigma(\varepsilon)\left(-\frac{\partial f(\varepsilon, T)}{\partial \varepsilon}\right) \quad (1)$$

whereas the thermopower is obtained from

$$S(T) = -\frac{k_B}{|e|\sigma(T)}\int \mathrm{d}\varepsilon\sigma(\varepsilon)\left(\frac{\varepsilon-\mu(T)}{k_B T}\right)\left(-\frac{\partial f(\varepsilon, T)}{\partial \varepsilon}\right) \quad (2)$$

Here, $f(\varepsilon,T) = \{\exp[(\varepsilon - \mu)/k_BT] + 1\}^{-1}$ is the Fermi-Dirac function and $\mu(T)$ is the chemical potential, which is written in the low-temperature representation as[17]

$$\mu(T) = \varepsilon_F - (k_B T)^2 \frac{\pi^2}{6}\left(\frac{\mathrm{d}\ln n(\varepsilon)}{\mathrm{d}\varepsilon}\right)_{\varepsilon_F} = \varepsilon_F - \xi T^2 \quad (3)$$

The electronic density of states $n(\varepsilon)$ is related to the spectral conductivity via the Einstein relation $\sigma(\varepsilon)=(e^2/V)n(\varepsilon)D(\varepsilon)$ with $D(\varepsilon)$ being the electronic spectral diffusivity. The only material-dependent quantity in **Eqs. (1–3)** is $\sigma(\varepsilon)$, so that a proper model of the spectral conductivity should reproduce both $\sigma(T)$ and $S(T)$ at the same time.

The *ab-initio*-derived spectral resistivity could be modeled by the superposition of two Lorentzians

$$\rho(\varepsilon) = A\left\{\left[\frac{1}{\pi}\frac{\gamma_1}{(\varepsilon-\delta_1)^2+\gamma_1^2}\right]+\alpha\left[\frac{1}{\pi}\frac{\gamma_2}{(\varepsilon-\delta_2)^2+\gamma_2^2}\right]\right\} \quad (4)$$

where $1/\pi\gamma_i$ is the height of a Lorentzian, $2\gamma_i$ its FWHM, $\delta_i$ its position with respect to the Fermi energy $\varepsilon_F$ (taken to be at the origin of the energy scale; $\varepsilon_F = 0$) and $\alpha$ is the relative weight of the Lorentzians. The position of the narrow resistivity peak with respect to the Fermi energy $\varepsilon_F$ is responsible for the anomalous electronic transport properties. As this peak is due to a specific distribution of Fe atoms in the structure, quasiperiodicity alone cannot account for the anomalous transport properties of *i*-Al-Cu-Fe quasicrystals; a right chemical decoration is also needed. The Fermi energy can be shifted on the scale of a few 100 meV by deviations in the stoichiometry and/or by defects in both structure and chemical decoration,[18,19] so that the relative position of the narrow peak can change on this energy scale in samples of slightly different composition and annealing treatment. Consequently, solely on the basis of small shifts of $\varepsilon_F$, the thermopower of *i*-Al-Cu-Fe samples of similar composition can switch between large positive and large negative values and it may also change sign with temperature, as demonstrated for the *i*-$Al_{62}Cu_{25.5}Fe_{12.5}$ polycrystalline sample.[9,10,12] The fits of the experimental $\rho(T)$ and $S(T)$ data were performed simultaneously with **Eqs. (1-4)** by adjusting the set of parameters ($A$, $\alpha$, $\delta_1$, $\delta_2$, $\gamma_1$ and $\gamma_2$) pertinent to the shape of the spectral resistivity $\rho(\varepsilon)$. The starting value of the parameter $\xi$ entering the temperature-dependent chemical potential of **Eq. (3)** was determined by recognizing that in the case when the spectral variation of the electronic diffusivity can be neglected, one can replace $n(\varepsilon)$ by $\sigma(\varepsilon)$ in **Eq. (3).** The initial value was obtained by using the Mott formula

$$S^{\mathrm{Mott}}(T) = \frac{\pi^2}{3}\frac{k_B^2}{|e|}\left(\frac{\mathrm{d}\ln\sigma(\varepsilon)}{\mathrm{d}\varepsilon}\right)_{\varepsilon_F} T$$

so that $\xi = -0.5|e|(S^{\mathrm{Mott}}(T)/T)$. The fits are shown as solid lines in **Figure 1** and **Figure 2;** the fit parameters are collected in **Table 1.** The fits of both $\rho(T)$ and $S(T)$ are excellent in the whole investigated temperature range.

The magnitude of the electrical resistivity of the monocrystalline *i*-$Al_{64}Cu_{23}Fe_{13}$ is in-line with the values reported for the polycrystalline *i*-Al-Cu-Fe. In polycrystalline *i*-Al-Cu-Fe the total variation of $\rho(T)$ over the relevant Fe range is merely a factor of two,[5] so that the material is best classified as a semi-metal over the whole icosahedral concentration range with no indication of a large resonant increase of the resistivity. The $\rho_{4K}$ resistivity value of our *i*-$Al_{64}Cu_{23}Fe_{13}$ matches well with that of the polycrystalline samples from the study[5] with the same Fe concentration. However, since the Fermi energy of our *i*-$Al_{64}Cu_{23}Fe_{13}$ is located nearly at the maximum of the spectral resistivity[20], further shifts of $\varepsilon_F$ over the resistivity peak due to a small variation of the Fe composition would not result in an additional increase of the resistivity, but can only make it smaller. This hints that the factor-of-two larger peak resistivity of the polycrystalline *i*-Al-Cu-Fe material at the Fe 12.5 % concentration,[5] as compared to the monocrystalline *i*-$Al_{64}Cu_{23}Fe_{13}$, could originate in extrinsic factors like grain boundaries and other lattice imperfections that act as additional scattering centers for the conduction electrons.

### *3.2 Thermal conductivity*

The measured thermal conductivities $\kappa$(T) of *i*-$Al_{64}Cu_{23}Fe_{13}$ and *i*-$Al_{63}Cu_{25}Fe_{12}$ are displayed in **Figure 3**. The conductivity value at room temperature of *i*-$Al_{64}Cu_{23}Fe_{13}$ amounts $\kappa_{300K}$ = 1.7W/mK, whereas in the case of the *i*-$Al_{63}Cu_{25}Fe_{12}$ is $\kappa_{300K}$ = 2.9 W/mK. These values are surprisingly low for an alloy of regular metals and are comparable to the thermal conductivities of known thermal insulators, amorphous fused silica[21] and the technologically widespread thermally insulating material, yttrium-doped zirconia ceramics[22]. The $\kappa(T)$ data were analyzed with a semi-quantitative model, appropriate for icosahedral quasicrystals and their approximants[22-29]. The thermal conductivity parameter $\kappa(T)$ is divided into three terms

**Table 1:** Parameters of the spectral resistivity $\rho(\varepsilon)$ of **Eq. (4)**, obtained from the simultaneous fits of $\rho(T)$ and $S(T)$ for *i*-$Al_{64}Cu_{23}Fe_{13}$ (monocrystalline) and *i*-$Al_{63}Cu_{25}Fe_{12}$ (polycrystalline)

**Tabela 1:** Parameter posebne upornosti $\rho(\varepsilon)$ enačba **(4)**, določen z istočasnim približkom $\rho(T)$ in $S(T)$ za *i*-$Al_{64}Cu_{23}Fe_{13}$ (monokristalen) in *i*-$Al_{63}Cu_{25}Fe_{12}$ (polikristalen)

| sample Al-Cu-Fe | $A$/(μΩ cm eV) | $d_1$/(meV) | $\gamma_1$/(meV) | $\alpha$ | $\delta_2$/(meV) | $\gamma_2$/(meV) |
|---|---|---|---|---|---|---|
| mono-crystalline | 392 | –43 | 241 | 1.13 | –9 | 38 |
| polycrystalline | 847 | –5.2 | 587 | 1.07 | –16 | 55 |

**Table 2:** Fit parameters of the thermal conductivity $\kappa(T)$ *i*-$Al_{64}Cu_{23}Fe_{13}$ (monocrystalline) and *i*-$Al_{63}Cu_{25}Fe_{12}$ (polycrystalline), respectively

**Tabela 2:** Parametri približka toplotne prevodnosti $\kappa(T)$ za *i*-$Al_{64}Cu_{23}Fe_{13}$ (monokristalen) in *i*-$Al_{63}Cu_{25}Fe_{12}$ (polikristalen)

| sample Al-Cu-Fe | $L_{\mathrm{eff}}$ | $\kappa_H^0$(W/mK) | $E_a$/(meV) | $A$/($s^{-1}K^{-2}$) | $B$/($s^{-1}K^{-4}$) | $\beta$ |
|---|---|---|---|---|---|---|
| mono-crystalline | 2.1 | 0.7 | 6.3 | $1.2x10^7$ | $2.8x10^4$ | 3.2 |
| polycrystalline | 2.5 | 2.2 | 16.2 | $3.5 x 10^6$ | $7.2 x 10^3$ | 2.0 |

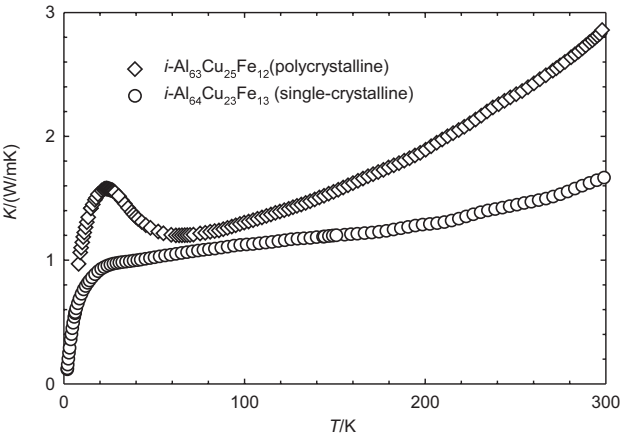


**Figure 3:** Thermal conductivity $\kappa(T)$ of the monocrystalline $i$-$Al_{64}Cu_{23}Fe_{13}$ and the polycrystalline $i$-$Al_{63}Cu_{25}Fe_{12}$ , respectively
**Slika 3:** Toplotna prevodnost $\kappa(T)$ za monokristalni $i$-$Al_{64}Cu_{23}Fe_{13}$ in polikristalni $i$-$Al_{63}Cu_{25}Fe_{12}$

$$\kappa(T) = \kappa_{el}(T) + \kappa_D(T) + \kappa_H(T) \quad (5)$$

The electronic contribution $\kappa_e$ is obtained using the empirical Wiedemann-Franz law ($\kappa_{el}=L_o\sigma T$) with a temperature-dependent effective Lorenz number

$$L(T) = \frac{\kappa_{el}(T)}{T \times \sigma(T)} \quad (6)$$

The lattice contribution ($\kappa - \kappa_{el}$) is analyzed by considering (i) the propagation of long-wavelength acoustic phonons (for which the quasicrystal structure is an elastic continuum) within the Debye model and (ii) hopping of localized vibrations within the icosahedral cluster substructure, which participate in the heat transfer via thermally activated hopping. In the simplest model, the hopping of localized vibrations is described by a single activation energy $E_a$, yielding a contribution to the thermal conductivity

$$\kappa_H = \kappa_H^0 \exp\left(\frac{-E_a}{k_B T}\right) \quad (7)$$

where $\kappa_H^0$ is a constant. The Debye thermal conductivity is written as[30]

$$\kappa_D = C_D T^3 \int_0^{\theta_D/T} \tau(x) \frac{x^4 e^x}{(e^x - 1)^2} dx \quad (8)$$

where $C_D = k_B^4/2\pi^2 \bar{v}\hbar^3$, $\bar{v}$ is the average sound velocity, $\theta_D$ the Debye temperature, $\tau$ the phonon relaxation time and $x = \hbar\omega/k_B T$, where $\hbar\omega$ is the phonon energy. The different phonon-scattering processes are incorporated into the relaxation time $\tau(x)$ and we assume that Matthiessen's rule is valid, $\tau^{-1} = \sum \tau_j^{-1}$, where $\tau_j^{-1}$ is the scattering rate related to the $j$-th scattering channel. In analogy with the Al-Pd-Mn approximant and quasicrystal phases,[24,25,30] we consider two dominant scattering processes in the investigated temperature range: (1) the scattering of phonons on structural defects of stacking-fault type with the scattering rate $\tau_{sf}^{-1} = Ax^2T^2$ and (2) *umklapp* processes with the phenomenological form of the scattering rate pertinent to quasicrystals,[23,24,29] $\tau_{um}^{-1} = Bx^{\beta}T^{4-\beta}$, so that $\tau^{-1} = \tau_{sf}^{-1} + \tau_{um}^{-1}$. The Debye temperature of $i$-Al-Cu-Fe was estimated from the specific heat[32] as $\theta_D \approx 560$ K and the Debye constant $C_D$ was determined from ultrasonic data[30]. The fits (solid lines in **Figure 4**) are excellent and the fit parameters are collected in **Table 2**. The electronic ($\kappa_{el}$), Debye ($\kappa_D$) and hopping ($\kappa_H$) contributions are shown separately on the graph. The temperature-dependent effective Lorenz number $L(T)$ of $i$-$Al_{64}Cu_{23}Fe_{13}$ and $i$-$Al_{63}Cu_{25}Fe_{12}$ deviates considerably from the Wiedemann-Franz value $L_0$, amounting $L/L_0$= 2.1 and $L/L_0$= 2.5 at 300 K, respectively, and the electrons carry around 40 % of the total heat in both cases. The Debye contribution exhibits a maximum at about 30 K and declines above this temperature, whereas the hopping contribution becomes significant at elevated temperatures. The activation energy for the hopping of $i$-$Al_{64}Cu_{23}Fe_{13}$ and $i$-$Al_{63}Cu_{25}Fe_{12}$ was determined as $E_a \approx 16$ meV and $E_a \approx 16$ meV, respectively. These energies correlate with the inelastic neutron and X-ray scattering experiments on $i$-Al-Pd-Mn quasicrystals, where dispersionless vibrational states were identified for energies higher than 12 meV. Such dispersionless states indicate localized vibrations and are considered to be a consequence of a dense distribution of energy gaps in the phonon excitation spectrum of quasicrystals. The parameters $B$ and $\beta$ define phonon scattering by *umklapp* processes in a phenomenological way. The fit-determined $\beta = 3.2$ value for $i$-$Al_{64}Cu_{23}Fe_{13}$ yields

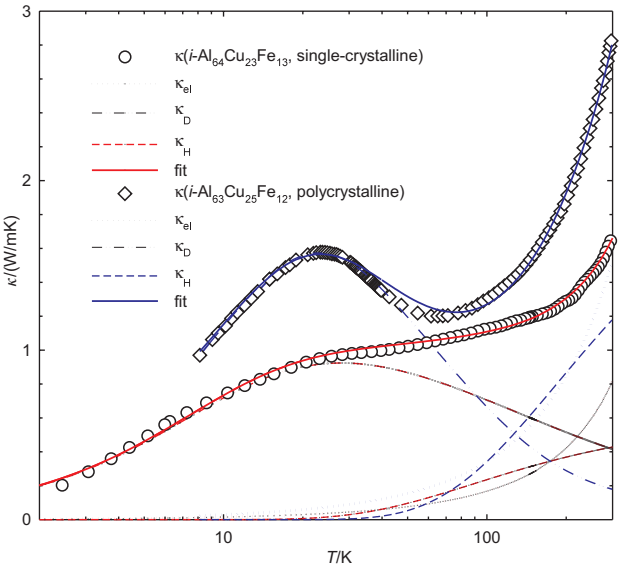


**Figure 4:** Thermal conductivity $\kappa(T)$ with the fits to the total $\kappa(T)$, of the monocrystalline $i$-$Al_{64}Cu_{23}Fe_{13}$ and the polycrystalline $i$-$Al_{63}Cu_{25}Fe_{12}$. The three contributions to the total $\kappa(T)$, electronic $\kappa_{el}$, Debye $\kappa_D$ and hopping $\kappa_H$, are shown separately
**Slika 4:** Toplotna prevodnost $\kappa(T)$ s približkom za skupen $\kappa(T)$, za monokristalni $i$-$Al_{64}Cu_{23}Fe_{13}$ in za polikristalni $i$-$Al_{63}Cu_{25}Fe_{12}$. Posebej so prikazani trije prispevki k skupni $\kappa(T)$, elektronski $\kappa_{el}$, Debye $\kappa_D$ in preskočna $\kappa_H$

the frequency- and temperature dependence of the *umklapp* term $\tau_{um}^{-1} \propto \omega^{3.2} T^{0.8}$ and indicates similarity with the modified quasi-umklapp scattering rate $\tau_{um}^{-1} \propto \omega^3 T$, used for the analysis of the thermal conductivity of *i*-Zn-Mg-Y quasicrystals, while for the polycrystalline sample, the fit-determined $\beta = 2.0$ $\tau_{um}^{-1} \propto \omega^2 T^2$ indicates the quasi-umklapp scattering rate obtained for the *i*-Al-Pd-Mn quasicrystals[25,29]. Here it should be mentioned that the Debye and hopping contributions slightly compensate for each other in the fit procedure, so that the parameter values characterizing $\kappa_D$ and $\kappa_H$ should be considered at the qualitative level.

Regarding the comparison of the thermal conductivity of monocrystalline and polycrystalline *i*-Al-Cu-Fe, we are not aware of other quantitative analyses of $\kappa(T)$ of polycrystalline samples in the sense of **Eqs. (5–8),** so that the comparison has to be made at the level of experimental thermal conductivities. The room-temperature value for *i*-$Al_{64}Cu_{23}Fe_{13}$ amounts to $\kappa_{300K} = 1.7$ W/mK, whereas for the *i*-$Al_{63}Cu_{25}Fe_{12}$ it is $\kappa_{300K} = 2.9$ W/mK. Though the scatter of the known values of thermal conductivity of *i*-Al-Cu-Fe[34] is relatively large, there seems to be no systematic difference between the polycrystalline and monocrystalline samples.

## 4 CONCLUSION

We performed investigations of electrical resistivity, thermoelectric power and thermal conductivity on a monocrystalline *i*-$Al_{64}Cu_{23}Fe_{13}$ and a polycrystalline *i*-$Al_{63}Cu_{25}Fe_{12}$ icosahedral quasicrystal, for comparison. The electrical resistivity and thermopower analysis shows that the Fermi energy is located at the minimum of the pseudogap in the spectral conductivity $\sigma(\varepsilon)$. All this gives evidence that we are dealing with icosahedral quasicrystal samples of exceptional quality, so that its physical properties may be considered as intrinsic to the *i*-Al-Cu-Fe phase. A comparison of the investigated monocrystalline *i*-$Al_{64}Cu_{23}Fe_{13}$ to the polycrystalline *i*-$Al_{63}Cu_{25}Fe_{12}$, however, shows that there are no pronounced differences between the two forms of the material. While there are essentially no differences in the magnetic properties of the monocrystalline and polycrystalline materials, the electrical resistivity of the polycrystalline material is larger by a factor of two. This difference can be easily accounted for by the grain boundaries and other lattice imperfections that act as additional scattering centers for the conduction electrons. Comparing the thermopowers of the monocrystalline and polycrystalline *i*-Al-Cu-Fe materials, in general, the *S*(T) magnitude and temperature dependence depend strongly on the position of $\varepsilon_F$ relative to the spectral resistivity peak, so that slight differences in the samples' stoichiometry and structural perfection may lead to very different thermopowers in both magnitude and sign. A quantitative comparison of the thermal conductivities of monocrystalline and polycrystalline *i*-Al-Cu-Fe is less straightforward due to the random scatter of the reported values, but $\kappa_{300K}$ of the monocrystalline *i*-$Al_{64}Cu_{23}Fe_{13}$ fits within the range of values for the polycrystalline *i*-$Al_{63}Cu_{25}Fe_{12}$. To conclude, we found no systematic differences in the electrical resistivity, thermoelectric power and thermal conductivity between the high-quality monocrystalline and polycrystalline *i*-Al-Cu-Fe quasicrystals, and the reported physical properties of the other *i*-Al-Cu-Fe quasicrystals appear to be intrinsic to this family of icosahedral quasicrystals.

## Acknowledgements

We would like to thank Y. Yokoyama and Y. Calvayrac for giving us the samples of monocrystalline *i*-$Al_{64}Cu_{23}Fe_{13}$ and polycrystalline *i*-$Al_{63}Cu_{25}Fe_{12}$ icosahedral quasicrystal, respectively. This work was done within the activities of the 6th Framework EU Network of Excellence "Complex Metallic Alloys" (Contract No. NMP3-CT-2005-500140), and has been supported in part by the Ministry of Science, Education and Sports of Republic of Croatia through the Research Projects Nos. 035-0352826-2848 and 177-0352828-0478.

## 5 REFERENCES

[1] T. Klein, A. Gozlan, C. Berger, F. Cyrot-Lackmann, Y. Calvayrac, A. Quivy, Europhys. Lett. 13 (**1990**), 129–134
[2] A. Smontara, J.C. Lasjaunias, C. Paulsen, A. Bilušić, Y. Calvayrac, Mat. Sci. Eng. 294-296 (**2000**), 706–710
[3] T. Klein, C. Berger, D. Mayou, F. Cyrot-Lackmann, Phys. Rev. Lett. 66 (**1991**), 2907–2910
[4] T. Klein, H. Rakoto, C. Berger, G. Fourcaudot, F. Cyrot-Lackmann, Phys. Rev. B 45 (**1992**), 2046–2049
[5] P. Lindqvist, C. Berger, T. Klein, P. Lanco, F. Cyrot-Lackmann, Y. Calvayrac, Phys. Rev. B 48 (**1993**), 630–633
[6] D. Mayou, C. Berger, F. Cyrot-Lackmann, T. Klein, P. Lanco, Phys. Rev. Lett. 70 (**1993**), 3915–3918
[7] M. Ahlgren, P. Lindqvist, M. Rodmar, Ö. Rapp, Phys. Rev. B 55 (**1997**), 14847–14854
[8] R. Escudero, J. C. Lasjaunias, Y. Calvayrac, M. Boudard, J. Phys.: Condens. Matter 11 (**1999**), 383–404
[9] A. Bilušić, A. Smontara, J.C. Lasjaunias, J. Ivkov, Y. Calvayrac, Mat. Sci. Eng. 294-296 (**2000**), 711–714
[10] A. Bilušić, I. Bešlić, J. Ivkov, J.C. Lasjaunias, A. Smontara, Fizika A (Zagreb) 8 (**2000**), 183–194
[11] C.V. Landauro, H. Solbrig, Mat. Sci. Eng. A 294-296 (**2000**), 600–603
[12] H. Solbrig, C.V. Landauro, Quasicrystals, Structure and Physical Properties, Wiley-VCH, Weinheim 2003, 254
[13] A. Perrot, J.M. Dubois, M. Cassart, J.P. Issi, Proc. of the 5th Inter. Conf. on Quasicrystals, World Scientific, Singapore, 1995, 588–601
[14] K. Fukamichi, Physical Properties of Quasicrystals, Springer, New York 1999, p. 295 and references therein
[15] Y. Yokoyama, Y. Matsuo, K. Yamamoto, K. Hiraga, Mater. Trans., JIM, 43 (**2002**), 762–765
[16] C. V. Landauro, H. Solbrig, Physica B 301 (**2001**), 267–275

[17] N. W. Aschroft, N. D. Mermin, Solid State Physics, Saunders College Publishing, London 1976, 46
[18] F. S. Pierce, P. A. Bancel, B. D. Biggs, Q. Guo, S. J. Poon, Phys. Rev. B 47 (**1993**), 5670–5676
[19] H. Solbrig, C. V. Landauro, A. Löser, Mat. Sci. Eng. A 294–296 (2000), 596–599
[20] J. Dolinšek, S. Vrtnik, M. Klanjšek, Z. Jagličić, A. Smontara, I. Smiljanić, A. Bilušić, Y. Yokoyama, A. Inoue, C.V. Landauro, Phys. Rev. B (in press)
[21] D.-M. Zhu, Phys. Rev. B 50 (**1994**), 6053–6056
[22] R. Mévrel, J.-C. Laizet, A. Azzopardi, B. Leclercq, M. Poulain, O. Lavigne, D. Demange, J. Eur. Cer. Soc. 24 (**2004**), 3081–3089
[23] Ž. Bihar, A. Bilušić, J. Lukatela, A. Smontara, P. Jeglič, P. J. McGuiness, J. Dolinšek, Z. Jagličić, J. Janovec, V. Demange, J. M. Dubois, J. Alloys Compd. 407 (**2006**), 65–73
[24] J. Dolinšek, P. Jeglič, P. J. McGuiness, Z. Jagličić, A. Bilušić, Ž. Bihar, A. Smontara, C.V. Landauro, M. Feuerbacher, B. Grushko, K. Urban, Phys. Rev. B 72 (**2005**), 064208–11
[25] A. Bilušić, A. Smontara, J. Dolinšek, P. J. McGuiness, H. R. Ott, J. Alloys Compd. 432 (**2007**), 1–6
[26] A. Smontara, I. Smiljanić, A. Bilušić, Z. Jagličić, M. Klanjšek, S. Roitsch, J. Dolinšek, M. Feuerbacher, J. Alloys Compd. 430 (**2007**) 29–38
[27] A. Smontara, I. Smiljanić, A. Bilušić, B. Grushko, S. Balanetskyy, Z. Jagličić, S. Vrtnik, J. Dolinšek , J. Alloys Compd., in press
[28] J. Dolinsek, T. Apih, P. Jeglic, I. Smiljanic, A. Bilusic, Ž . Bihar, A. Smontara, Z. Jaglicic, M. Heggen, M. Feuerbacher, Intermetallics 15 (**2007**) 1367–1376
[29] A. Bilušić, Ž. Budrović, A. Smontara, J. Dolinšek, P. C. Canfield., I. R, Fisher, J. Alloys Compd. 342 (2002), 413–415
[30] R. Berman, Thermal Conduction in solids, Clarendon Press, Oxford 1978, 23
[31] P. A. Kalugin, M. A. Chernikov, A. Bianchi, H. R. Ott, Phys. Rev. B 53 (**1996**), 14145–14151
[32] J. C. Lassjaunias, Y. Calvayrac, H. Yang, J. Physique 17 (**1997**), 959–976
[33] Y. Amazit, M. de Boissieu, A. Zarembowitch, Europhys. Lett. 20 (**1992**), 703–706
[34] A. Bilušić, D. Pavuna, A. Smontara, Vacuum 61 (**2001**), 345–348

UDK 669.71'3'1:620.18
Original scientific article/Izvirni znanstveni članek

ISSN 1580-2949
MTAEC9, 41(6)271(2007)

# FAZE V KVAZIKRISTALNI ZLITINI $Al_{64,4}Cu_{22,5}Fe_{13,1}$

## PHASES IN A QUASICRYSTALLINE ALLOY $Al_{64,4}Cu_{23,5}Fe_{13,1}$

**Tonica Bončina[1], Boštjan Markoli[2], Ivan Anžel[1], Franc Zupanič[1]**

[1]Univerza v Mariboru, Fakulteta za strojništvo, Smetanova 17, SI-2000 Maribor, Slovenija
[2]Univerza v Ljubljani, Naravoslovnotehniška fakulteta, Aškerčeva 12, SI-1000 Ljubljana, Slovenija
tonica.boncina@uni-mb.si

*Prejem rokopisa – received: 2007-09-24; sprejem za objavo – accepted for publication: 2007-10-18*

V ternarnem sistemu Al-Cu-Fe se pojavlja t. i. *i*-faza (ikozaedrični kvazikristal), ki je termodinamsko ravnotežna faza in s tem sestavni del ravnotežnega faznega diagrama. Na enofazno področje *i*-faze meji veliko število intermetalnih faz, ki so lahko glede na sestavo zlitine, razmere pri strjevanju in toplotni obdelavi v stabilnem ali metastabilnem ravnotežju z *i*-fazo. Sinteza enofazne kvazikristalne zlitine je mogoča samo v ozkem koncentracijskem območju in pri primernem načinu toplotne obdelave, zato je poznanje in ugotavljanje faz ključnega pomena. V raziskavi smo izdelali zlitino $Al_{64,4}Cu_{22,5}Fe_{13,1}$ in vzorce toplotno obdelali na različne načine. Posamezne faze in druge mikrostrukturne značilnosti smo ugotovili z ustrezno metalografsko pripravo vzorcev in metodami svetlobne mikroskopije (SM), vrstične elektronske mikroskopije (SEM), mikrokemične analize (EDS), rentgenske fazne analize (XRD), presevne elektronske mikroskopije (TEM) ter z merjenjem mikrotrdote. Faze smo ločevali tudi glede na njihovo morfologijo in mikrotrdoto (nanoidentifikacija). Prisotnost *i*-faze smo potrdili z metodama XRD in TEM.

Ključne besede: Al-Cu-Fe, kvazikristal, metalografija

In the ternary system Al-Cu-Fe an *i*-phase (icosahedral quasicrystal) is present. It is thermodynamically stable and a part of the equilibrium phase diagram. However, according to the chemical composition and conditions during the solidification and heat treatment, a considerable number of intermetallic phases can be in stabile or metastabile equilibrium with the *i*-phase. Consequently, synthesis of onephase quasicrystalline alloy is possible only in a narrow concentration range and after appropriate heat treatment.

In the investigation, alloy $Al_{64,4}Cu_{22,5}Fe_{13,1}$ was synthesized and heat treated to increase the fraction of the *i*-phase. The presence of phases and other microstructural characteristics were determined using appropriate metallographic preparation methods, light microscopy (LM), scanning electron microscopy (SEM), microchemical analyses (EDS), X-ray diffraction (XRD), transmission electron microscopy (TEM) and microhardness measurements. The presence of quasicrystalline phase *i* was clearly confirmed using XRD and TEM.

Key words: Al-Cu-Fe, quasicrystal, metallography

## 1 UVOD

Leta 1984 so Shechtman in sodelavci [1] objavili članek o novi snovi, ki ima poseben elektronski uklonski vzorec – red dolgega dosega, vendar brez periodičnosti. To snov so kasneje poimenovali kvazikristalna snov. H. R. Trebin v knjigi Quasicrystals [2] trdi, da je kvazikristalno stanje tretje stanje trdnih snovi poleg kristalnega in amorfnega. Atomi so urejeno razporejeni, toda z rotacijskimi simetrijami, ki imajo pet-, osem-, deset- ali dvanajstštevne osi, ki jih nimajo snovi v kristalnem stanju.

Številne raziskave kvazikristalnih faz temeljijo na poglobljenem študiju tvorbe teh faz v zlitinah Al-Cu-Fe, saj so elementi, ki jih sestavljajo lahko dostopni, poceni in niso strupeni. Poleg tega spada zlitina Al-Cu-Fe med najbolj primerne za preučevanje nastanka kvazikristalnih faz, s tem pa tudi možnosti za uporabo kvazikristalnih zlitin. Velika verjetnost nastanka kompleksnih ternarnih spojin v zlitinah Al-Cu-Fe namreč izhaja že iz konstitucije robnih binarnih zlitinskih sistemov z večjim številom binarnih intermetalnih spojin.

Kristalografske značilnosti spojin v sistemu Al-Cu-Fe v območju *i*-faze so navedene v **tabeli 1**. Ugotovljeno je, da v ternarnem sistemu nastopa poleg kristalnih intermetalnih spojin tudi kvazikristalna *i*-faza, za katero je značilna ploskovno centrirana ikozaedrična kvazikristalna zgradba (FCI) [3]. Ta faza nastaja v skladu s ternarno peritektično reakcijo $L + \lambda + \beta \rightarrow i$ pri temperaturi 882 °C, kjer ima talina sestavo v točki $P_1$, kar je razvidno iz vertikalnega prereza ternarnega sistema zlitine Al-Cu-Fe pri $x(Cu) = 25$ % Cu (**slika 1**). Konstitucija vertikalnega prereza ternarnega sistema Al-Cu-Fe pri konstantni koncentraciji bakra ($x(Cu) = 25$ %) nazorno prikazuje razmere pri ternarni peritektični reakciji in potrjuje ugotovitve raziskovalcev [3], da ima kvazikristalna *i*-faza ozko koncentracijsko območje obstojnosti (blizu $Al_{62}Cu_{25,5}Fe_{12,5}$), ki se spreminja s temperaturo in je prikazano na **sliki 1** s črtkano črto.

Iz izotermnega prereza aluminijevega kota ternarnega sistema Al-Cu-Fe pri 700 °C (**slika 2**) je razviden obstoj več heterogenih ravnotežij in intermetalnih spojin, ki v njih sodelujejo.

Iz izotermnega prereza pri 700 °C (**slika 2**) je razvidno, da so lahko v ravnotežjem stanju z *i*-fazo štiri faze: $\omega$, $\lambda$, $\beta$ in talina (L), v metastabilnih stanjih pa se pojavijo še dodatne faze. Cilj našega dela je bil raziskati faze, ki se pojavljajo v zlitini $Al_{62}Cu_{25,5}Fe_{12,5}$ po litju in toplotni obdelavi.

**Tabela 1:** Najpomembnejše binarne in ternarne faze v sistemu Al-Cu-Fe v soseščini *i*-faze [8]
**Table 1:** The most important binary and ternary phases in system Al-Cu-Fe in the vicinity of *i*-phase [8]

| Stehiometrična formula spojine<br>Stechiometric formula of the compound | Kemična sestava<br>Chemical composition<br>*x*/% | Mrežni parametri<br>Lattice parameters | Kristalni sistem<br>Crystal system | Pearsonov simbol<br>Pearson's symbol |
|---|---|---|---|---|
| $\eta$ – AlCu | 49,8 – 52,4 Cu | $a$ = 0,4015 nm<br>$b$ = 1,202 nm<br>$c$ = 0,8652 | Ortorombični<br>Orthorombic | oP16 |
| $\xi$ – $Al_3Cu_4$<br>590–530 °C | 55,2 – 59,8 Cu | $a$ = 0,81 nm<br>$c$ = 1,000 nm | Heksagonalni<br>Hexagonal | hP42 |
| $\xi$ – $Al_3Cu_4$<br><570 °C | 55,2 – 56,3 Cu | $a$ = 0,707 nm<br>$b$ = 0,408 nm<br>$c$ = 1,002 nm<br>$\beta$ = 90,63° | Monoklinski<br>Monoclinic | m*21 |
| $\theta$ – $Al_2Cu$ | 31,9 – 33 Cu | $a$ = 0,6063 nm<br>$c$ = 0,487 nm | Tetragonalni<br>Tetragonal | tI12 |
| $\lambda$ – $Al_{13}Fe_4$ | od $Al_{78}Fe_{22}$ do $Al_{73}Cu_5Fe_{22}$ | $a$ = 1,5489 nm<br>$b$ = 0,8083 nm<br>$c$ = 1,247 nm<br>$\beta$ = 107,72° | Monoklinski<br>Monoclinic | mC102 |
| $\beta$ - Al(FeCu) | 22,0 – 54,5 Al | $a$ = 0,2909 nm | Kubična telesno centrirana<br>Cubic body centered | cP2 |
| $\omega$ – $Al_7Cu_2Fe$ | 70 Al | $a$ = 0,6336 nm<br>$c$ = 1,487 nm | Urejeni tetragonalni<br>Ordered tetragonal | tP40 |
| $i$ – $Al_{62}Cu_{25,5}Fe_{12,5}$ | | $a$ = 0,63346 | Ikozaedrični ploskovno centrirani<br>Icosahedral phase centred | –35m |

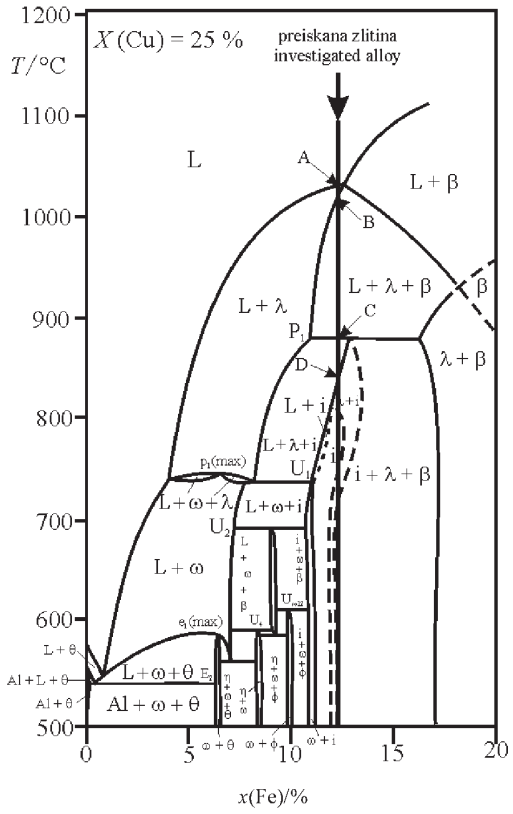


**Slika 1:** Vertikalni prerez ternarnega sistema Al-Cu-Fe pri 25 % Cu [6]
**Figure 1:** Vertical cross-section of the ternary system Al-Cu-Fe at 25 % Cu [6]

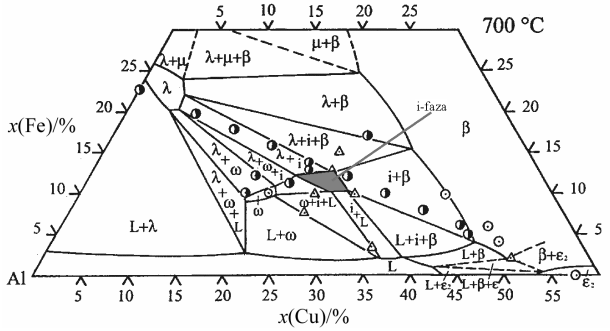


**Slika 2:** Izotermni prerez ternarnega faznega diagrama Al-Cu-Fe pri 700 °C v aluminijevem kotu [7]
**Figure 2:** Isothermal section of the ternary Al-Cu-Fe system in the Al-rich corner at 700 °C [7]

## 2 EKSPERIMENTALNO DELO

Zlitino Al-Cu-Fe smo izdelali v vakuumski peči LEYBOLD-HEREAUS IS pri tlaku $10^{-2}$ bar. Kot vložek smo uporabili aluminij ($w$ = 99,99 % in baker ($w$ = 99,99 %) ter predzlitino AlFe45. Lili smo v jekleno kokilo v zaščitni atmosferi argona. Izdelana zlitina je bila krhka, zato smo jo lahko zdrobili na majhne koščke, ki smo jih toplotno obdelali. Zlitino smo kemično analizirali z metodo ICP-AES (optična emisijska spektrometrija z indukcijsko sklopljeno plazmo), sestava zlitine je navedena v **tabeli 2**. Kemijska sestava je vedno navedena v množinskih deležih.

**Tabela 2:** Kemijska sestava preiskane zlitine Al-Cu-Fe
**Table 2:** Chemical composition of the investigated Al-Cu-Fe alloy

| | *w*/% / *x*(Al) % | *w*/% / *x*(Cu) % | *w*/% / *x*(Fe) % |
|---|---|---|---|
| ZLITINA 2 Al-Cu-Fe | 42,9 / 64,4 | 37 / 22,5 | 20 / 13,1 |

Vzorce zlitine $Al_{64,4}Cu_{22,5}Fe_{13,1}$ smo toplotno obdelali v cevni peči v zaščitni argonski atmosferi. Žarjenje je potekalo 24 h pri 750 °C (nato hitro ohlajanje) in 100 h pri 780 °C (vzorec je bil zataljen v kremenovo cevko v argonski atmosferi in v njej tudi toplotno obdelan, ohlajanje je bilo počasno).

Zlitino Al-Cu-Fe smo preiskali v izhodnem litem stanju in v toplotno obdelanem. Za karakterizacijo zlitine smo uporabili sodobne raziskovalne metode, kot so: svetlobna mikroskopija (SM), elektronska vrstična mikroskopija (SEM), elektronska presevna mikroskopija (TEM), mikrokemična spektroskopska analiza (EDS) in rentgenska fazna analiza (XRD). Pri nekaterih vzorcih smo tudi merili mikrotrdoto po Vickersu *HV* 0,05.

## 3 REZULTATI IN DISKUSIJA

Zlitina Al-Cu-Fe v začetnem litem stanju ima kemijsko sestavo v množinskih deležih 64,4 % Al, 22,5 % Cu in 13,1 % Fe. S svetlobno in vrstično elektronsko mikroskopijo smo ugotovili štiri faze: *i*, $\lambda$, $\beta$ in $\xi$ (**slika 3**

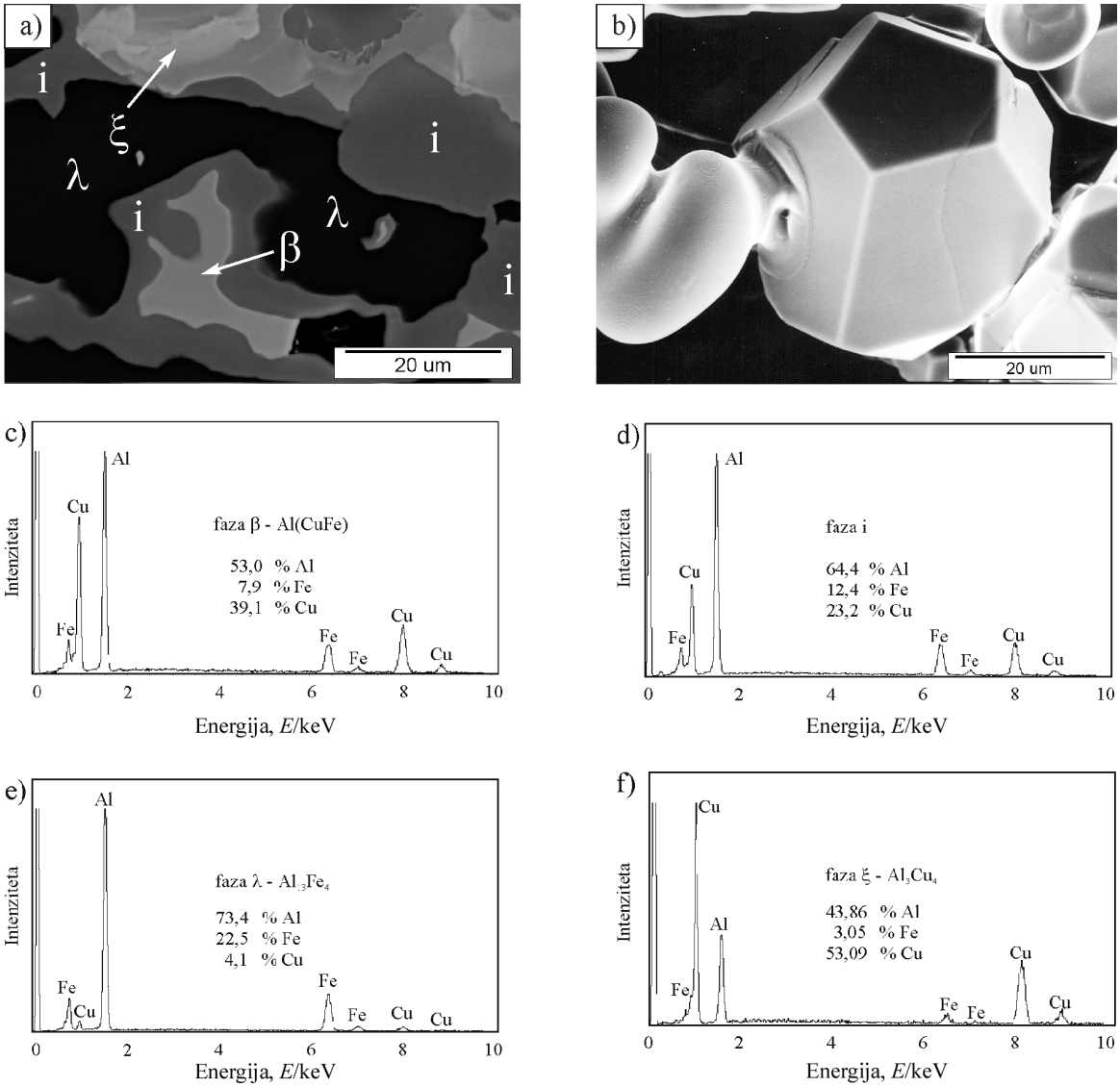


**Slika 3:** Mikrostruktura in EDS-spektri faz v zlitini $Al_{64,4}Cu_{22,5}Fe_{13,1}$ v začetnem litem stanju: a) SEM-posnetek mikrostrukture zlitine, b) SEM-posnetek monokvazikristala, ki je nastal z neovirano rastjo, c) EDS-spekter faze $\beta$, d) EDS-spekter faze *i*, e) EDS-spekter faze $\lambda$, f) EDS-spekter faze $\xi$

**Figure 3:** Microstructure and EDS-spectra of phases present in the alloy $Al_{64,4}Cu_{22,5}Fe_{13,1}$ in the as-cast condition: a) SEM-micrograph, b) SEM-micrograph of a quasicrystal with pentagonal octahedral morphology. c) EDS-spectrum of phase $\beta$, d) EDS-spectrum of i-phase, e) EDS-spectrum of phase $\lambda$, f) EDS-spectrum of phase $\xi$

**a**). Kemijsko sestavo posameznih faz smo ugotovili z analizo EDS (**slike 3 c do f**).

Na prelomni površini so vidni monokvazikristali (**slika 3 b**), ki so nastali s prosto rastjo *i*-faze s kemijsko sestavo 64,4 % Al, 12,4 % Fe in 23,2 % Cu (**slika 4 d**). Navzoče so še faze $\beta$ (Al(Cu,Fe) (**slika 4 c**), $\lambda$ ($Al_{13}Fe_4$) (**slika 4 e**) in $\xi$-($Al_3Cu_4$) (**slika 3 f**). Primarno se je izločala faza $\lambda$, vendar je bila njena količina majhna, ker je sestava zlitine zelo blizu evtektičnemu žlebu, zato kmalu poteče binarna evtektična reakcija L → $\lambda$ + $\beta$ (vertikalni prerez, **slika 1**). Preostala talina se porabi pri ternarni peritektični reakciji, ko nastane *i*-faza. Najsvetlejša faza $\xi$ je bogata z bakrom in se nahaja v meddendritnem prostoru.

### *3.1 Mikrostruktura zlitine $Al_{64,4}Cu_{22,5}Fe_{13,1}$ po DTA*

Vzorec zlitine smo kontrolirano segrevali do 1100 °C in ohlajali do sobne temperature s hitrostjo 10 K/min. S svetlobno in vrstično elektronsko mikroskopijo smo ugotovili, da so v mikrostrukturi vzorca po DTA štiri faze: *i*, $\beta$, $\lambda$ in $\beta$' (**sliki 4 a, b**).

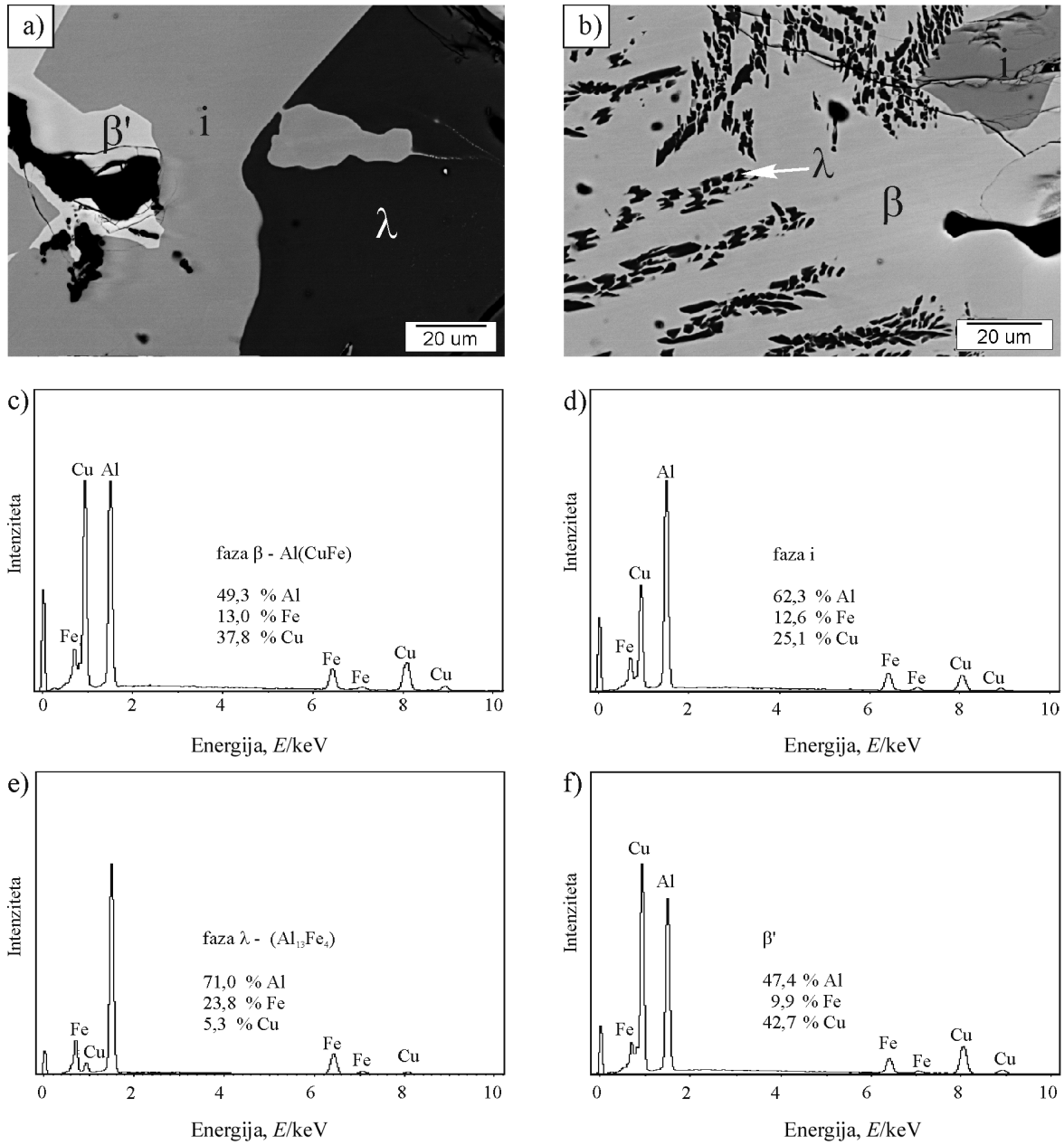


**Slika 4:** Mikrostruktura in EDS-spektri faz v zlitini $Al_{64,4}Cu_{22,5}Fe_{13,1}$ po DTA: a, b) SEM posnetka mikrostrukture, c) EDS-spekter faze $\beta$, d) EDS-spekter faze *i*, e) EDS-spekter faze $\lambda$, f) EDS-spekter faze $\beta$'

**Figure 4:** Microstructure and EDS-spectra of phases present in the alloy $Al_{64,4}Cu_{22,5}Fe_{13,1}$ after DTA: a, b) SEM-micrographs, c) EDS-spectrum of phase $\beta$, d) EDS-spectrum of i-phase, e) EDS-spectrum of phase $\lambda$, f) EDS-spectrum of phase $\beta$'

Pri strjevanju je primarno nastajala faza $\lambda$, kasneje je potekla še binarna evtektična reakcija, kjer sta se iz taline hkrati izločali fazi $\lambda$ in $\beta$. Glede na verikalni prerez ternarnega faznega diagrama (**slika 1**) poteče pri ravnotežnem strjevanju peritektična reakcija, kjer se tvori *i*-faza po reakciji: $\lambda + \beta + L \rightarrow i$. Pri nižjih temperaturah *i*-faza evtektoidno razpade v fazi $\lambda$ in $\beta$. Na **sliki 4 a** je $\lambda$ prikazana v dendritni obliki, ki je obdana z *i*-fazo. Na **sliki 4 b** je $\lambda$ prikazana v obliki peresastih delcev, ki je obdana s fazo $\beta$. Prisotna je še faza β' (najsvetlejša faza na **sliki 4 a**), ki ima glede na EDS-analizo (**slika 4 f**) od vseh analiziranih faz v tem vzorcu največji množinski delež bakra (42,7%).

Strjevanje zlitine v začetnem stanju in pri DTA je bilo neravnotežno, le da je bilo pri DTA počasnejše. Razlika se pokaže pri strjevanju preostale taline pri nižjih temperaturah. V začetnem litem stanju nastane faza $\xi$-($Al_3Cu_4$), ki ima okoli 3 % Fe in okoli 53 % Cu. Po drugi strani nastane v DTA-vzorcu, ki se je kontrolirano ohlajal s hitrostjo 10 K/min, nazadnje faza $\beta$' s sestavo okoli 10 % Fe in 43 % Cu. Nastanek faze $\beta$' je povezan s pomikom sestave zlitine k manjšim deležem železa in z oteženim nastankom $\omega$-faze [4].

### *3.2 Toplotno obdelano stanje 24 h pri 750 °C*

Vzorec zlitine $Al_{64,4}Cu_{22,5}Fe_{13,1}$ je bil 24 h žarjen pri 750 °C in hitro ohlajen. Na **sliki 5a** je prikazan vzorec v poliranem stanju. Zaradi toplotno aktiviranih procesov v

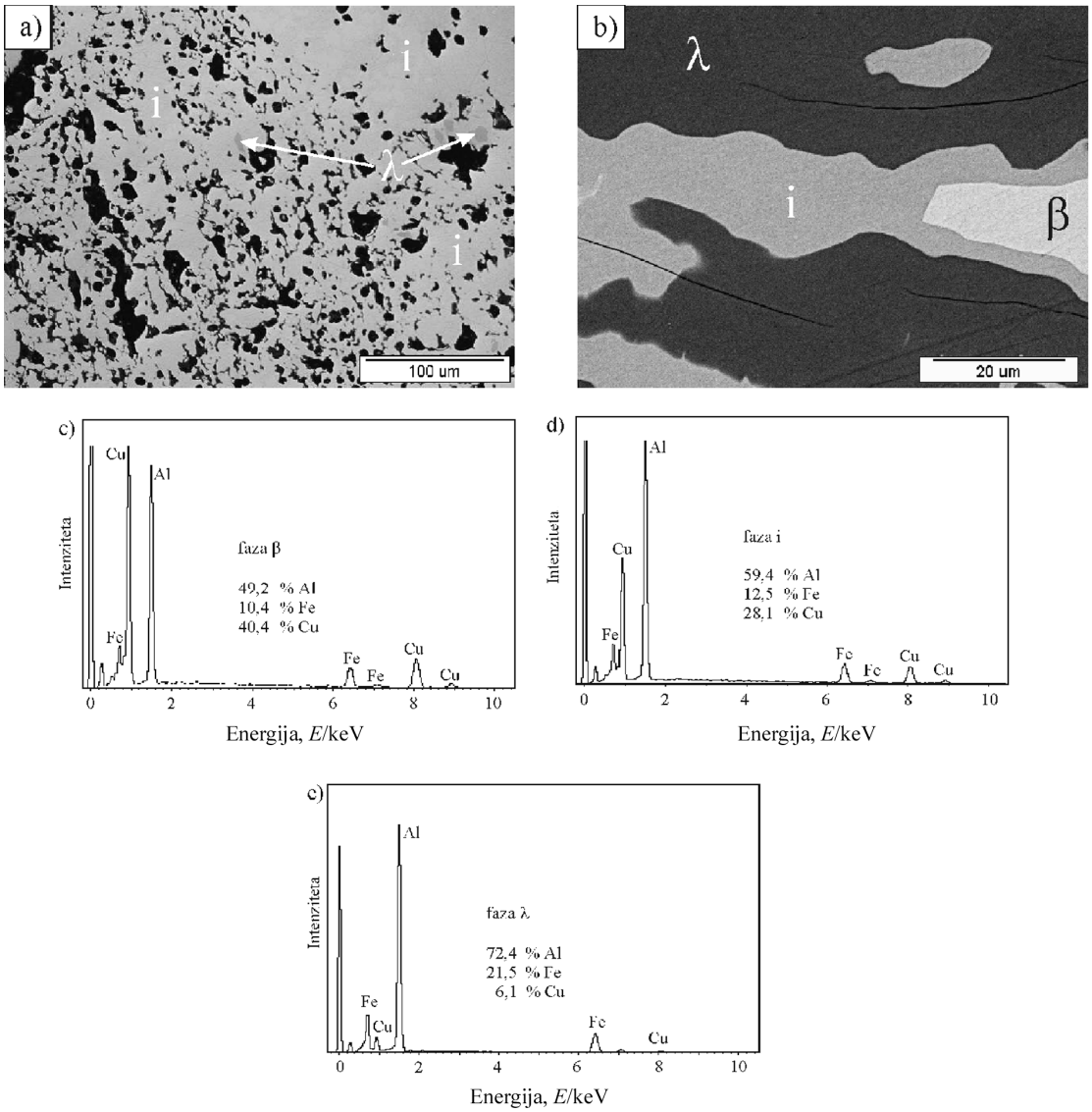


**Slika 5:** Mikrostruktura in EDS-spektri faz v zlitini $Al_{64,4}Cu_{22,5}Fe_{13,1}$ v toplotno obdelanem stanju (24 h pri 750 °C): a) pregledni SEM-posnetek, b) SEM-posnetek, c) EDS-spekter faze $\beta$, d) EDS-spekter faze *i* in e) EDS-spekter faze $\lambda$

**Figure 5:** Microstructure and EDS-spectra of phases present in the alloy $Al_{64,4}Cu_{22,5}Fe_{13,1}$ after heat treatment (24 h at 750 °C): a, b) SEM-micrographs, c) EDS-spectrum of phase $\beta$, d) EDS-spectrum of i-phase, e) EDS-spectrum of phase $\lambda$

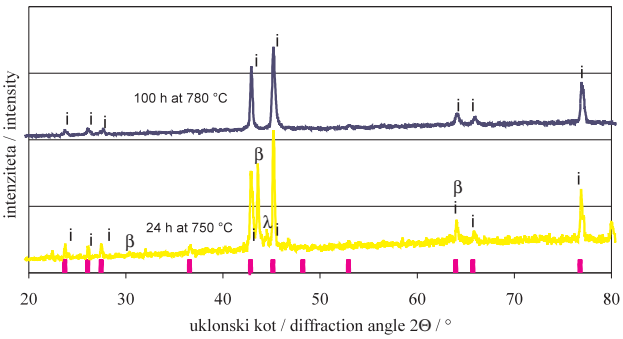


**Slika 6:** Rentgenska fazna analiza (XRD) toplotnoobdelane zlitine $Al_{64,4}Cu_{22,5}Fe_{13,1}$
**Figure 6:** X-ray diffraction of the heat-treated alloy $Al_{64,4}Cu_{22,5}Fe_{13,1}$

trdnem je celoten vzorec močno porozen, pojavi pa se tudi sprememba fazne sestave.

Mikrostruktura je sestavljena iz najsvetlejše faze $\beta$ (Al(Cu,Fe))(**slika 5 c**), *i*-faze (**slika 5 d**) in faze $\lambda$ ($Al_{13}Fe_4$) (**slika 5 e**). Glede na vertikalni prerez ternarnega faznega diagrama Al-Cu-Fe (**slika 1**) je bila temperatura 750 °C za zlitino $Al_{64,4}Cu_{22,5}Fe_{13,1}$ prenizka in čas žarjenja prekratek, da bi dosegli enofazno področje *i*-faze ali dvofazno področje ($\lambda$ + *i*). Prisotnost faz smo potrdili z EDS-analizo in rentgenska fazno analizo (XRD) (**slika 6**).

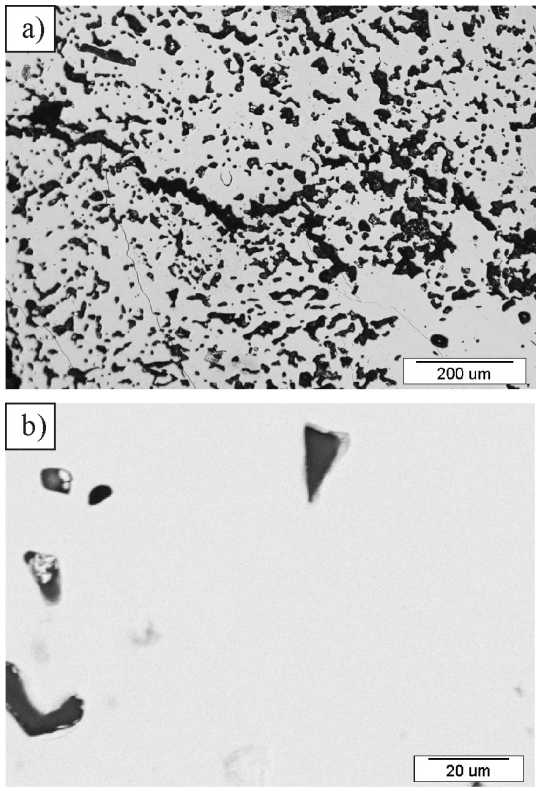


**Slika 7:** Mikrostruktura zlitine $Al_{64,4}Cu_{22,5}Fe_{13,1}$ v toplotno obdelanem stanju (100 h pri 780 °C): a) pregledni SM posnetek, b) SEM posnetek
**Figure 7:** a) Optical micrograph and b) SEM-micrograph of the alloy $Al_{64,4}Cu_{22,5}Fe_{13,1}$ in heat-treated condition (100 h at 780 °C)

### *3.3 Toplotno obdelano stanje 100 h pri 780 °C*

Vzorec zlitine smo žarili tudi 100 h na temperaturi 780 °C in počasi ohladili, kar je omogočilo približanje ravnotežnim razmeram ohlajanja. Majhna temperaturna razlika (30 °C) pri žarjenju in daljši čas žarjenja glede na toplotno obdelavo pri 750 °C povzročita velike razlike v mikrostrukturi. Po končanem žarjenju dobimo enofazno kvazikristalno strukturo (**sliki 7 a in b**).

Značilno kvazikristalno strukturo smo potrdili s presevno elektronsko mikroskopijo (TEM) (**slika 8**) in meritvami mikrotrdote, prisotnost kvazikristalne *i*-faze pa tudi z rentgensko fazno analizo (XRD) (**slika 6**).

Z uklonske **slike 8** je razvidna značilnost kvazikristalne strukture – ni periodičnega vzorca. V šestih smereh se razdalje med uklonskimi lisami povečujejo s $\tau$, ki je $(1 + \sqrt{5})/2$. Uklonske lise so med seboj oddaljene v razmerju $\tau \approx 1{,}6$. Tako razmerje velja med razdaljami BC/AB, DC/CB in DE/CD (**slika 8**). Z merjenjem mikrotrdote smo ugotovili, da je *HV* 0,05 942 ± 15, kar je skladno s podatki iz literature [5].

## 4 SKLEPI

Zlitina $Al_{64,4}Cu_{22,5}Fe_{13,1}$ vsebuje v začetnem litem stanju štiri faze: $\lambda$, *i*, $\beta$ in $\xi$. Enako število faz je bilo tudi po nadzorovanem ohlajanju z 10 K/min, le da se je namesto faze $\xi$ pojavila faza $\beta$'. Pri počasnem ohlajanju zlitine v začetnem litem stanju so bile ustvarjene razmere za neovirano rast kvazikristalov iz taline. Nastali monokvazikristali so imeli obliko pentagonalnega dodekaedra.

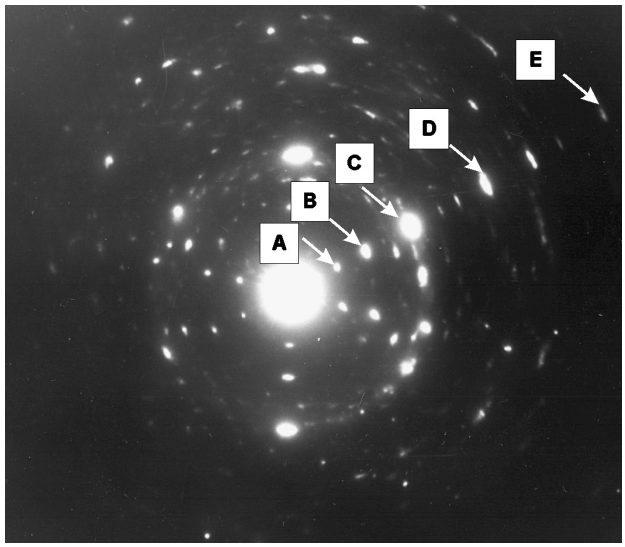


**Slika 8:** Uklonska slika (TEM) na zdrobljenih delcih zlitine $Al_{64,4}Cu_{22,5}Fe_{13,1}$ v toplotno obdelanem stanju (100 h pri 780 °C, počasno ohlajanje)
**Figure 8:** Selected area diffraction pattern of broken particles of the alloy $Al_{64,4}Cu_{22,5}Fe_{13,1}$ in the heat-treated condition (100 h at 780 °C, slow cooling)

Z ustrezno toplotno obdelavo se je delež faze *i* povečal. Po 24-urnem žarjenju zlitine $Al_{64,4}Cu_{22,5}Fe_{13,1}$ na 750 °C se je močno povečal delež faze *i*, vendar pa sta bili v zlitini še vedno fazi $\lambda$ in $\beta$. Toda po 100-urnem žarjenju na 780 °C in počasnem ohlajanju do sobne temperature, je ternarna peritektična reakcija $L + \lambda + \beta \rightarrow i$ potekla v celoti, tako je nastala enofazna kvazikristalna mikrostruktura. Kvazikristalna faza je imela trdoto *HV* okoli 1000.

Na osnovi raziskav lahko sklenemo, da lahko v zlitini $Al_{64,4}Cu_{22,5}Fe_{13,1}$ s primerno toplotno obdelavo dosežemo enofazno kvazikristalno mikrostrukturo. Prisotnost kvazikristalne faze *i* v raziskovanih zlitinah iz sistema Al-Cu-Fe smo zanesljivo potrdili s presevno elektronsko mikroskopijo in rentgensko fazno analizo.

## 5 LITERATURA


[1] D. S. Shechtman, I. Blech, D. Gratias, J. W. Cahn: Phy. Rev. Lett., 53 (**1984**), 1951–1953

[2] Quasicrystals, Structure and Physical Properties. Edited by Hans-Rainer Trebin: Wiley-VCH GmbH & Co. KgaA, Weinheim, 2003, 2–23

[3] A. P. Tsai, A. Inoue, T. A. Masumoto, Jpn. J. Appl. Phys., 26 (**1987**), L1505–L1507

[4] L. Zhang, R. Lück, Z. Metallkunde 94 (**2003**) 2, 774–781

[5] E. Giacometti, N. Baluc, J. Bonneville and J. Rabier, Scripta Materialia, 41 (**1999**) 9, 989–994

[6] L. Zhang, R. Lück Z. Metallkunde 94 (**2003**)2, 98–107

[7] L. Zhang, R. Lück, Z. Metallkunde 94 (**2003**)2, 108–115

[8] Ternary Alloys. Edited by G. Petzow and G. Effenberg: VCH Verlagsgesellscaft, Weinheim, 1988, 475–489, 361–362

UDK 669'295'296'24:669.788
Original scientific article/Izvirni znanstveni članek

ISSN 1580-2949
MTAEC9, 41(6)279(2007)

# HYDROGEN ABSORPTION BY Ti–Zr–Ni-BASED ALLOYS

## ABSORPCIJA VODIKA V ZLITINAH Ti–Zr–Ni

**Irena Škulj[1], Andraž Kocjan[2], Paul J. McGuiness[2], Borivoj Šuštaršič[1]**

[1]Institute for Metals and Technology, Lepi pot 11, 1000 Ljubljana, Slovenia
[2]Jožef Stefan Institute, Jamova 39, 1000 Ljubljana, Slovenia
irena.skulj@imt.si

*Prejem rokopisa – received: 2007-05-15; sprejem za objavo – accepted for publication: 2007-11-07*

Some transition metals and their alloys have the ability to reversibly absorb considerable amounts of hydrogen. The amount of absorbed hydrogen and the absorption kinetics depend on interactions between the hydrogen atoms and the alloy. Titanium and zirconium show a high affinity for hydrogen, and Ti–Zr–Ni alloys with either amorphous or quasicrystalline structures have proved to be excellent absorbers of hydrogen. In this study we have focused on processing Ti–Zr–Ni ribbons with four different compositions and investigating their hydrogenation behaviour. A melt-spinning process was used as the alloy-preparation technique, and samples from each composition were examined before and after the hydrogenation process. The ribbons were analysed by X-ray diffraction (XRD) and examined with a scanning electron microscope (SEM) equipped with an energy-dispersive X-ray spectrometer (EDS). Only the sample with the lowest nickel concentration was found to absorb any significant quantity of hydrogen under the applied experimental conditions.

Keywords: Quasicrystals, Ti–Zr–Ni alloys, Hydrogenation

Nekatere kovine prehoda in njihove zlitine imajo sposobnost reverzibilne absorpcije vodika. Količina absorbiranega vodika in kinetika absorpcije sta odvisni od interakcij med atomi vodika in atomi zlitine. Titan in cirkonij imata visoko afiniteto do vodika in zato zlitina Ti–Zr–Ni z amorfno ali kvazikristalno strukturo odlično absorbira vodik. V tem delu smo se osredinili na postopek izdelave trakov Ti–Zr–Ni s štirimi različnimi sestavami in preučili postopek hidrogenacije. Kot postopek izdelave trakov smo uporabili litje taline na vrteči se valj. Hitrostrjene trakove različnih sestav smo preučili pred hidrogenacijo in po njej. Trakove smo analizirali z rentgensko spektroskopijo (XRD) in vrstičnim elektronskim mikroskopom (SEM) z energijsko disperzijo rentgenskih žarkov (EDS). Le vzorec z najnižjo vsebnostjo niklja je pri danih pogojih absorbiral znatnejše količine vodika.

Ključne besede: kvazikristali, zlitine Ti–Zr–Ni, hidrogenacija

## 1 INTRODUCTION

Amorphous and quasicrystalline alloys have recently attracted a lot of attention for hydrogen-storage applications. Much of the research has concentrated on Ti- and Zr-based alloys and related materials. These alloys mostly contain an *i*-phase, which has an icosahedral quasicrystalline structure. These quasicrystals are able to absorb/desorb considerable amounts of hydrogen[1, 2, 3, 4]. Containing more tetrahedral sites in their structure than other crystals, and with Ti and Zr having high affinities for hydrogen, makes these alloys potentially excellent hydrogen-storage materials [5]. The *i*-type quasicrystal is formed either by rapid quenching or solid-state transformation at 500–600 °C, generally leading to a microstructure of quasicrystal and crystal phases with a grain size of several microns [1]. The melt-spinning process is a technique used for the rapid cooling of molten metals and alloys. It is used to develop materials that require extremely high cooling rates in order to form, for example, metallic glasses. The cooling rates achieved are of the order of $10^4$–$10^7$ K/s. Therefore, the process can be successfully used for the preparation of amorphous and quasicrystalline samples through the rapid solidification of a molten alloy on a cold spinning wheel made of copper. The cooling rate of the process has also been defined for this type of alloy with additions of silicon [6]. The hydrogenation of these alloys was successful at high temperatures and low pressures. However, only 10 % of the absorbed hydrogen can be evolved from the alloy during the heat treatment [7]. The aim of this study was to optimise the melt-spinning process for the production of ribbons with amorphous and quasicrystalline structures.

## 2 EXPERIMENTAL DETAILS

Samples with the compositions in Table 1 were prepared from $Ti_{78.6}Ni_{21.4}$, $Zr_{65.9}Ni_{34.1}$ and $Ti_{60}Zr_{40}$ binary-alloy ingots. The starting alloys were crushed into smaller lumps (≈3 cm), and suitable amounts of each composition were put in to a melting crucible in an induction furnace. The crucible we used was made of graphite, coated with a zirconia-water suspension that was dried before use. The coating was used to prevent the formation of carbides. Induction melting in a vacuum was used to prepare the pre-alloy with the desired composition. The homogenous pre-alloys were then re-melted and spun to obtain the ribbons. The melt-spinning process was carried out with a 25.2 m/s wheel speed, and the size of the crucible's nozzle was

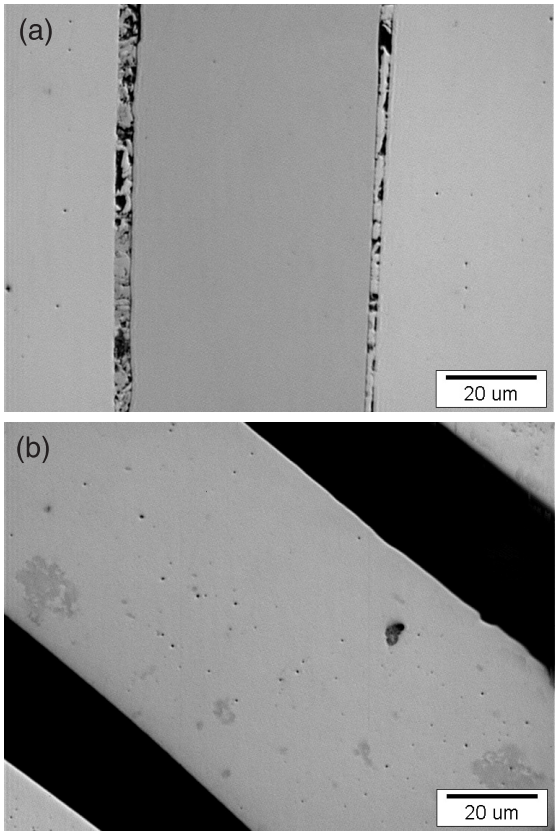


**Figure 1:** Cross-sectional view of the ribbon with the most (a) and the least (b) amount of Ni present in the microstructure
**Slika 1:** Prečni prerez traku z največjo (a) in najmanjšo (b) vsebnostjo Ni v mikrostrukturi

2.2 mm ($\phi$). To obtain melt-spun ribbons with the desired structure it was necessary to choose a suitable wheel speed and the correct size of nozzle. The process was carried out in a slight under-pressure of argon. Some of the prepared ribbons were examined and others were hydrogenated. The hydrogenation process was carried out in a furnace in a hydrogen atmosphere. First, the ribbons were put in to the furnace and the furnace was sealed. The furnace was then evacuated and refilled with an 8-bar over-pressure of hydrogen. The furnace was heated up to 350 °C, and the temperature was maintained at this temperature. When the absorption was complete the furnace was allowed to cool down and the remaining hydrogen was released from the system.

All the ribbons, as-melt-spun and hydrogenated, were investigated with an X-ray diffractometer (XRD) and examined with a scanning electron microscope (SEM) equipped with an energy-dispersive spectrometer (EDS). The samples for the SEM examinations and the EDS analyses were ground and polished prior to the examination.

## 3 RESULTS AND DISCUSSION

The cross-sections of the samples obtained using an optical microscope can be seen in **Figure 1**. A comparison was made between sample A1, with the highest amount-of-substance fraction of Ni present in the composition (26.3 %), and sample A2, with the smallest amount-of-substance fraction of Ni present in the

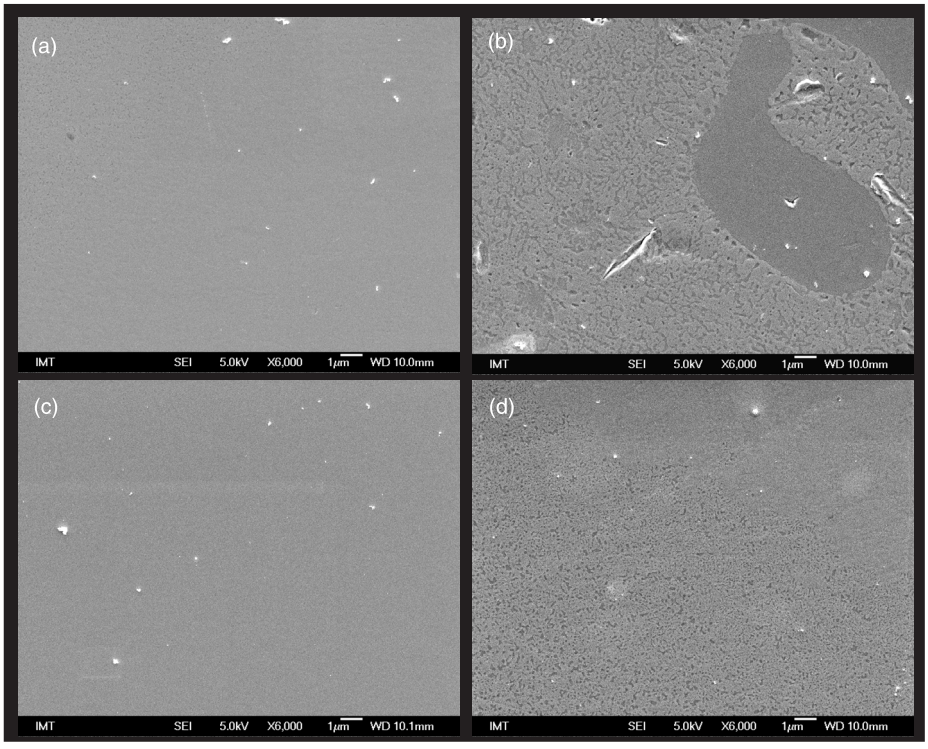


**Figure 2:** Cross-sectional views of the as-melt-spun ribbons with compositions A1 (a), A2 (b), A3 (c) and A4 (d)
**Slika 2:** Prečni prerez hitrostrjenih trakov s sestavami A1 (a), A2 (b), A3 (c) in A4 (d)

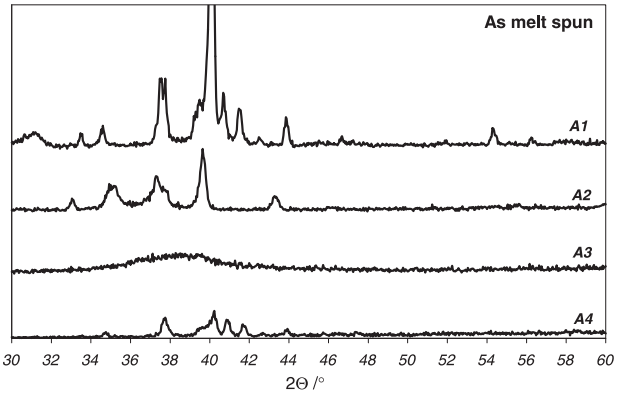


**Figure 3:** XRD scans of as-melt-spun Ti–Zr–Ni ribbons
**Slika 3:** XRD spektri hitrostrjenih trakov Ti–Zr–Ni

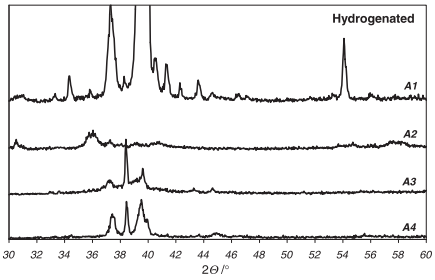


**Figure 4:** XRD scans of as-melt-spun Ti–Zr–Ni ribbons after hydrogenation
**Slika 4:** XRD spektri hitrostrjenih trakov Ti–Zr–Ni po hidrogenaciji

composition (17 %). It seems that the sample with less Ni in the overall composition forms a two-phase microstructure and the sample with more Ni forms a single-phased microstructure. The assumption was confirmed by the SEM investigation. From the images shown in **Figure 2** it is clear that sample A2 (**Figure 2b**) is the only one consisting of two phases. All the other samples, with higher Ni concentrations, have single-phase microstructures. All the samples and phases were analysed with EDS, and the results are collected in **Table 2**. All the phase compositions are in accordance with the starting compositions listed in **Table 1**. The ribbons with the A2 composition are the only samples containing Ti–Zr particles in a matrix structure, which again agrees with the original composition (**Table 1**). The particles can be seen in **Figures 1 b and 2 b**.

XRD scans belonging to the as-melt-spun samples are collected in **Figure 3**. It is clear that sample A3 was the only sample that had an amorphous structure. All other samples, A1, A2 and A4, show patterns that indicate the presence of crystalline phases. From this we can conclude that the solidification resulting from melt spinning at 25.2 m/s with a 2.2 mm nozzle was insufficiently rapid to form an amorphous structure except in the sample with the lowest amount of Ni. The samples with compositions A1, A2 and A4 cooled down

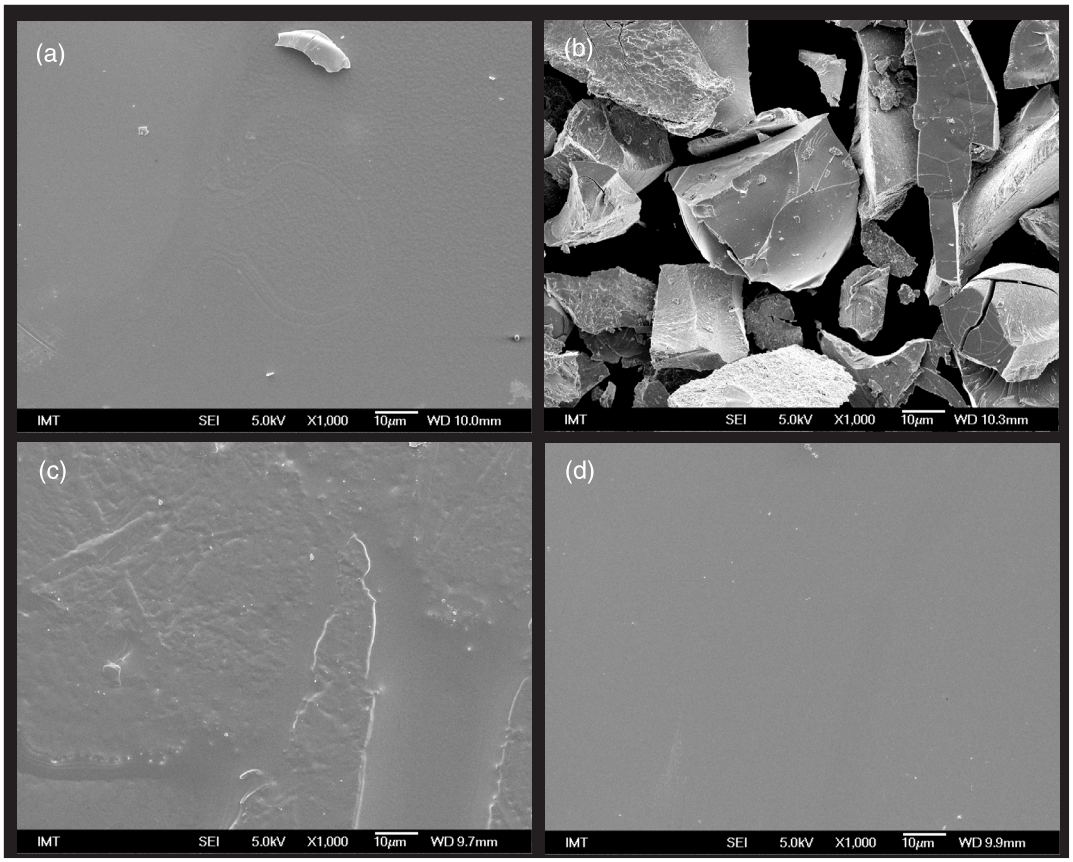


**Figure 5:** Ribbons with compositions A1 (a), A2 (b), A3 (c) and A4 (d) after hydrogenation
**Slika 5:** Trakovi s setavo A1 (a), A2 (b), A3 (c) in A4 (d) po hidrogenaciji

**Table 1:** Compositions
**Tabela 1:** Sestava

| | |
|---|---|
| A1 | $Ti_{48}Zr_{26}Ni_{26}$ |
| A2 | $Ti_{50}Zr_{33}Ni_{17}$ |
| A3 | $Ti_{44}Zr_{33}Ni_{23}$ |
| A4 | $Ti_{50}Zr_{29}Ni_{21}$ |

**Table 2:** Compositions of phases forming the microstructure of melt-spun ribbons
**Tabela 2:** Sestave faz, ki tvorijo mikrostrukturo hitrostrjenih trakov

| | Phase | *x*(Ti)/% | *x*(Zr)/% | *x*(Ni)/% |
|---|---|---|---|---|
| A1 | Matrix | 48.3 ± 0.5 | 26.1 ± 0.7 | 25.6 ± 0.5 |
| A2 | Matrix | 50.1 ± 0.5 | 33.7 ± 0.7 | 16.2 ± 0.5 |
| | Particle | 56.2 ± 0.5 | 43.8 ± 0.7 | / |
| A3 | Matrix | 43.9 ± 0.5 | 33.3 ± 0.7 | 22.8 ± 0.5 |
| A4 | Matrix | 51.4 ± 0.5 | 27.8 ± 0.7 | 20.9 ± 0.5 |

**Table 3:** Compositions of the phases forming the microstructure of the hydrogenated ribbons
**Tabela 3:** Sestave faz, ki tvorijo mikrostrukturo hidrogeniranih trakov

| | *x*(Ti)/% | *x*(Zr)/% | *x*(Ni)/% |
|---|---|---|---|
| A1 | 48.7 ± 0.5 | 26.1 ± 0.7 | 25.2 ± 0.5 |
| A2 | 49.1 ± 0.5 | 33.3 ± 0.7 | 17.6 ± 0.5 |
| | 56.3 ± 0.5 | 43.7 ± 0.7 | / |
| A3 | 43.2 ± 0.5 | 33.8 ± 0.7 | 23.0 ± 0.5 |
| A4 | 50.3 ± 0.5 | 28.0 ± 0.7 | 21.7 ± 0.5 |

too slowly and so had time to form a crystalline structure.

Based on these results we can state that the conditions used during the melt-spinning process were not suitable for producing ribbons with an amorphous structure. The oversized nozzle as well as a too-slow wheel speed during the melt-spinning process resulted in a relatively slow cooling rate and slow solidification, giving the material time to crystallise. At this stage it is also worth mentioning that the melting temperature of the alloy is increasing with decreasing Ni content. From the Ti–Zr–Ni phase diagram [9] it is clear that when the decreasing Ni content exceeds the amount-of-substance fraction ≈22 % the solidus-liquidus area starts widening. A consequence of this is the presence of solid particles in the melt that could cause difficulties during melt-spinning.

The images in **Figure 5** and the XRD scans in **Figure 4** were obtained from ribbons after hydrogenation. Comparing the scans for A1, A3 and A4 before and after the hydrogenation it is clear that the scans are the same, proving that no hydrides were formed during the hydrogenation process. The compositions in **Tables 2 and 3** also confirm that the samples did not absorb any hydrogen. Sample A2 was the only affected sample. When exposed to hydrogen the hydrogen penetrated via grain boundaries through the ribbons and forced the grains to decrepitate [9]. Consequence of the process was the formation of a powder with an unaffected composition.

It can also be concluded that the hydrogenation conditions were not sufficient for the hydrogenation to proceed. It is most likely that the hydrogen pressure applied to the sample was insufficient. Unfortunately, the existing equipment used for the hydrogenation is not capable of supporting higher pressures.

## 4 CONCLUSIONS

From a range of samples with different amounts of Ni in their compositions only the sample with smallest amount-of-substance fraction Ni (17 %) content forms a two-phase structure. Some Ti–Zr particles are present in the microstructure. All the other compositions formed a single-phase microstructure.

The cooling rate of the melt-spun samples was not fast enough to provide the conditions for fast solidification and, consequently, ribbons with an amorphous structure, except for the sample with least amount of Ti.

The conditions under which the hydrogenation process was carried out were found to be insufficient to initiate the formation of hydrides for three of the four samples.

### Acknowledgements

Many thanks go to the Jožef Stefan Institute for their support and contribution to the research of which this work forms a part. Thanks also to Slovenian research agency ARRS for their financial support.

## 5 REFERENCES

[1] Davis J. P., Majzoub E. H., Simmons J. M., Kelton K. F.; Mater. Sci. Eng.; 104 (**2000**), A294
[2] Guo X. Q., Louzguine D. V., Yamaura S., Ma L. Q., Sun W., Hasegawa M., Inoue A.; Mater. Sci. Eng.; A338 (**2002**), 97
[3] Viano A. M., Majzoub E. H., Stroud R. M., Kramer M. J., Misture S. T., Gibbons P. C., Kelton K. F.; Phil. Mag. A; 78 (**1998**) 1, 131
[4] Gibbons P. C., Hennig R. G., Huett V. T., Kelton K. F.; J. non-crystalline Solids; 334&335 (**2004**), 461
[5] Batalla E., Strom-Olsen J. O., Altounian Z., Boothroyd D., Harris R.; J. Mater. Res.; 1 (**1986**), 765
[6] Rud A. D., Schmidt U., Slukhovskii O. I., Zeliska G. M.; J. Alloys Comp.; 373 (**2004**), 48
[7] Viano A. M., Stroud R. M., Gibbons P. C., McDowell A. F., Conradi M. S., Kelton K. F.; Phys. Rew. B; 51(**1995**) 17, 12026
[8] Kelton K. F., Gangopadhyay A. K., Lee G. W., Hyers R. W., Rathz T. J., Robinson M. B., Rogers J.; Studies of nucleation and growth, specific heat and viscosity of undercooled melts of quasicrystal and ploytetrahedral-phase forming alloys, Proc. of NASA Microgravity Materials Science Conference, Huntsville, Alabama, USA, 2000, 327–337
[8] McGuiness P. J., Harris, I. R., Rozendaal, E., Ormerod, J., Ward, M. Journal of Materials Science 21(**1986**) 11, 4107

UDK 669.715:620.18
Original scientific article/Izvirni znanstveni članek

ISSN 1580-2949
MTAEC9, 41(6)283(2007)

# MICROSTRUCTURAL EVALUATION OF RAPIDLY SOLIDIFIED Al–7Cr MELT SPUN RIBBONS

## OVREDNOTENJE MIKROSTRUKTURE HITROSTRJENIH TRAKOV Al-7Cr

**Peter Jurči[1], Mária Dománková[2], Mária Hudáková[2], Borivoj Šuštaršič[3]**

[1]ECOSOND, Ltd., K Vodárně 531, 257 22 Čerčany, Czech Republic
[2]STU Trnava, J. Bottu 52, 917 24 Trnava, Slovak Republic
[3]IMT, Lepi pot 11, 1000 Ljubljana, Slovenia
p.jurci@seznam.cz

*Prejem rokopisa – received: 2007-09-20; sprejem za objavo – accepted for publication: 2007-10-18*

The use of conventional bulk materials is limited by segregation phenomena, which are generated during the solidification and cannot be eliminated in the solid state. The introduction of rapid-solidification technology (RST) into material processing overcame some of the problems of unacceptable material quality and broadened the range of materials that it is possible to fabricate.
The use of conventional ingot metallurgy for the fabrication of aluminium alloys containing a large amount of elements with a low diffusion coefficient is impossible because coarse, hard and brittle intermetallics are formed and the alloys have poor mechanical properties. The use of RST makes it possible to produce these alloys with an improved microstructure; however, before industrial production the structure and properties of the rapidly solidified semi-products as well as the consolidated bulk product must be evaluated systematically.
In this paper, melt-spun ribbons, made under various conditions from a binary Al–7%Cr, alloy are investigated. The structure consisted of a supersaturated Al solid solution with a high dislocation density, precipitates of chromium-rich phases and rosette-like spherolites formed from the Al solid solution and the $Al_7Cr$ intermetallic phase. The type of phases is related to the processing conditions in only a very limited way.

Keywords: rapid solidification, melt spinning, ribbons, microstructure

Praktična uporaba konvencionalnih kovinskih materialov je omejena zaradi izcejanja zlitinskih elementov. To nastaja zaradi različnih vzrokov in pojavov med strjevanjem in ga je praktično nemogoče odpraviti s kasnejšo toplotno obdelavo v trdnem stanju. Hitro strjevanje in njegova vpeljava kot tehnologije za procesiranje različnih kovinskih materialov premaguje to oviro in razširja izbiro materialov.
Uporaba konvencionalne metalurgije ingotov za izdelavo Al zlitin z velikim deležem legirnih elementov z majhnim difuzijskim koeficientom je praktično nemogoča, ker v mikrostrukturi nastajajo grobi delci trdih in krhkih intermetalnih spojin in imajo zlitine nizke mehanske lastnosti. Uporaba tehnologije hitrega strjevanja omogoča izdelavo teh zlitin z izboljšano mikrostrukturo, pred vpeljavo te tehnologije v redno proizvodnjo pa je treba sistematično analizirati strukturo in lastnosti hitrostrjenih polproizvodov ter iz njih izdelanega zgoščenega izdelka.
V tem članku obravnavamo raziskave hitro strjenih trakov zlitine Al z masnim deležem Cr 7 %, izdelanih pri različnih pogojih. Preiskave so pokazale, da mikrostrukturo sestavljajo: s Cr prenasičena trdna raztopina Al z veliko gostoto dislokacij ter izločki na Cr bogatih faz, kakor tudi peritektik v obliki rozet nastal iz trne raztopine Al in intermetalne faze $Al_7Cr$. Ugotovili smo, da je oblika in velikost posameznih faz relativno malo odvisna od izbranih pogojev izdelave hitro strjenih trakov.

Ključne besede: hitro strjevanje, nalivanje na hitrovrteči se valj, trakovi, mikrostruktura

## 1 FUNDAMENTAL

The industrial use of metallic materials is limited by their microstructure and mechanical properties, characteristics that are greatly influenced by the initial casting operation. During slow cooling in large industrial ingots a considerable amount of segregation takes place due to the different solubilities in the solid and the liquid, and this cannot be improved via a solid-state thermal treatment. Only a rapid solidification can successfully overcome the problems connected with segregation and produce fine-grained, segregation-free materials with an unusual chemical composition and unique mechanical properties.

Rapidly solidified (RS) materials differ a great deal from materials with the same chemical composition prepared by conventional casting procedures in terms of the refinement of the main structural constituents [1–3]. As a result of non-equilibrium freezing, they may also contain supersaturated phases, metastable intermediate phases or, in limited cases, amorphous constituents [4,5]. The results affect the microstructures and the properties of materials, in many cases favourably, and this positive effect of RS on materials' characteristics has been clearly determined [6–8].

One typical example where the rapid solidification is required to obtain material with acceptable properties is the group of aluminium alloys with elements that have a negligible solid solubility and a low diffusion coefficient. In conventionally produced Al alloys, elements like Fe, Ni, V, Cr, etc. are considered as impurities, since they form coarse and brittle aluminides. On the other hand, Al alloys containing elements with a low diffusion coefficient made by the RS technique exhibit an

excellent combination of toughness and elongation and are stable up to relatively high temperatures [7,8].

The Al–Cr system is a very typical example. The solid solubility of chromium in aluminium is very low. In slowly solidified material, for example, chromium forms large needle-like as well as branch-like particles of $Al_xCr_y$ intermetallics, which have a deleterious effect on the mechanical properties. On the other hand, powder-metallurgy materials based on this binary system, with the addition of some other elements, can easily achieve an ultimate tensile strength up to 600 MPa during an elongation of several percents [9,10].

## 2 EXPERIMENTAL

The $Al_7Cr$ alloy was prepared from technically pure aluminium and chromium. The mixture made from raw materials was molten in a vacuum furnace and overheated up to 1150 °C in order to eliminate the occurrence of large and hardly soluble intermetallics in the melt.

Melt-spun ribbons were prepared in an experimental device, i.e., the Melt-Spinner M-10, in IMT, Ljubljana. The metals were melted under an argon overpressure. The rotation speed of the copper wheel ranged between 900 r/s and 1350 r/s (16.8 $ms^{-1}$ and 25.2 $ms^{-1}$). Other important parameters of the melt-spinning process are given in **Table 1**.

The microstructure of the alloy was investigated using light microscopy (slowly solidified material) and transmission electron microscopy (melt-spun ribbons). The microstructure of the slowly solidified material was revealed by using the Dix-Keller reagent. Thin foils were prepared directly from the rapidly solidified ribbons using a TENUPOL 2® device. A mixture of 30 % nitric acid and 70 % methanol was used as an etching agent. The thinning was carried out at a temperature of –30 °C and a bias of 19 V.

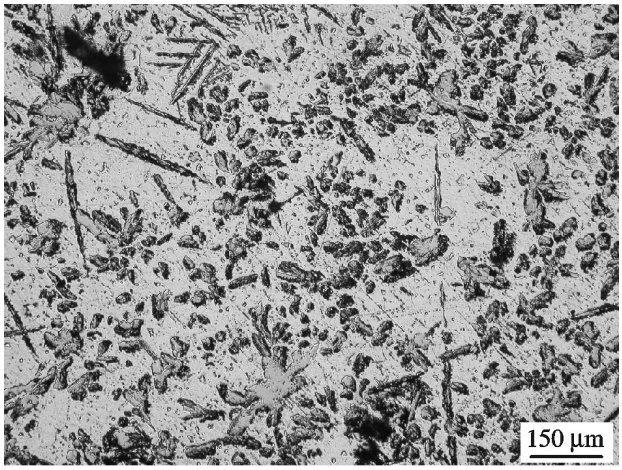


**Figure 1:** Optical micrograph of the slowly solidified alloy with star-shaped formations of intermetallics

**Slika 1:** Optični posnetek počasi strjene zlitine z zvezdastimi intermetalnimi spojinami

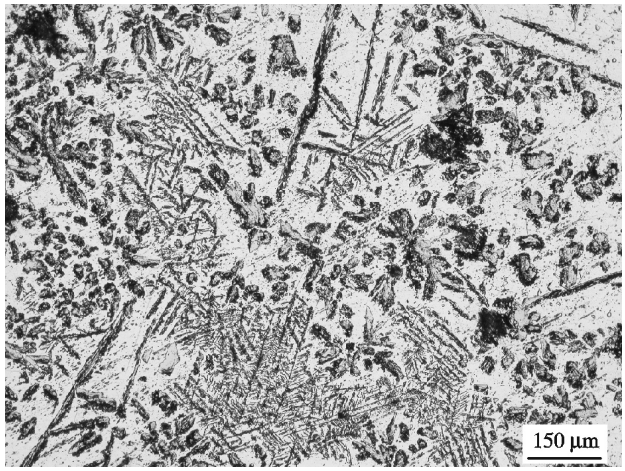


**Figure 2:** Optical micrograph of the slowly solidified alloy with semi-globular particles of intermetallics

**Slika 2:** Optični posnetek počasi strjene zlitine s polkroglastimi intermetalnimi spojinami

## 3 RESULTS AND DISCUSSION

The microstructure of the slowly solidified material in an as-cast ingot is shown in **Figures 1 and 2**. **Figure 1** shows an optical micrograph of the slowly solidified alloy with star-shaped formations of intermetallics, and **Figure 2** shows the slowly solidified alloy with semi-globular particles of intermetallics.

The alloy has a dendritic solidification morphology composed of a relatively large amount of intermetallic phases, which differ from each other mainly in shape and size. Some of them have a globular, convex shape, which indicates primary crystallization from the melt. In some cases, star-shaped formations are found in the micro-

**Table 1:** Important parameters of the melt spinning process

**Tabela 1:** Pomebni parametri procesa hitrega strjevanja

| Sample designation | Superheating of the melt | Induction heating power | Atmosphere (vacuum + Ar 5.9) | Wheel speed | Nozzle diameter |
|---|---|---|---|---|---|
| | °C | | | m/s | mm |
| Al-1 | 1030 | 3 kW to 500 °C<br>7 kW to 1030 °C<br>(heating rate approx. 70 °C/min.) | 60 kPa overpressure of argon | 16.8 | 2.2 |
| Al-2 | | | | 19.6 | 0.8 |
| Al-3 | | | | 25.2 | 0.8 |

structure, **Figure 1**. Their occurrence can be related to the primary crystallization and a peritectic reaction between the intermetallic and the Al solid solution.

From the binary Al–Cr equilibrium diagram only the $Al_7Cr$ intermetallic would be expected for our chosen composition, although with an increased Cr content other compounds would also be possible ($Al_{11}Cr_2$, $Al_4Cr$, $Al_3Cr$, $Al_9Cr_4$, etc.) [11,18]. All these intermetallics are non-stoichiometric compounds (Bertholides) with a relatively narrow range of possible compositions.

X-ray diffraction fixed the Al solid solution with sharp diffraction lines. This indicates that during a slow solidification no supersaturation of the solid solution occurred, **Figures 3 and 4**. The second phase was identified as the $Al_{13}Cr_2$ compound, **Figure 3**. In the binary diagram reported in [11] there is only the isoconcentration $Al_7Cr$ phase. In reference [12], it is suggested that the phase is stable in a given concentration range. Taking into account the fact that the investigated alloy has a lower chromium content than the compound, the stoichiometry $Al_{13}Cr_2$ may correspond to the lower limit of the range for the $Al_7Cr$ compound. In addition, an intermetallic phase with the same stoichiometry was also found by Selke [13] in the bulk alloy Al–15 % Cr. In this alloy the chromium content is also below the concentration range of the phase $Al_7Cr$ [12]; it is, however, twice as high as in the alloy investigated in this work. Pearson´s Handbook also mentions the $Al_{45}Cr_7$ phase. The stoichiometric ratio of 45:7 is between that of 13:2 and 7:1 and, with respect to the actual chemical composition of the alloy, the probability of its occurrence is lower than that for the $Al_{13}Cr_2$. Therefore, identifying this intermetallic as $Al_{13}Cr_2$ is considered to be correct.

**Figure 5** shows one of the features of the specimen Al-1. This type is represented by a primary crystallized rosette-like particle having a size of about 250 nm. Electron diffraction patterns fixed this phase as $Al_{11}Cr_2$ aluminide, in good agreement with the Al–Cr binary equilibrium diagram [12], where the $Al_{11}Cr_2$ phase is in

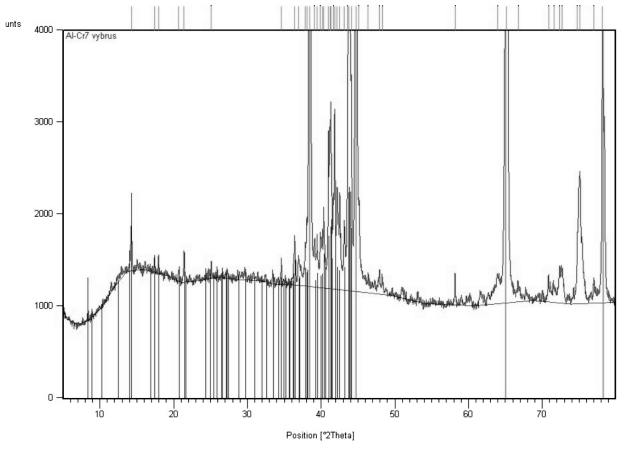


**Figure 3:** X-ray patterns from the slowly solidified material: red lines, Al; blue lines, $Al_{13}Cr_2$

**Slika 3:** Rentgenska difrakcijska slika počasi strjene zlitine: Al – rdeče črte, $Al_{13}Cr_2$ – modre črte

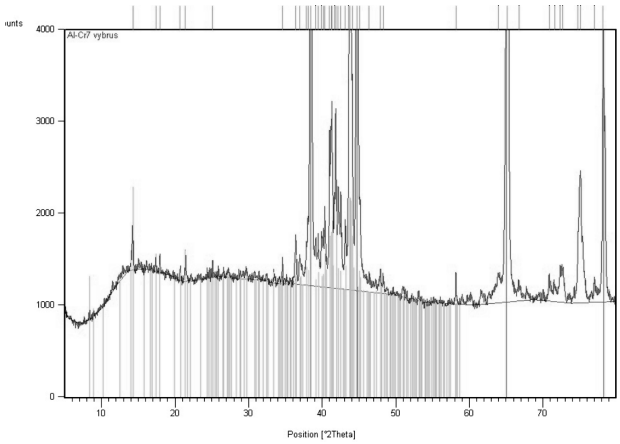


**Figure 4:** X-ray patterns from the slowly solidified material: red lines, Al; green lines, $Al_{45}Cr_7$

**Slika 4:** Rentgenska difrakcijska slika počasi strjene zlitine: Al – rdeče črte, $Al_{45}Cr_7$ – zelene črte

equilibrium with the residual melt above 785 °C. In the slowly solidified alloy, the $Al_{11}Cr_2$ phase decomposes normally to the Al solid solution with a negligible Cr content and the phase $Al_7Cr$. However, if the solidification rate is rapid enough the phase can be conserved in the alloy down to room temperature.

**Figure 6** shows the aluminium solid-solution matrix with a relatively high dislocation density in the same specimen. The electron diffraction patterns revealed a

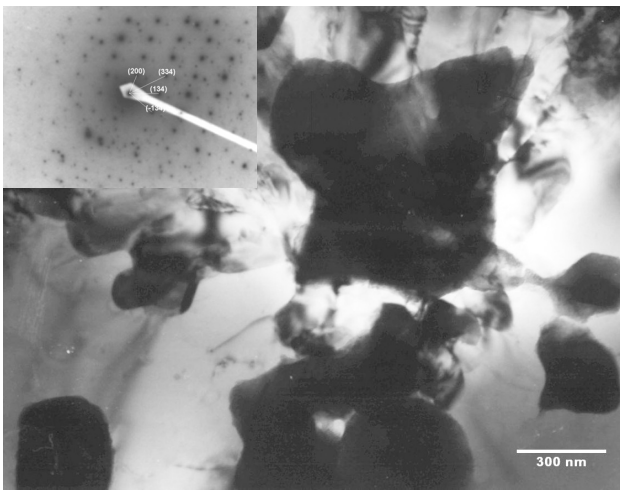


| Measured values | | Tabular values for the $Al_{11}Cr_2$ | |
|---|---|---|---|
| č.s. | $d_{vyp}/(10^{-10}\,m)$ | (h k l) | $d_{hkl}/(10^{-10}\,m)$ |
| 1 | 6.25 | 2 0 0 | 6.17 |
| 2 | 4.35 | 1 3 4 | 4.30 |
| 3 | 3.10 | 3 3 4 | 3.06 |
| 4 | 4.35 | –1 3 4 | 4.30 |
| $\varphi_{1/2} = 69°$ | | $\varphi_{(200)a(134)} = 69.6°$ | |

**Figure 5:** A typical primary particle in the specimen Al-1

**Slika 5:** Značilen primarni delec v vzorcu Al-1

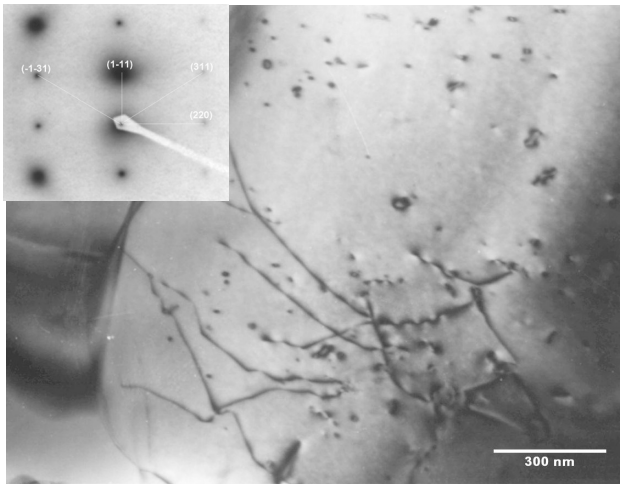


| Measured values | | Tabular values for the (Al) | |
|---|---|---|---|
| č.s. | $d_{vyp}/(10^{-10}\text{m})$ | (h k l) | $d_{hkl}/(10^{-10}\text{m})$ |
| 1 | 2.43 | 1 -1 1 | 2.34 |
| 2 | 1.48 | 2 2 0 | 1.43 |
| 3 | 1.26 | 3 1 1 | 1.22 |
| 4 | 1.26 | -1 -3 1 | 1.22 |
| $\varphi_{1/2} = 90°$ | | $\varphi_{(1\text{-}11)a(220)} = 90°$ | |

**Figure 6:** The Al solid-solution matrix in the specimen Al-1
**Slika 6:** Matica trdne raztopine v vzorcu Al-1

lattice distortion in comparison to the equilibrium situation. Both of these phenomena can be ascribed to the rapid solidification, which produced the supersaturation of the solid solution and the enhanced dislocation density in the matrix.

The TEM micrograph in **Figure 7** shows the rosette-like spherolite from the sample Al-2. The circular-shaped constituent with a diameter of 2 μm consists of the Al solid solution and an intermetallic phase, identified as the $Al_4Cr$ aluminide.

**Figure 8** shows the second constituent, which consists of many semi-globular particles with a size of several tens of nanometers, surrounded by dislocation clusters. These particles correspond very well to the high-temperature δ-phase with a stoichiometry of $Al_9Cr_4$. The matrix is formed in a similar way as in the previous specimen from the supersaturated Al solid solution.

The last constituent of the microstructure of the investigated melt-spun ribbons is presented in **Figure 9**. It consists of vermicular $Al_7Cr$ precipitates embedded in the Al solid-solution matrix. As confirmed by the electron diffraction, the lattice spacings do not correspond exactly to the equilibrium $Al_7Cr$ phase; they are smaller, which suggests that the phase is also partly non-equilibrium.

To understand the nature of the phases occurring in thin melt-spun ribbons, the Al–Cr equilibrium diagrams [11,12] must first be taken into consideration. Shunk [14] reported that $\theta$-$Al_{13}Cr_2$ and $\eta$-$Al_{11}Cr_2$ are the equilibrium

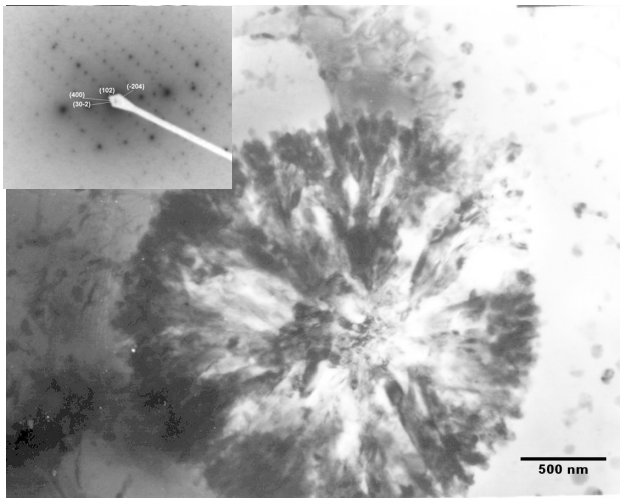


| Measured values | | Tabular values for the $Al_4Cr$ | |
|---|---|---|---|
| č.s. | $d_{vyp}/(10^{-10}\text{m})$ | (h k l) | $d_{hkl}/(10^{-10}\text{m})$ |
| 1 | 10.43 | 1 0 2 | 10.10 |
| 2 | 5.35 | 3 0 -2 | 5.25 |
| 3 | 4.40 | 4 0 0 | 4.34 |
| 4 | 5.13 | -2 0 4 | 5.05 |
| $\varphi_{1/2} = 80°$ | | $\varphi_{(102)a(30\text{-}2)} = 79.5°$ | |

**Figure 7:** Rosette-like spherolite in the specimen Al-2
**Slika 7:** Rozetasti sferoliti v vzorcu Al-2

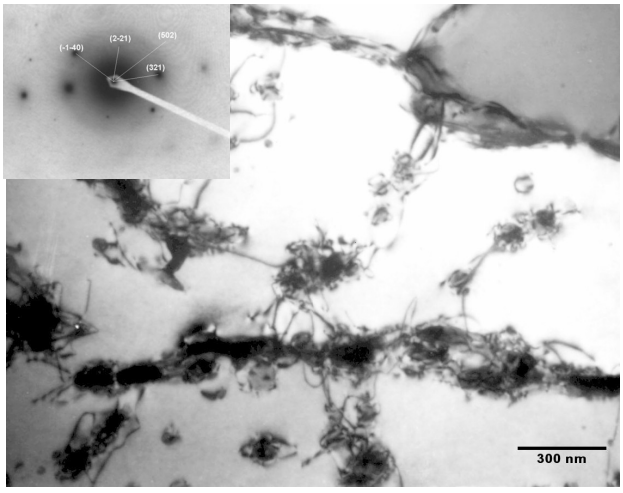


| Measured values | | Tabular values for the $Al_9Cr_4$ | |
|---|---|---|---|
| č.s. | $d_{vyp}/(10^{-10}\text{m})$ | (h k l) | $d_{hkl}/(10^{-10}\text{m})$ |
| 1 | 3.04 | 2 -2 1 | 3.04 |
| 2 | 2.43 | 3 2 1 | 2.43 |
| 3 | 1.64 | 5 0 2 | 1.69 |
| 4 | 2.27 | -1 -4 0 | 2.21 |
| $\varphi_{1/2} = 72°$ | | $\varphi_{(2\text{-}21)a(321)} = 74.5°$ | |

**Figure 8:** Semi-globular particles in the Al matrix in the specimen Al-2
**Slika 8:** Polglobularni delci v aluminijevi matici v vzorcu Al-2

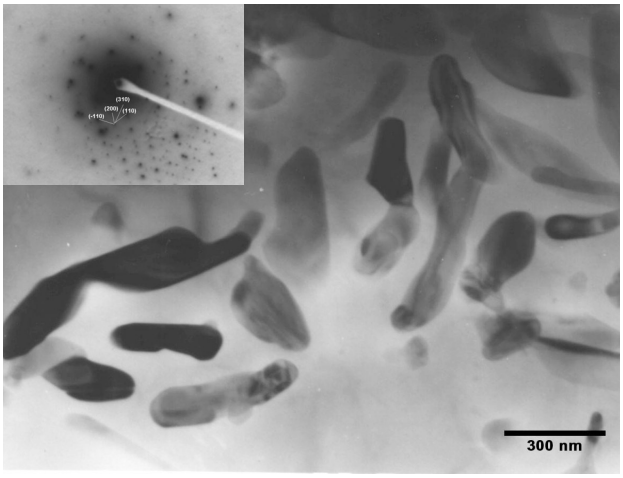


| Measured values | | Tabular values for the $Al_7Cr$ | |
|---|---|---|---|
| Č.s. | $d_{vyp}/(10^{-10}m)$ | (h k l) | $d_{hkl}/(10^{-10}m)$ |
| 1 | 9.20 | 2 0 0 | 9.83 |
| 2 | 6.85 | 1 1 0 | 7.06 |
| 3 | 4.45 | 3 1 0 | 4.95 |
| 4 | 6.85 | -1 1 0 | 7.06 |
| $\varphi_{1/2} = 74°$ | | $\varphi_{(200)a(110)} = 72.8°$ | |

**Figure 9:** The $Al_7Cr$ precipitates in the specimen Al-3
**Slika 9:** Izločki $Al_7Cr$ v vzorcu Al-3

phases for the pure Al–Cr system. However, at a higher concentration the $Al_{11}Cr_2$ phase is present at room temperature in the diagram [12], and only above 790 °C can this phase be expected to be an equilibrium aluminide in the alloy. However, it is expected to occur in the melt-spun ribbon, either as a direct consequence of the normal solidification or as a result of non-equilibrium freezing.

There is no unequivocal information concerning the $Al_7Cr$ aluminide. In a diagram in [11], the $Al_7Cr$ phase is shown as an isoconcentric intermetallic compound. On the other hand, the phase is shown in [12] to occur in some narrow concentration range. The stoichiometry 13:2 is slightly smaller that 7:1; thus, $\theta$-$Al_{13}Cr_2$ can probably be considered as a chromium-poor variant (Bertholide) of the $Al_7Cr$ aluminide.

Other phases with a higher chromium content ($Al_4Cr$, $Al_9Cr_4$) can be expected at room temperature only after slow solidification in the alloys with a high chromium content. At temperatures above 940 °C ($Al_4Cr$) and 1030 °C ($Al_9Cr_4$) the occurrence of both phases is also shifted to a lower chromium content.

During investigations of alloy processing, theories relating to the structure of the melt were suggested. For instance, it was determined that the structure of the solid alloy is in many cases also conserved to a limited extent in the liquid as a constituent with short-range order. The constituents with long-range orders of atoms were described as clusters on the basis of the "clusters theory" [15-17]. It is important that these clusters often have the same compositions as the nearest solid phase. In the rapidly solidified alloy the clusters (or the phases with a similar chemical composition) can be conserved to room temperature, and this is the principal explanation for their occurrence in the ribbons.

In addition, Selke [13] suggested that an "i-phase" occurred in the splat-quenched $Al_{85-x}Cu_xCr_{15}$ alloys; however, no information about its stoichiometry for the pure Al–Cr system was found so far. Therefore, it is practically impossible to estimate whether it corresponds to the identified phases in the Al–7%Cr alloy or not.

## 4 CONCLUSIONS

The microstructure of the slowly solidified alloy Al–7% Cr consists of the matrix, primary globular or semi-globular dendrites and intermetallic phases. The matrix is an Al solid solution and the intermetallic phases are mainly the compound $Al_7Cr$ ($Al_{13}Cr_2$).

The microstructure of RS ribbons consists of the matrix with a high dislocation density and of nano-crystalline phases of different size, shape and distribution. The matrix is a supersaturated solid solution in which many different phases occur. Some of them are semi-equilibrium, while the $Al_9Cr_4$ and $Al_4Cr$ phases are of a non-equilibrium origin. The RS ribbons processed by various conditions differ from each other mainly in terms of the quantity and the occurrence of non-equilibrium phases.

## 5 REFERENCES

[1] Tewari, S. N.: J. Mater. Sci. Lett. 11 (**1992**), 1020–1022
[2] Muller, B. A., Tanner, L. E., Perepezko, J. H.: Mater. Sci. Eng. A150 (**1992**), 123–132
[3] Zhang, X., Atrens, A.: Mater. Sci. Eng. A159 (**1992**), 243–251
[4] Era, H., Kishitake, K., Li, P.: Metall. Trans., 24A, (**1993**) 3, 751–756
[5] Kuoji, M. et al.: J. Mater. Sci. 29 (**1994**), 1449–1454
[6] Jurči, P.: PhD Thesis, MtF STU Trnava, 1996 (In Czech)
[7] Ehrstrom, J. C., Ponesu, A.: Mater. Sci. Engng., A186 (**1994**), 55–64
[8] Premkumar, M. K., Lawley, A., Koczak, M. J.: Mater. Sci. Engng., A174 (**1994**), 127–139
[9] Jones, H.: Mater. Sci. Engng., A375-377 (**2004**), 104–111
[10] Lieblich, M. et al.: Mater. Sci. Techn., 12 (**1996**), 25–33
[11] Web page: http://aluminium.matter.org.uk/content/html/eng/default.asp?catid=79&pageid=-884660481
[12] Smithells Metal Reference Book, 8th Edition, Elsevier, 2004
[13] Selke, H., Ryder, P. L.: Mater. Sci. Engng., A165 (**1993**), 81–87
[14] Shunk, I. A.: Constitution of Binary Alloys, Second Supplement, McGraw-Hill, New York, 1969
[15] Stewart, G. W., Benz, C. A.: Phys. Rev., 46 (**1934**), 703
[16] Frenkel, Ja. I.: Kinetic theory of liquids, Leningrad, 1975 (In Russian)
[17] Danilov, V. I., Rabčenko, I.V.: ŽETF 7, 1937, 1153 (In Russian)
[18] M. Hansen, K. Anderko: Constitution of binary diagrams, 1958

UDK 691.421:628.54
Original scientific article/Izvirni znanstveni članek

ISSN 1580-2949
MTAEC9, 41(6)289(2007)

# THE INFLUENCE OF DIFFERENT WASTE ADDITIONS TO CLAY-PRODUCT MIXTURES

## VPLIV RAZLIČNIH ODPADKOV NA IZHODNO SUROVINO ZA PROIZVODNJO OPEČNIH IZDELKOV

**Vilma Ducman, Tinkara Kopar**

Slovenian National Building and Civil Engineering Institute, Dimičeva 12, 1000 Ljubljana, Slovenia
vilma.ducman@zag.si

*Prejem rokopisa – received: 2007-07-09; sprejem za objavo – accepted for publication: 2007-10-22*

The potential use of four different wastes in the clay-based industry has been studied. The selected wastes were: stone mud from the stone-processing industry, paper mud, sawdust, and sludge from the polishing process for silicate igneous rocks. Waste, depending on its composition, can be used as i) an opening agent, when it contains a large amount of silica or ii) a pore-forming agent, when it contains combustible materials.

Mixtures of clay and different amounts of selected waste (up to the mass fraction of 50 %) were prepared. The influence of the addition of different wastes on drying and firing shrinkage was determined, as well as the water absorption, bulk density, bending and compressive strengths of fired samples.

We found that the addition of paper mud and sawdust improves the drying process by reinforcing the clay body structure, which counteracts cracking. It also significantly improves the thermal insulation properties. Additions of silica stone mud, as well as granite polishing sludge act as opening agents, which decrease the deformability of green as well as fired specimens.

Using waste in the production of clay-based products could represent a quite significant decrease in costs due to the replacement of basic raw materials with waste, and in some cases also the significant improvement of the quality of the final product.

Key words: industrial waste, paper mud, sawdust, polishing sludge, silica stone mud, clay products

V prispevku so predstavljene možnosti uporabe štirih različnih industrijskih odpadkov v opečni industriji, in sicer kremenov mulj, papirni mulj, žagovina in odpadek, ki nastaja pri poliranju silikatnih magmatskih kamnin. Odpadke glede na sestavo lahko dodajamo kot dodatke, ki povečujejo odprto poroznost, kadar vsebujejo večje količine kremena oziroma kadar vsebujejo organske komponente, ki zgorijo med žganjem, kot dodatke za povečevanje celotne poroznosti.

Pripravili smo mešanice gline in izbranih odpadkov (do masnega deleža 50 %). Določili smo vpliv teh dodatkov na skrčke pri sušenju in žganju ter na vpijanje vode, gostoto, upogibno in tlačno trdnost žganih izdelkov. Ugotovili smo, da dodatek papirnega mulja in žagovine izboljša proces sušenja, saj učvrsti strukturo nežganih proizvodov in tako preprečuje nastanek razpok. Prav tako znatno izboljša toplotno-izolacijske karakteristike opečnega izdelka. Kremenov mulj in odpadek pri poliranju granita sta dodatka, ki povečujeta odprto poroznost in zmanjšujeta skrčke pri sušenju in žganju in s tem možnost nastanka deformacij žganih proizvodov.

Uporaba odpadkov v opekarski industriji lahko pomeni znatno znižanje stroškov zaradi delne zamenjave osnovne surovine z odpadnim materialom; prav tako lahko v določenih primerih odpadki izboljšajo kakovost končnega proizvoda.

Ključne besede: industrijski odpadki, papirni mulj, žagovina, polirni odpadki, kameni mulj, opečni proizvodi

## 1 INTRODUCTION

Different industrial wastes could be quite successfully used in the clay-based industry; some of them have a positive effect on the process and/or on the final properties, others are simply used to replace the basic raw material and lower the cost of the production.

In this investigation four different industrial wastes were checked for their usability in the clay-based industry: silica stone mud from the stone-processing industry, paper mud, sawdust, and granite-like polishing sludge.

The sawdust is a by-product of freshly felled timber and therefore contains no solvents, adhesives or other components. Papermaking sludge is a residue in the paper industry, which mainly consists of paper fibres, kaolin, lime and water. The fibrous structure of both wastes has a favourable influence on the stability of the freshly extruded green ware during drying and so counteracts cracking. Besides a favourable effect on the process parameters, sawdust and paper-making sludge are combustible and they can be used as pore-forming agents. Products with increased porosity have better thermal insulation properties[1-5].

Silica stone mud is a secondary material that remains after the screening of stone aggregate in quarries. It contains a large amount of very fine silica sand, feldspar and clay. Waste granite-like mud is a residue material of polishing operations in the natural stone industry. It contains very fine particles of silicate igneous rocks and a residue of the grinding abrasives. Both wastes could be used as a filler (opening agent) in the clay-based industry due to the large amount of very fine silica sand, which decreases the plasticity of the clay and reduces its shrinkage on drying and firing[6-10].

In order to study the influence of selected waste materials on the production and final properties of clay bricks, different mixtures of clay and waste were prepared (see **Tables 1, 2, and 3** for the composition of the individual mixtures).

## 2 EXPERIMENTAL

### *2.1 Raw materials and test mixtures*

#### 2.1.1 Brick-making clay A

Clay taken from the production of masonry bricks from the eastern part of Slovenia was used. The clay can be classified as the chlorite-illitic type, with traces of montmorillonite and around the mass fraction $w$ = 38 % of quartz. The grain size distribution is as follows (in mass fractions): 18.1 % > 20 μm; 36.0 % 2–20 μm, and 45.8 % < 2 μm.

#### 2.1.2 Brick-making clay B

Clay taken from the production of masonry bricks from the southern part of Slovenia was used. The clay can be classified as chlorite-illitic type, with around $w$ = 23 % of quartz. The grain size distribution is as follows (in mass fractions): 22.5 % > 20 μm, 40.0 % 2–20 μm, and 37.5 % < 2 μm.

#### 2.1.3 Papermaking sludge

The papermaking sludge used was in the form of filter cake, with a water content of approximately $w$ = 52 %. It consists of the following inorganic components: calcite, kaolinite and illite. The loss on ignition at 500 °C is $w$ = 24 % and at 900 °C it is $w$ = 48 %.

#### 2.1.4 Sawdust

The sawdust was chopped to pieces of around 1 mm: 11.7 % of the particles were ≥ 1 mm, 76.7 % of the particles were between 1 mm and 0.2 mm, and 11.6 % of the particles were < 0.2 mm. The water content was 19.7 %. Sawdust consists of 99 % combustible substances. The loss on ignition at 500 °C was 98 % and at 900 °C it was 98.6 %.

#### 2.1.5 Silica stone mud

The waste silica mud contained about 35 % of quartz, the rest is clay and feldspar. It had the following grain size distribution in mass percent: 16.5 % > 20 μm, 34.9 % 2–20 μm, and 48.6 % < 2 μm. Silica stone mud also contains the swelling mineral montmorillonit.

#### 2.1.6 Granite-like polishing mud

The waste granite polishing mud contained about 30 % quartz; the rest is clay, feldspars, carbonates and a residue of SiC polishing tools. It had the following grain size distribution in weight percentage: 8.4 % > 20 μm, 75.3 % 2–20 μm, and 16.3 % < 2 μm.

### *2.2 Shaping, drying and firing of the test specimens*

The test specimens were shaped in a laboratory de-airing extruder at a vacuum of about 80 %, i. e., 20 kPa. During extrusion, a proper amount of water was added to the mixtures to avoid surface cracks on the test

**Table 1:** Mixtures of clay, papermaking sludge and sawdust and the average properties of laboratory-made test specimens
**Tabela 1:** Mešanice gline, papirnega mulja in žagovine ter pripadajoče lastnosti laboratorijsko pripravljenih vzorcev

| MIXTURE | **A1** | **A2** | **A3** | **A4** | **A5** | **A6** | **A7** |
|---|---|---|---|---|---|---|---|
| Clay content – clay A ($\varphi$/%) | 100 | 90 | 80 | 70 | 70 | 70 | 80 |
| Sawdust ($\varphi$/%) | | 10 | 20 | 30 | | 10 | 15 |
| Papermaking sludge ($\varphi$/%) | | | | | 30 | 20 | 5 |
| Shaping | | | | | | | |
| Water content based on dry mass ($w$/%) | 26.9 | 28.4 | 29.3 | 34.7 | 34.5 | 33.8 | 30.2 |
| Water content based on wet mass ($w$/%) | 21.2 | 22.1 | 22.6 | 25.7 | 25.7 | 25.2 | 23.2 |
| Shrinkage after drying (%) | | | | | | | |
| Measured along the prism length | 7.7 | 6.8 | 6.5 | 7.2 | 8.6 | / | 7.1 |
| Measured across the prism width | 6.4 | 6.5 | 6.4 | 7.5 | 9.6 | / | 6.7 |
| Firing temperature (°C) (±15) | 850 | 850 | 920 | 920 | 920 | 910 | 920 |
| Body density after firing (kg/dm$^3$) | 1.81 *1.85 | 1.69 | 1.65 | 1.44 | 1.59 | 1.58 | 1.63 |
| Water absorption (%) | 16.7 | 19.6 | 21.5 | 30.5 | 24.9 | 25.3 | 22.2 |
| Compressive strength (MPa) | | | | | | | |
| Prisms | 23.9 | 17.4 | 19.0 | 10.7 | 29.3 | 23.0** | 23.4 |

* fired at 920 °C, ** measured on cylinder / not determined

**Table 2:** Mixtures of clay and silica stone mud and average properties of laboratory-made test specimens
**Tabela 2:** Mešanice gline in kremenovega mulja ter pripadajoče lastnosti laboratorijsko pripravljenih vzorcev

| MIXTURE | **B1** | **B2** | **B3** | **B4** |
|---|---|---|---|---|
| Clay content – clay B ($w$/%) | 100 | 70 | 50 | 0 |
| Silica stone mud ($w$/%) | 0 | 30 | 50 | 100 |
| Shaping | | | | |
| Water content based on dry mass ($w$/%) | 25.1 | 31.6 | 30.0 | 52.9 |
| Water content based on wet mass ($wt$/%) | 20.0 | 23.1 | 23.1 | 34.6 |
| Shrinkage after drying (%) | | | | |
| Measured along the prism length | 8.4 | 10.5 | 11.6 | 15.4 |
| Measured across the prism width | 7.3 | 8.8 | 11.2 | 15.6 |
| Firing at temperature (°C) (±15) | 900 | 900 | 900 | 900 |
| Shrinkage after firing (%) | | | | |
| Measured along the prism length | 1.4 | 0.9 | 1.2 | 1.6 |
| Measured across the prism width | 1.2 | 1.1 | 1.4 | 1.4 |
| Body density after firing (kg/dm$^3$) | 1.96 | 1.90 | 1.86 | 1.79 |
| Water absorption (%) | 9.2 | 10.6 | 12.5 | 16.8 |
| Clinker point | | | | |
| Temp. of firing where water absorption amounts to $w$ = 6 % | 1017 | 1029 | 1042 | 1095 |
| Bending strength (MPa) | | | | |
| Measured on prisms | 22.0 | 20.7 | 20.0 | 6.3* |
| Compressive strength (MPa) | | | | |
| Measured on prisms | 62.5 | 52.5 | 50.7 | /* |

*cracks visible before testing

**Table 3:** Mixtures of clay and granite stone mud and average properties of laboratory-made test specimens
**Table 3:** Mešanice gline in odpadka od poliranja granite ter pripadajoče lastnosti laboratorijsko pripravljenih vzorcev

| MIXTURE | C1 | C2 | C3 | C4 | C5 |
|---|---|---|---|---|---|
| Clay content – clay B (*w*/%) | 100 | 95 | 90 | 80 | 70 |
| Granite like stone mud (*w*/%) | 0 | 5 | 10 | 20 | 30 |
| Shaping | | | | | |
| Water content based on dry mass (*w*/%) | 26.1 | 27.0 | 28.3 | 32.6 | 34.6 |
| Water content based on wet mass (*w*/%) | 20.7 | 21.3 | 22.1 | 24.6 | 25.7 |
| Shrinkage after drying (%) | | | | | |
| Measured along the prism length | 8.7 | 8.5 | 9.5 | 9.8 | 9.3 |
| Measured across the prism width | 7.5 | 6.6 | 7.6 | 8.7 | 7.8 |
| Firing at temperature (°C) (±15) | 915 | 915 | 915 | 915 | 915 |
| Body density after drying (g/cm$^3$) | 2.05 | 2.02 | 1.98 | 1.88 | 1.80 |
| Shrinkage after firing (%) | | | | | |
| Measured along the prism length | 1.0 | 1.5 | 1.4 | 1.5 | 1.3 |
| Measured across the prism width | 1.1 | 1.5 | 1.4 | 1.7 | 1.4 |
| Body density after firing (g/cm$^3$) | | | | | |
| Measured on prisms | 2.00 | 1.96 | 1.92 | 1.84 | 1.76 |
| Water absorption after firing (%) | | | | | |
| Measured on prisms | 8.8 | 9.6 | 10.7 | 12.8 | 16.6 |
| Clinker point | | | | | |
| Temp. of firing where water absorption amounts to $w$ = 6 % | 1008 | 1022 | 1037 | 1045 | 1052 |
| Bending strength (MPa) | | | | | |
| Measured on prisms | 16.1 | 15.6 | 16.7 | 13.5 | 10.4 |
| Compressive strength (MPa) | | | | | |
| Measured on prisms | 86.2 | 77.6 | 78.5 | 71.7 | 62.4 |

specimens and to maintain a Pff number of 1.4 (±0.1) – see **Tables 1, 2, and 3**.

The test specimens were dried for 7 d in ambient room conditions, followed by 24 h at 60 °C and 8 h at 100 °C in a dryer. The dried samples were then fired for 4 h in a laboratory kiln at selected temperatures using heating rates of 80 °C/h up to 400 °C, and 50 °C/h between 400 °C and the final temperature. These firing conditions are similar to those generally applied in the brick-making industry.

### 2.3 Test methods

The particle size distribution of the tested clays was determined by sieving it down to 90 µm. Below 90 µm, the sedimentation method was applied using a Quantachrome Microscan II apparatus. The Quantachrome Microscan II apparatus was also used to determine the particle size distribution of the silica stone mud and the granite polishing mud.

The mineral components of both clays and both stone wastes were determined by X-ray diffractometry using a Phillips Norelco apparatus.

The linear shrinkage, ceramic body density, water absorption (by boiling test specimens in water for 2 h), and compressive strength were determined on fired samples of (160 × 50 × 25) mm prisms.

The pore size and the pore size distribution were measured using Hg porosimetry. The maximum pressure when filling was 206,843 kPa, $\theta$ 130° and $\gamma$ 485 · 10$^{-5}$ N/cm.

## 3 RESULTS AND DISCUSSION

### *3.1 The addition of sawdust and papermaking sludge*

The properties related to shaping, drying and firing are listed in **Table 1**. The shaping parameter (i.e., the water content) shows that with the additions of pore-forming agents, more water should also be added to mixtures to avoid surface cracks during shaping. The shrinkage after drying is reduced with the addition of sawdust; most significantly for the specimen with the volume fraction of 20 % of sawdust, where the shrinkage after drying is 6.5 % in comparison to pure clay, where the shrinkage is 7.7 % (specimen A1). In contrast, the shrinkage after drying with the addition of papermaking sludge is increased to 8.6 % when the volume fraction of 30 % of the papermaking sludge is added. The decrease in the drying shrinkage is favourable because it reduces the danger of cracking during drying.

In **Figure 1** the firing analysis from the gradient kiln is presented for pure clay and the mixture A5 containing the mass fraction of 30 % of paper-making sludge. It is clear that the sludge addition increases the water absorption of the specimen, which is to be expected due to its pore-forming action. The shrinkage after firing is lower for the specimen with the sludge, which is a favourable effect since it contributes to the dimensional stability during firing.

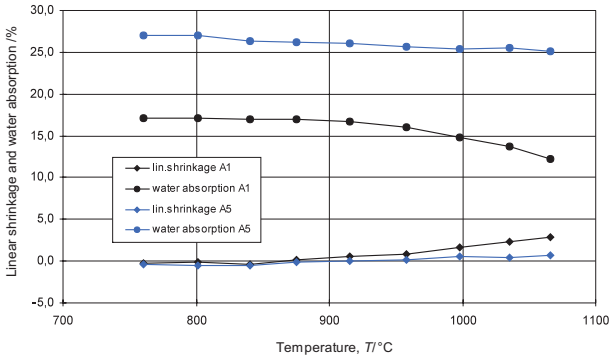


**Figure 1:** Determination of the effect of firing temperature on the linear shrinkage and water absorption by firing in a gradient kiln for samples A1 and A5
**Slika 1:** Vpliv temperature žganja na skrček in vpijanje vode (žganje v gradientni peči) vzorcev A1 in A5

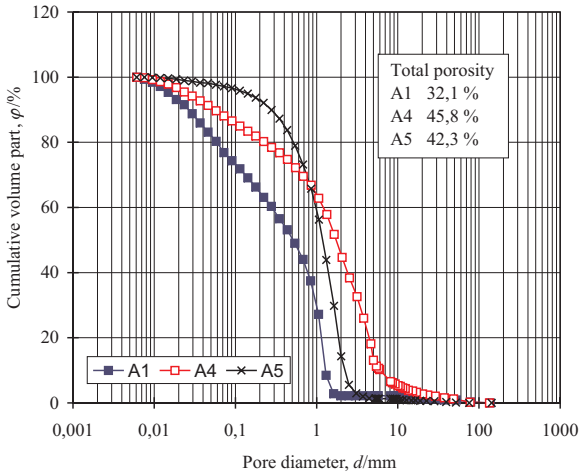


**Figure 2:** Pore size distribution for samples A1, A4, and A5
**Slika 2:** Porazdelitev velikosti por vzorcev A1, A4 in A5

After firing the body density is significantly reduced with the addition of pore-forming agents, especially when sawdust is added. The density of sample A4 with 30 % of added sawdust is 1.44 kg/dm$^3$, whereas the density of the clay without additives is 1.85 kg/dm$^3$. The distribution of the porosity for samples A1, A4, and A5 is presented in **Figure 2**. In the case of clay without additives (mixture A1) the pore size distribution is uniform. The total porosity in the volume fraction is 32.1 % and over 95 % of the pores are smaller than 3 µm. The addition of sawdust (A4) creates larger pores, where 35 % of the pores are larger than 3 µm and the total porosity is 45.8 %. The addition of papermaking sludge (A5) influences the formation of finer pores, where with a total porosity of 42.3 % over 95 % of the pores are smaller than 3 µm.

The reduction in density also influences the compressive strength: from 23.9 MPa for pure clay (fired at 850 °C) to 10.7 for the specimen with 30 % of sawdust. From comparisons of the compressive strengths for specimens A4 and A5 (30 % of sawdust and 30 % of papermaking sludge, respectively), as well as A6 and A7, both with the addition of pore-forming agents, it is clear that with the addition of papermaking sludge, an increase in the compressive strength is observed. This was ascribed to the presence of calcite in the papermaking sludge, as already described in the literature, where it was observed that the addition of 15 % of calcite increases the compressive strength of the clay body by up to 40 %, and at the same time it practically doubles the bending-tensile strength[11].

As previously described[4], the optimal results regarding shrinkage, compressive strengths and body density after firing are obtained with a combination of both pore-forming agents.

### *3.2 The addition of silica stone mud*

The properties of the clay mixture with silica stone mud are presented in **Table 2**. Mixtures with silica stone

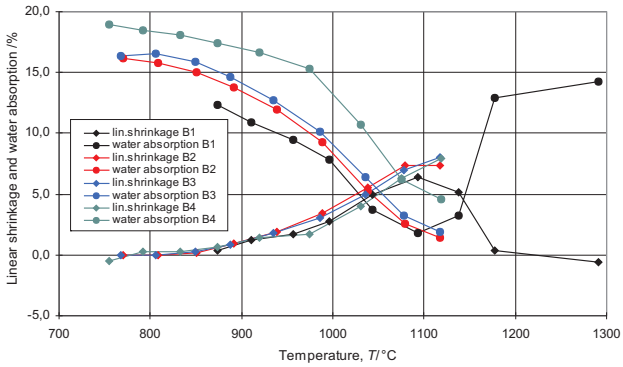


**Figure 3:** Determination of the effect of firing temperature on the linear shrinkage and water absorption by firing in a gradient kiln for samples of series B
**Slika 3:** Vpliv temperature žganja na skrček in vpijanje vode (žganje v gradientni peči) vzorcev serije B

mud that contain swelling minerals required quite a large content of water for proper shaping. The requirement for a larger amount of water is generally discouraging because this water should be removed in the drying process and this consequently increases the shrinkage after drying: from 8.4 % for pure clay to 15.4 % for pure silica stone mud. A high shrinkage introduces cracks into the green body, which was observed in specimen B4. This sample was prepared from pure silica stone mud, and the water content required for the extrusion amounted to 52.9 %.

From **Figure 3**, which presents the firing analysis in a gradient kiln, it is clear that the addition of mud significantly influences the water absorption's dependence on firing temperature, but only slightly influences the shrinkage after firing. The compressive strength of the fired specimen decreases with the silica stone mud additions, from 62.5 MPa for pure clay to 50.7 MPa when 50 % of silica stone mud is added.

### *3.3 The addition of granite-like stone mud*

The properties of the clay mixtures with granite-like polishing waste are presented in **Table 3**. Mixtures with

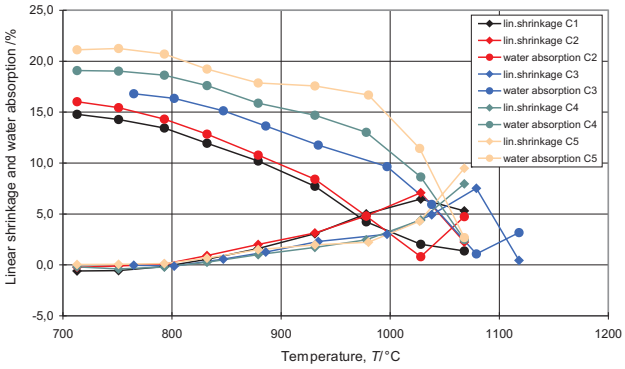


**Figure 4:** Determination of the effect of firing temperature on the linear shrinkage and water absorption by firing in a gradient kiln for samples of series C
**Slika 4:** Vpliv temperature žganja na skrček in vpijanje vode (žganje v gradientni peči) vzorcev serije C

waste additions require more water for proper shaping and consequently the linear shrinkage after drying increases from 8.7 % for the mixture without granite-like stone mud to 9.3 % for the mixture containing the mass fraction of 30 % mud. The effect is not pronounced for mixtures with up to 10 % of mud addition.

The firing analysis in a gradient kiln showed that the addition of mud significantly increased the water absorption and that it reduced the shrinkage of the basic clay (**Figure 4**). The addition of mud increased the water absorption of the test specimens and decreased their body density and compressive strength after firing. The decrease in mechanical properties is more significant with a larger amount of mud, when for samples containing up to 10 % of mud addition only a slight decrease in mechanical properties can be observed.

## 4 CONCLUSIONS

Many wastes, depending on their properties and the type of clay, can be successfully used in the brick-making industry. The clay designated as A contains traces of the swelling mineral montmorillonite, which contributes to the sensitivity to cracking of the products on drying. The addition of sawdust and papermaking sludge to brick-making clay favourably influences the process of shaping and drying due to the fibrous structure, which strengthens the green body and prevents the final products from cracking on drying. The addition of sawdust greatly increases the porosity of the fired body and therefore also significantly reduces the compressive strength. Papermaking sludge additions slightly increase the porosity and at the same time introduce finer pores, whose distribution is more homogeneous, thus lowering the compressive strength only slightly. At the same time, if paper sludge contains calcite, which is the case here, it contributes to an improvement in the mechanical properties of the fired clay products. With the optimal combination of paper-making sludge and sawdust (the amount of both wastes in the volume fraction is up to 30 % ) porous clay products can be achieved with almost the same mechanical properties as for the basic brick-making clay.

The addition of silica stone mud that contains the swelling mineral montmorillonite requires a larger amount of water for shaping than the basic clay, and this amount of water will evaporate during the process of drying, which can introduce cracks into the green product. The use of such a stone mud is therefore limited. If silica stone mud was used in the clay-based industry anyway, great attention should be paid to the drying phase in order to avoid cracks.

Granite-like polishing waste facilitates shaping, but it also makes the basic clay more sensitive to drying, especially when a larger amount is added. It also decreases the mechanical properties of the products. Both effects are not so pronounced when up to the mass fraction of 10 % of mud is added.

The use of different wastes in the clay-based industry can have, in some cases, a positive impact on the final properties of clay products. In other cases it can be used as a substitute for basic raw materials, which can contribute to a significant saving in natural resources, and at the same time to a reduction in the amount of landfill

### Acknowledgements

The research work described in this paper was supported by the companies Termit d.d. and Wienerberger Opekarna Ormož. Part of the work is the result of the European project **POLISHCOVERINGS – *Development of an efficient and environmentally friendly polishing process for floor and wall coverings*** (Project number*: CRAFT-1999-70904*)

## 5 REFERENCES

[1] K. Junge, Ziegel Industrie, 1 (**1994**), 35–38
[2] D. Hauck, E. Jung, Ziegel Industrie Jahrbuch, 1991, 108–121
[3] K. Junge, N. Pauls, Ziegel Industrie Jahrbuch, 1994, 90–96
[4] V. Ducman, T. Kopar, Sawdust, Ind. ceram., 21 (**2001**) 2, 81–86
[5] E. Rimpel, T. Schmedders, Ziegel Industrie Jahrbuch, 1996, 174–206
[6] U. Hahn, Ziegel Industrie, 9 (**1989**), 458–464
[7] M. Rickli, U. Eggenberger, T. Peters, Ch. Meyer, Th. Mumenthaler, Ziegel Industrie, 12 (**1998**), 818–827
[8] F. Andreola, L. Barbieri, A. Corradi, I. Lancellotti, American Cer. Soc. Bulletin, 3,83 (**2004**), 9401–9408
[9] V. Ducman, T. Kopar, Ind. ceram., 24 (**2004**) 1, 8–12
[10] V. Ducman, T. Kopar, E. Sanchez, Ind. ceram., 25 (**2005**) 3, 164–169
[11] M. Elwan, E. A. El-Alfi, H. El Didamony, Ind. Ceram., 21 (**2001**) 2, 87–90

UDK 669'25'26:611.314
Original scientific article/Izvirni znanstveni članek

ISSN 1580-2949
MTAEC9, 41(6)295(2007)

# ELECTROCHEMICAL AND MECHANICAL PROPERTIES OF COBALT-CHROMIUM DENTAL ALLOY JOINTS

## ELEKTROKEMIJSKE IN MEHANSKE LASTNOSTI RAZLIČNIH SPOJEV STELITNE DENTALNE ZLITINE

**Rok Zupančič[1], Andraž Legat[2], Nenad Funduk[1]**

[1]Department of Prosthodontics, University of Ljubljana, Faculty of Medicine, Division of Dental Medicine, Ljubljana, Slovenia
[2]Slovenian National Building and Civil Engineering Institute, Ljubljana, Slovenia
rok.zupancic@mf.uni-lj.si

*Prejem rokopisa – received: 2007-09-19; sprejem za objavo – accepted for publication: 2007-10-18*

In dentistry cobalt-chromium alloys are frequently used for partial denture frameworks. For fabrication of some complex frameworks, separate metal segments have to be joined. The longevity of these restorations is limited due to the mechanical or corrosive failure of the joints. The purpose of this study was to determine which joining method offers the best properties to cobalt-chromium alloy frameworks. Intact specimens, brazed and two types of laser-welded joints were compared for their electrochemical and mechanical characteristics. Electrochemical impedance spectroscopy and potentiodynamic polarization in two artificial saliva solutions were used to assess basic corrosion parameters and tensile strength of brazed and laser welded specimens was measured. The fracture surfaces and corrosion defects were examined in a scanning electron microscope. The average tensile strength of brazed joints was significantly greater than the tensile strength of both types of laser-welded joints. When laser welding was used, successful joining was limited to the peripheral aspects of the weld. The welding technique did not affect significantly the joint tensile strength. Electrochemical measurements indicated that primarily due to differences in pasivation ability, the corrosion resistance of the laser-welded joints was better than that of the brazed.

Key words: brazing, laser welding, dental alloys, corrosion, strength

V zobni protetiki pogosto izdelamo ogrodja fiksnih in snemnih protetičnih izdelkov iz stelitnih (kobalt-kromovih) zlitin. Pri kompleksnejših konstrukcijah je treba spojiti posamezne dele ogrodja. Trajnost protetičnega izdelka pogosto omejujejo mehanske in korozijske poškodbe spojev. Namen te raziskave je bil ugotoviti, s katerim načinom spajanja dobimo korozijsko in mehansko najbolj odporne spoje. Primerjali smo lotanje in dva načina laserskega varjenja. Osnovne korozijske parametre smo ugotovili z elektrokemijsko potenciodinamsko polarizacijo in elektrokemijsko impedančno spektroskopijo v dveh različnih raztopinah umetne sline. Pri lotanih in lasersko varjenih vzorcih smo izmerili natezno trdnost. Lomne ploskve in korozijske poškodbe smo pregledali z vrstičnim elektronskim mikroskopom. Povprečna natezna trdnost lotanih spojev je bila značilno višja od trdnosti obeh skupin lasersko varjenih spojev. Z laserskim varjenjem smo uspešno spojili le površinsko plast vzorcev. Način laserskega varjenja ni značilno vplival na natezno trdnost spojev. Elektrokemijske lastnosti spojev kažejo, da so, predvsem zaradi razlike v sposobnosti pasivacije, lasersko varjeni spoji korozijsko obstojnejši od lotanih.

Ključne besede: lotanje, lasersko varjenje, dentalne zlitine, korozija, trdnost

## 1 INTRODUCTION

Cobalt-chromium (Co-Cr) alloys are frequently used for fixed and removable partial denture frameworks.[1–3] In the fabrication of some complex frameworks and in repairs or additions, separate metal segments of the framework have to be joined.[2] The longevity of these restorations is limited due to the mechanical or corrosive failure of the joints.[4–6] Several joining techniques are available but brazing and laser welding are most commonly used.

Brazing is a process in which a molten filler metal wets and fills the gap between the parent metal surfaces.[3] The filler metal has a lower melting point than the parent metal.[3] In welding, the parent metals fuse and form the joint with or without a filler alloy.[2] Conventional heat sources tend to produce excessive thermal damage to prosthodontic restorations and are therefore not used in dentistry.[2] Laser welding has recently gained popularity, mostly because it is simpler and less time consuming than brazing.[7] For brazing Co-Cr alloys, a Co-Cr alloy with a lower melting point or a noble alloy serves as a filler.[5–8] Gold-based filler alloys are often used because their melting points are well below those of Co-Cr alloys.[5–8] Research has shown that these joints have poor mechanical properties and corrosion resistance[5,7,9] and exhibit a significantly lower tensile strength than laser welded joints.[7,9] Angelini et al [5] compared the corrosion resistance of Co-Cr alloy brazing done with a gold-based filler and a Co-Cr filler and concluded that Co-Cr filler is more appropriate than gold-based filler.

Co-Cr dental alloys have an excellent corrosion resistance, which is provided by a thin adherent layer of chromium-based oxides on the surface.[5,6,10] Considerable defects caused by corrosion tend to appear primarily in the joints. Beside specific problems related to crevice forming, joining of 2 metals with different corrosion potentials can form a galvanic cell. [11] In such a case, the less noble metal acts as a main anode, and it could exhibit a relatively high dissolution rate.[12,13] Such problems with brazed joints, caused by the dissimilar composition of the filler and the parent metals are reported.[14–16] Corrosion not only results in a poor esthetic outcome, but can also compromise physical properties

and induce biological irritation in form of an allergic reaction, lichen planus, or some other soft tissue inflammation.[5,12,17,18]

Corrosion properties are commonly assessed by various types of electrochemical measurements.[13,19] Electrochemical potentiodynamic polarization (EPP) techniques are often used, providing general information about the corrosion resistance and susceptibility, such as the general corrosion rate, the range of passivation, and the break-down potential.[12,20] These results should be carefully considered since with EPP the information is not obtained in stationary conditions.[20] In rather passive systems with relatively low corrosion rates (application of noble metals or systems with protective coatings) more reliable information can usually be gained from electrochemical impedance spectroscopy (EIS) measurements.[12,20] EIS applies sinusoidal voltage signal of relatively small amplitudes (usually a few tens of mV) and the conditions of the electrodes are only slightly disturbed.[12,21] Beside the general corrosion properties of an investigated system, specific information about underlying electrochemical mechanisms can also be obtained from the measured impedance spectra.[20,21]

These electrochemical methods have been successfully implemented in several investigations of various corrosion problems in dentistry.[21–25] Electrolyte solutions, such as artificial saliva, are often used as the corrosion medium because their electrochemical properties are similar to those of the natural saliva.[26] The level of corrosion resistance of brazed and laser-welded Co-Cr dental alloy joints has so far been determined merely with microscopic assessment of corrosion defects. Electrochemical properties of different joints have not yet been compared quantitatively.

Most studies investigating the mechanical resistance of various joints showed that laser welds have higher tensile strength than soldered or brazed joints using noble solders.[7,9,26,27] However, laser welds are more prone to fatigue damage than brazed joints.[9]

Short laser pulses which heat metal beyond the melting point are used for laser welding. The amount of energy released in each laser pulse is controlled by setting the welding parameters (voltage, pulse duration, and focus diameter).[4] Spots where laser pulses are applied cool rapidly and the welding depth is sometimes relatively shallow in comparison with the diameter of the welded object.[28,29] More powerful laser pulses not only deepen the weld penetration, but also increase porosity.[2,28,29] In an attempt to overcome this problem, different joint designs have been proposed.[2] If adjacent joint-forming surfaces are ground so as to form the shape of the letter X, they can be laser-welded starting from the center and the joint is built towards the surface of the object.[2] In the process, metal is added to the joint by a filler wire with a composition equal, or very similar to the parent metal.

The aim of this study was to determine which method of joining Co-Cr alloy framework segments produces joints with the best strength and corrosion resistance. The joining methods used were brazing with a Co-Cr filler and laser welding with 2 different joint designs.

## 2 MATERIAL AND METHODS

52 cylindrical specimens with a diameter of 2 mm and the length of 35 mm were cast in a Co-Cr alloy (Remanium GM 380; Dentaurum), following the procedures recommended by the alloy manufacturer. The alloy composition is shown in **Table I**. 16 specimens were selected for electrochemical measurement, and divided into 4 groups of 4 specimens each. In the intact group, the specimens were left as cast. The specimens of the remaining 3 groups were sectioned at the center, perpendicular to their long-axis, using a 0.6 mm separating disk and subsequently re-joined by brazing (brazing group) and laser welding, using an X- or I-shaped joint design (X laser and I laser groups, respectively).

36 specimens were selected for tensile strength testing, and divided into 3 groups in which specimen pairs ($n$ = 6) were to be joined by brazing or laser welding, using an X- or I-shaped joint design.

To achieve a standard gap for the brazing group, a 0.3 mm metal shim was placed between the two halves of specimens. The shim was removed once the specimens were positioned and invested in the phosphate-bonded investment. Flux was applied, and a Co-Cr solder was used as the filler metal. Its composition is shown in **Table I**. The assembly was pre-heated to 750 °C and torch brazed at 1180 °C, following the procedures recommended by the manufacturer of the solder.

For laser welding the I-shaped joint design, the joint surfaces of specimens were straight and placed in tight contact with each other. An Nd:YAG laser with the wavelength of 1064 nm was used with the following settings: voltage of 290 V, pulse duration of 10 ms, and weld spot diameter of 0.7 mm. A weld spot overlap of approximately 75 % was used, so that the joint was

**Table I:** Composition (*w*/%) of Remanium GM 380 alloy, Co-Cr solder, and filler wire
**Tabela I:** Sestava zlitine Remanium GM 380, Co-Cr lota in varilne žice v masnih deležih (*w*/%)

| | Co | Cr | Mo | Mn | Ni | C | Fe | Si | N | B | Nb |
|---|---|---|---|---|---|---|---|---|---|---|---|
| GM 380 alloy | 64.6 | 29 | 4.5 | <1 | – | <1 | – | <1 | <1 | – | – |
| Co-Cr solder | 61 | 28.5 | 3.5 | – | – | <1 | 1.5 | 4 | – | 1 | – |
| filler wire | – | 22.1 | 9.1 | – | 63.8 | – | 1 | – | – | – | 3 |

formed with 25 pulses per specimen. These laser conditions were chosen to simulate typical laboratory procedures for welding of Co-Cr dental alloys.[2,7,27]

With the X-shaped laser welding design the joint surfaces were ground to form the shape of the letter X if viewed from the side. During grinding, the surfaces were cooled with 75 % ethanol. The tip was rounded with a hand instrument to facilitate the alignment of the halves. Laser welding was performed using pulses of lower energy (settings: 255 V, 4.5 ms, 0.9 mm) because no deep weld penetration was required for this joint design. A Co-Cr filler wire was used to complete the joints. The composition of the wire is shown in Table I. Specimens were polished using conventional laboratory procedures[2] for removable partial denture frameworks with silicone polishers and polishing paste for Co-Cr alloys. The final joint diameter varied slightly due to the custom finishing.

The corrosion parameters were assessed by electrochemical potentiodynamic polarization (EPP) and electrochemical impedance spectroscopy (EIS). Since it was expected that the investigated electrochemical systems would exhibit relatively low corrosion activities, the polarization potential in EPP measurements were changed in a wide interval from cathodic to anodic region (–0.5 V vs *E*corr to +2 V vs *E*corr). From measured potentiodynamic curves, the corrosion current densities and break-down potentials were determined. In EIS measurements, the sinusoidal voltage signal with an amplitude of 10 mV in the frequency interval between 10 mHz and 5 kHz was applied. Significant parameters, as the total impedance ($|Z_0|$) and the polarization charge-transfer resistance ($R_{CT}$), were estimated from the measured spectra. The working electrode was always the specimen with a saturated calomel electrode serving as a reference electrode and a graphite electrode as a counter electrode. Fusayama type artificial saliva [30] was used as the corrosion medium. Its pH value is 4.65 and it has the following composition: NaCl 0.4 g/L, KCl 0.4 g/L, $CaCl_2 \cdot 2H_2O$ 0.795 g/L, $NaH_2PO_4$ 0.69 g/L and urea 1 g/L. A potentiostat (PC3/750; Gamry Instruments Inc) with the appropriate software (CMS 100 and CMS 300) was used for the experiment.

The joined specimens were tested in tension. The total length of the specimens was 7 cm, which allowed for secure fixation in the testing machine (Z 030; Zwick GmbH & Co). The joint diameter was measured with each specimen using an electronic caliper having an accuracy of 0.01 mm. The determined value was used to compute the tensile strength of the joints by the formula $\sigma = F/\pi r^2$, where $\sigma$ is the tensile strength, $F$ is the load at fracture and $r$ is the half-diameter of the joint.[3] Tensile tests were performed under constant extension rate of 0.008 $s^{-1}$ (relative extension) according to the standard EN 10002-1.[31] A 30kN load cell was used (KAP-TC, class 0.05; Zwick GmbH & Co) with the software (testXpert V10.11) provided by the manufacturer.

The data were statistically analyzed using a 1-way analysis of variance (ANOVA) and Scheffé post hoc tests. Differences between groups were regarded as significant at $\alpha = 0.05$. After mechanical and electrochemical testing the fracture surfaces and corrosion defects were analyzed by scanning electron microscopy (JSM–5500; JEOL), whereas the longitudinal sections were studied under a metallographic optical microscope (Neophot 22, Carl Zeiss AG).

## 3 RESULTS

Potentiodynamic curves obtained for intact alloy and different joints are shown in **Figure 1**. The curves of intact alloy and laser-welded joints are similar as all of them contain rather steep and nearly straight sections up to approximately 800 mV versus saturated calomel electrode. Very low dependence of electrochemical current on the applied potential in this region indicates a nearly passive state. Beyond these potentials, the so-called break-down potentials, there are distinct transitions to active corrosion, where measured currents start to increase rapidly. The potentiodynamic curve corresponding to the brazed joint shows that the measured current increased continuously and no distinct passive region was observed. The differences in break-down potentials between groups were statistically analyzed and found to be significant ($P = 0.036$), with the brazed joint having much lower average break-down potential (544 mV) than other specimens (pooled

**Table II:** Mean values and standard deviations (SD) of corrosion potentials ($E_{corr}$), break-down potentials ($E_{bd}$), corrosion current densities ($I_{cor}$), total impedances at lowest frequency ($|Z_0|$) and estimated polarization charge-transfer resistances ($R_{CT}$)
**Tabela II:** Povprečne vrednosti in standardne deviacije (SD) korozijskih potencialov ($E_{corr}$), porušitvenih potencialov ($E_{bd}$), gostote korozijskega toka ($I_{cor}$), impedance pri najnižji frekvenci ($|Z_0|$) in ocene polarizacijske upornosti ($R_{CT}$)

| | mean $E_{corr}$ (mV) | SD $E_{corr}$ (mV) | mean $E_{bd}$ (mV) | SD $E_{bd}$ (mV) | mean $I_{corr}$ (μA/cm²) | SD $I_{corr}$ (μA/cm²) | mean $\|Z_0\|$ (kΩ) | SD $\|Z_0\|$ (kΩ) | mean $R_{CT}$ (kΩ) | SD $R_{CT}$ (kΩ) |
|---|---|---|---|---|---|---|---|---|---|---|
| intact | –462.3 | 111.7 | 758.3 | 73.6 | 0.10 | 0.05 | 182.9 | 38.0 | 75.1 | 10.8 |
| brazing | –409.9 | 32.0 | 543.8 | 298.0 | 0.07 | 0.04 | 80.9 | 37.3 | 7.1 | 5.1 |
| I laser | –560.2 | 9.7 | 875.5 | 32.4 | 0.22 | 0.14 | 140.1 | 30.3 | 21.5 | 4.0 |
| X laser | –555.0 | 29.5 | 885.0 | 84.4 | 0.16 | 0.06 | 173.6 | 16.2 | 29.5 | 6.0 |

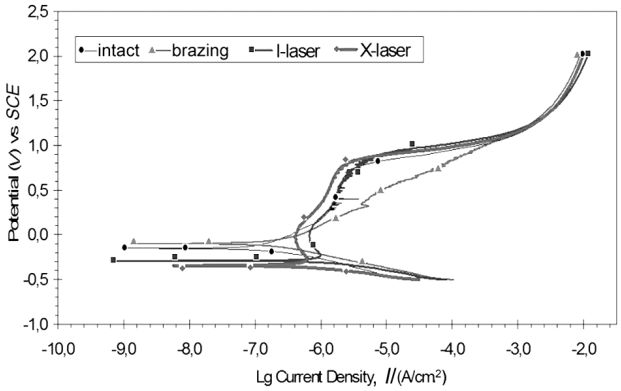


**Figure 1:** Potentiodynamic curves for different joints and intact alloy
**Slika 1:** Potenciodinamske krivulje za različne spoje in intaktno zlitino

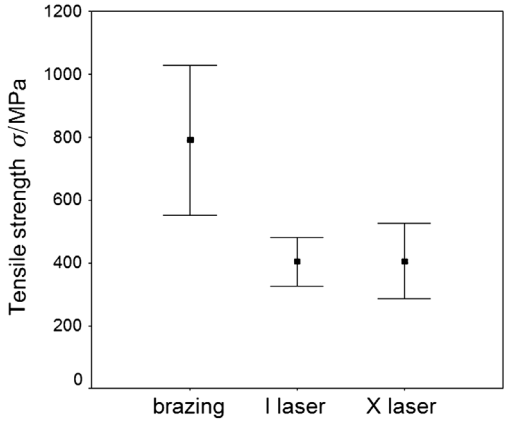


**Figure 3:** Means and standard deviations of tensile strength of the different joint types
**Slika 3:** Povprečne vrednosti in standardne deviacije natezne trdnosti različnih spojev

average 840 mV). All corrosion current densities were very low (from $10^{-7}$ to $10^{-6}$ A/cm$^2$). Exact values of corrosion current densities were calculated by the extrapolation of the Tafel slopes[19] however, they are generally represented as the intersections of anodic and cathodic curves (**Figure 1**). Estimated values of the corrosion potentials, corrosion current density, and break-down potentials are shown in **Table II**.

The electrochemical impedance spectra generally confirmed the observation drawn from the electrochemical potentiodynamic measurements. Impedance spectra are presented as Nyquist plots in **Figure 2**. Total impedance at the low frequency range is generally related to the corrosion resistance. The impedances at the lowest frequency $|Z_0|$ and estimated values of the polarization charge-transfer resistance $R_{CT}$ are shown in **Table II**.

The results obtained from EPP measurements and those from EIS measurements were in agreement. Both of them clearly expressed higher corrosion resistance of the laser-welded joints compared to the corrosion resistance of the brazed joints. SEM analysis of the specimens confirmed the results of the electrochemical measurements. The most pronounced corrosion damage was at the brazed joints, located primarily at the parent metal. Corrosion damage of the intact alloy and the laser-welded joints was minor and mostly located at certain defects on surfaces, such as inclusions or scratches.

The mean value (standard deviation) for the tensile strength of brazed joints was 792 (238.5) MPa. This was significantly ($P$ = 0.004) greater than the tensile strength of both types of laser-welded joints. The mean values for I-shaped and X-shaped joint designs were 404 (76.7) MPa and 405 (120.4) MPa, respectively. These are shown in **Figure 3**. All specimens, regardless of the joining technique, fractured in the joints. The strength of the laser-welded joints did not depend significantly on the joint design used. SEM examination, however, revealed differences in the effective cross-sections joined. The fracture surfaces of brazed joints were relatively smooth and they exhibited a fine grained partially ductile nature (**Figure 4**). Fracture surfaces of the I-shaped laser-welded joints showed that only peripheral aspects of these specimens were successfully joined, since under the surface there were some voids

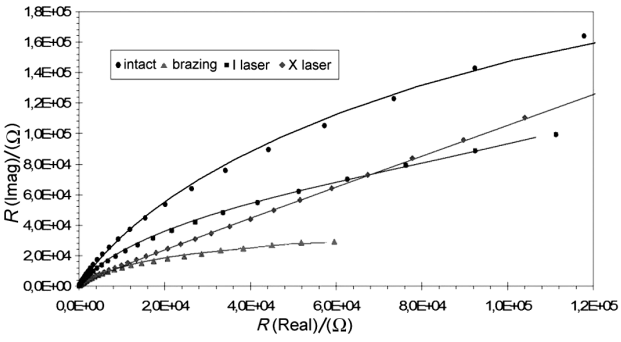


**Figure 2:** Nyquist plots for different joints and intact alloy
**Slika 2:** Nyquistovi diagrami za različne spoje in intaktno zlitino

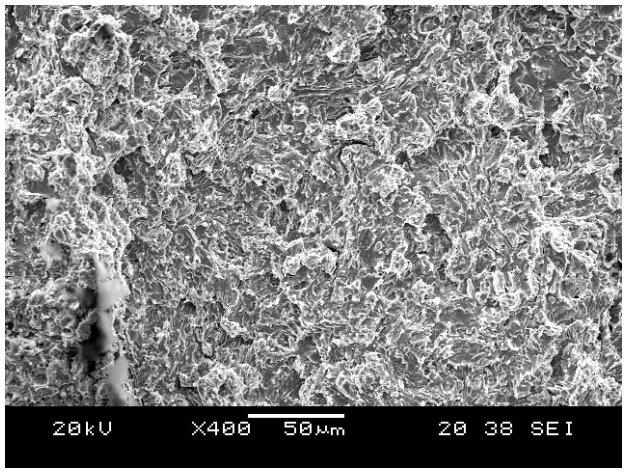


**Figure 4:** Fracture surface of brazed joint at X 400 magnification
**Slika 4:** Lomna ploskev lotanega vzorca pri 400-kratni povečavi

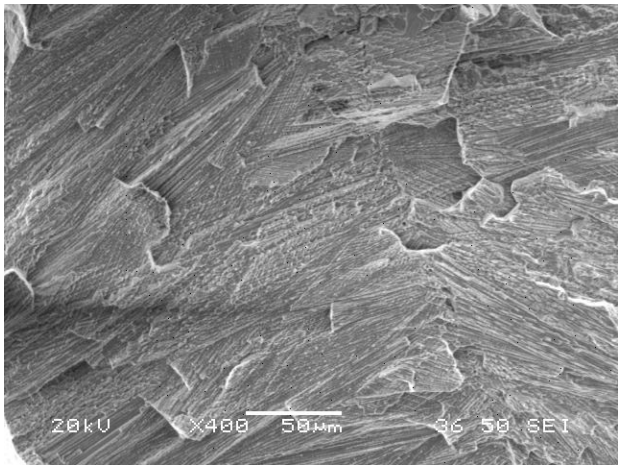


**Figure 5:** Fracture surface of laser welded joint at X 400 magnification
**Slika 5:** Lomna ploskev lasersko varjenega vzorca pri 400-kratni povečavi

and the central area remained unwelded. Even after X-shaped laser welding, the central area remained partly unwelded, but the joined effective cross-section was larger than in the I-shaped laser-welded specimens. However, there was no significant difference in the tensile strength of the two groups. In the laser welded joints the fracture surfaces were coarse grained and brittle (**Figure 5**).

## 4 DISCUSSION

The average tensile strength of the laser-welded joints was significantly lower than that of the brazed joints, mainly due to the smaller cross-section of the welded joints and partly due to the relatively strong brazed joints. For the purpose of comparing brazing with laser welding of Co-Cr alloys, most authors used a noble filler metal.[5–7] Average tensile strengths of these brazings ranged from 357 MPa to 519 MPa.[7,9] In this study, the average tensile strength of brazed specimens was 792 MPa. The average tensile strength of laser-welded Co-Cr dental alloy joints investigated thus far has ranged from 480 MPa to 751 MPa,[7,28, 29] which exceeds the average strength of laser welds in this study (404 MPa and 405 MPa).

An important reason for the relative weakness of laser-welded joints in this study is a small effective cross-section of specimens that was actually joined. This is a problem associated with low weld penetration depth.[28,29] In laser welding using the I-shaped joint design, laser pulses were not powerful enough to reach the central parts of the specimens, although peripherally the metal was overheated with a resulting porosity. Optimizing laser parameters could, to some extent, improve the quality of these welds.[29] The composition of the alloy greatly affects its weldability and in this respect, the carbon content is critical.[28] For laser welding, the manufacturer recommends an alloy with no carbon (Remanium 900). Yet, according to clinical experience, this alloy is not stiff enough for partial denture frameworks and was therefore not used in this study.

Nevertheless, laser welding of Co-Cr denture frameworks has been used with considerable success in clinical practice. A plausible explanation is that during mastication prostheses are never subjected to isolated tensile loads. In bending, most of the load is placed on the peripheral parts of the framework; one side is subjected to tension and the other one to compression, while central portions are less involved. Since the examination of fracture surfaces in this study showed that the laser welding technique was much more effective in the peripheral than in the central parts of the specimens, it is possible that the technique would prove satisfactory in most clinical situations.

The results of electrochemical measurements, which are in agreement with previously published data,[6,12,17,18] showed excellent corrosion resistance of the intact Co-Cr dental alloy. On the basis of previous qualitative observations, it was expected that laser-welded joints would exhibit better resistance to corrosion than brazed joints. This was confirmed by the results of both electrochemical methods used. With the potentiodynamic curves of the welded joints, a characteristic passive region was observed, whereas in the case of the brazed joints, measured current increased rapidly and continuously. The more noble potential of the filler additionally polarized the parent metal and consequently almost no passivation took place. Similar conclusions could be drawn from the measured impedance spectra, where all characteristic impedance values of the brazed joints were lower than those of the intact alloy and the welded joints.

However, the corrosion processes, which were investigated by EPP and EIS, occurred at the surface of the test specimen and thus were not influenced by bulk defects. Compared to brazed joints, laser-welded joints had more porosity and similar defects likely to initiate corrosion in a clinical situation. From EPP and EIS measurements it was not possible to determine weather the corrosion process was localized or generalized, which is a limitation of this study. SEM analysis revealed localized phenomena, such as pitting near the joints and pronounced corrosion in some defects on surfaces. In case of localized corrosion, and over longer periods of time, the process could become autocatalytic and more pronounced than in the study.

The laser welding process could, to some extent, be improved by increasing the weld penetration depth. Preparation of the areas to be welded, such as marking them black with a black felt-tipped pen or airborne-particle-abrading can reduce laser beam reflection and could probably improve the welding efficiency.[2] In situations where surfaces to be laser-welded can be

designed in advance, large joint surfaces might ensure sufficient strength and limited thickness might enable complete joining with minimum porosity. These questions remain to be addressed in the future.

## 5 CONCLUSION

Laser-welded Co-Cr alloy joints exhibit excellent corrosion resistance, but their tensile strength is limited due to the shallow weld penetration. Using laser welding mainly the peripheral parts of the joints can be successfully welded. Brazed joints are less resistant to corrosion but have significantly higher tensile strength.

## 6 REFERENCES


[1] Wataha JC. Alloys for prosthodontic restorations. J Prosthet Dent 87 (**2002**), 351–63

[2] Wulfes H. Precision milling and partial denture constructions. Bremen: Academia Dental; 2003. p. 259–60; 115–9; 108–13

[3] Craig RG. Dental materials: properties and manipulation. 7th ed. St Louis. Mosby; 2000. p. 228–38; 20–3

[4] Henriques GE, Consani S, Rollo JM, Andrade e Silva F. Soldering and remelting influence on fatigue strength of cobalt-chromium alloys. J Prosthet Dent. 78 (**1997**), 146–52

[5] Angelini E, Pezzoli M, Rosalbino F, Zucchi F. Influence of corrosion on brazed joints' strength. J Dent 19 (**1991**), 56–61

[6] Luthy H, Marinello CP, Reclaru L, Sharer P. Corrosion considerations in the brazing repair of cobalt based partial dentures. J Prosthet Dent 75 (**1996**), 515–24

[7] NaBadalung DP, Nicholls JI. Laser welding of a cobalt-chromium removable partial denture alloy. J Prosthet Dent 79 (**1998**), 285–90

[8] Dominici JT, Sobczak KP, Mitchell RJ. A comparison of infrared- and torch-soldering of Au-Pd and Co-Cr metal-ceramic alloys using a high-fusing solder. J Prosthodont 4 (**1995**), 101–10

[9] Wiskott HW, Macheret F, Bussy F, Besler UC. Mechanical and elemental characterization of solder joints and welds using a gold-palladium alloy. J Prosthet Dent 77 (**1997**), 607–16

[10] Dong H, Nagamatsu Y, Chen KK, Tajima K, Kakigawa H, Shi S. Corrosion behavior of dental alloys in various types of electrolyzed water. Dent Mater J 22 (**2003**), 482–93

[11] Landolt D. Introduction to surface reactions: Electrochemical basis of corrosion in Corrosion mechanics in theory and practice. Vol 17. 2nd ed. New York: Marcel Dekker Inc; 2002. p 1–19

[12] Kelly RG, Shoesmith DW, Buchheit RG. Electrochemical techniques in corrosion science and engineering. New York: Marcel Dekker Inc; 2003. p. 55–124; 125–150; 205–57

[13] McDonald MM. Corrosion of braze joints. In: Metals Handbook 9th Edition, Vol 13, Corrosion, Metals Park: ASM International, 1987. p. 876–886

[14] Shigeto N, Yanagihara T, Hamada T, Budtz-Jorgensen E. Corrosion properties of soldered joints. Part 1. Electrochemical action of dental solder and dental nickel-chromuim alloy. J Prosthet Dent 62 (**1989**), 512–515

[15] Cortada M, Giner LL, Costa S, Gil FJ, Rodriguez D, Planell JA. Galvanic corrosion behavior of titanium implants coupled to dental alloys. J Mater Sci Mater Med 11 (**2000**), 287–93

[16] Al-Ali S, Oshida Y, Andres CJ, Barco MT, Brown DT, Hovijitra S, et al. Effects of coupling methods on galvanic corrosion behavior of commercially pure titanium with dental precious alloys. Bio-med Mat Eng 15 (**2005**), 307–16

[17] Wataha JC. Biocompatibility of dental casting alloys. J Prosthet Dent 87 (**2000**), 223–34

[18] Geurtsen W. Biocompatibility of dental casting alloys. Crit Rev Oral Biol Med 13 (**2002**), 71–84

[19] Martin MD, Broughton S, Drangsholt M. Oral lichen planus and dental materials: a case-control study. Contact Dermatitis 48 (**2003**), 331–6

[20] Mansfeld F, Shih H, Greene H, Tsai CH. Analysis of EIS data for common corrosion processes. In: Electrochemical Impedance: Analysis and Interpretation, Scully JR, Silverman DC, Kendig MW, editors. Philadelphia: American Society for Testing and Materials; 1993. p. 37–53

[21] Sun D, Monaghan P, Brantley WA, Johnston WM. Electrochemical impedance spectroscopy study of high-palladium dental alloys. Part I: Behavior at open-circuit potential. J Mater Sci Mater Med 13 (**2002**), 435–42

[22] Cai Z, Vermilyea SG, Brantley WA. In vitro corrosion resistance of high-palladium dental casting alloys. Dent Mater 15 (**1999**), 202–10

[23] Mueller HJ, Hirthe RW. Electrochemical characterization and immersion corrosion of a consolidated silver dental biomaterial. Biomaterials 22 (**2001**), 2635–46

[24] Mueller HJ. In vitro tarnish and corrosion of a consolidated silver material for direct filling applications. Dent Mater 17 (**2001**), 60–70

[25] Acciari HA, Guastaldi AC, Brett CMA. Corrosion of the component phases presents in high copper dental amalgams. Application of electrochemical impedance spectroscopy and electrochemical noise analysis. Corr Sci 47 (**2005**), 547–653

[26] Duffo GS Quezada Castillo E. Development of an artificial saliva solution for studying the corrosion behavior of dental alloys. Corrosion 60 (**2004**), 594-602

[27] Jemt T, Henry P, Linden B, Naert I, Weber H, Bergstrom C. A comparison of laser-welded titanium and conventional cast frameworks supported by implants in the partially edentulous jaw: a 3-year prospective multicenter study. Int J Prosthodont 13 (**2000**), 282–8

[28] Bertrand C, Le Petitcorps Y, Albingre L, Dupuis V. The laser welding technique applied to the nonprecious dental alloys procedure and results. Br Dent J 190 (**2001**), 255–7

[29] Bertrand C, le Petitcorps Y, Albingre L, Dupuis V. Optimization of operator and physical parameters for laser welding of dental materials. Br Dent J 196 (**2004**), 413–8

[30] Fusayama T, Katayori T, Nomoto S. Corrosion of gold and amalgam placed in contact with each other. J Dent Res 42 (**1963**), 1183–97

[31] European Committee for Standardization. Standard EN 10002 – 1: Metallic materials; tensile testing; part 1: method of test. Brussels, 1996

UDK 669.14:620.18
Original scientific article/Izvirni znanstveni članek

ISSN 1580-2949
MTAEC9, 41(6)301(2007)

# DEVELOPMENT OF MICROSTRUCTURE OF STEEL FOR THERMAL POWER GENERATION

## RAZVOJ MIKROSTRUKTURE JEKEL ZA TERMIČNO GENERACIJO ENERGIJE

**Kvackaj Tibor, Kuskulic T., Fujda M., Pokorny I., Weiss M.[1], Bevilaqua T. [1]**

Technical University in Kosice, Slovakia
[1]ŽP-Podbrezová, a. s.
tibor.kvackaj@tuke.sk

*Prejem rokopisa – received: 2006-10-05; sprejem za objavo – accepted for publication: 2007-10-18*

The evolution of microstructure during the reheating and cooling of steel for thermal power generation was investigated. On the basis of the microstructure produced during cooling a CCT diagram is proposed.

Key words: steel, thermal power generation, microstructure, CCT diagram

Raziskan je bil razvoj mikrostrukture pri segrevanju in ohlajanju jekel za toplotno generacijo energije. Na podlagi mikrostrukture, ki je nastala pri ohlajanju, je bil predložen CCT-diagram.

Ključne besede: jeklo, toplotna generacija energije, mikrostrukture, CCT diagram

## 1 INTRODUCTION

Natural gas is now an important source of energy. However, especially in developing countries, lignite and anthracite will also be used for the generation of electrical energy, and power stations utilizing these energy resources for steam production will also play an important role in the future.

The minimization of the capital costs required to build new steam-power stations leads to the extensive use of ferrite-martensite steels, or martensite steels for all the main components in boilers and turbines [1].

For modern power stations the operating conditions are defined as follows:

- 540 °C/18 MPa
- 600 °C /30 MPa
- 720 °C /37.5 MPa - expected for the future

The applied materials were analyzed for their creep rupture strength under the following conditions:

- short-term creep behavior up to $t$ = 10 000 h
- long-term creep test up to $t$ = 100 000 h

In **Figure 1**[2] the chemical analysis and the creep resistance is given for some classic and newly developed steels.

The 1CrMoV steel has been used for a very long time and is considered as a classic steel. The steels with an increased content of Cr up to 9–12 % with addition of Nb and B are considered as newly developed types.

The newly developed steels can be, in comparison to classic materials, applied in operating conditions with increased steam temperatures of 30-70 °C. The steels for

| Steel | C | Cr | Mo | W | V | Nb | N | B | w/% |
|---|---|---|---|---|---|---|---|---|---|
| 1CrMoV | 0.28 | 1.0 | 0.9 | - | 0.30 | - | - | - | |
| 12CrMoV | 0.21 | 12.0 | 1.0 | - | 0.30 | - | - | - | |
| 10CrMoV | 0.12 | 10.0 | 1.5 | - | 0.20 | 0.05 | 0.05 | - | |
| 10CrMoWV | 0.12 | 10.0 | 1.0 | 1.0 | 0.20 | 0.05 | 0.05 | - | |
| 9CrMoVB | 0.18 | 9.0 | 1.5 | - | 0.25 | 0.05 | 0.02 | 0.010 | |

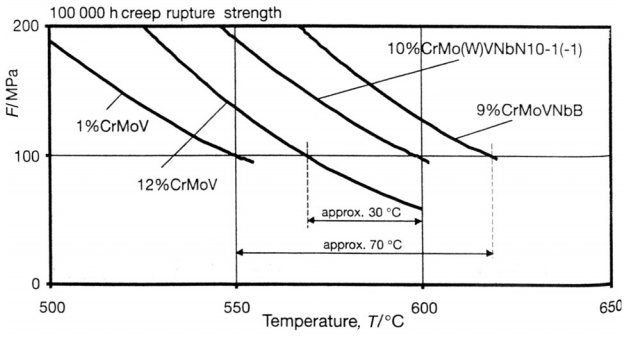


**Figure 1**[2]**:** Creep rupture strength of the new 9–10 % Cr rotor materials applied in Europe
**Slika 1:** Odpornost proti lezenju pri novih 9–10 % Cr jeklih, ki se uporabljajo v Evropi

**Table 1**[3]**:** Chemical composition and properties of two steels
**Tabela 1**[3]**:** Kemična sestava in lastnosti dveh jekel

| $w$ | C | Cr | Mo | W | Ni | V | Nb | N | $B$/ µg/g | $R_{p\,0,2}$/ MPa | $FATT_{50}$/ °C |
|---|---|---|---|---|---|---|---|---|---|---|---|
| GX12CrMoVNbN9 1 | 0,12 | 9 | 1,0 | – | 0,4 | 0,2 | 0,06 | 0,05 | 80 | 633 | +46 |
| GX12CrMoWVNbN 10 1 1 | 0,12 | 10 | 1,0 | 1,0 | 0,7 | 0,2 | 0,06 | 0,05 | 10 | 730 | +40 |

steam-turbine rotors can be divided into three groups according to their chemical composition:

- 10 % Cr + Mo
- 10 % Cr + W+ Mo
- 9 % Cr + Mo + B

These steels are used for the manufacturing of rotors with diameters up to 1200 mm. The basic properties for two steel grades are given in **Table 1** [3].

Besides the steels based on CrMoV or CrMoVW, steels based on CrMoNiV or CrMoNiVW have also been developed. The research work is currently oriented to improve steel technology with the aim to decrease the content of unwanted elements in the steel and to master the forging technology and heat-treating processes of these high-purity steels. The aim is to obtain good chemical and structural homogenity of the material, as well as forgings with minimum of defects [4].

The properties of steel depend on the steam characteristics, since the turbines can operate in conditions of:

- HP – high pressure
- IP – intermediate pressure
- LP – low pressure

The specifications of the material should be defined by the following characteristics:

1. Static strength – failure strength
2. Creep rupture strength, high-temperature strength
3. Toughness – fracture toughness
4. Fatigue properties – low-cycle fatigue
   – high-cycle fatigue
5. Crack growth rate – static-creep (CG)
   – alternative – fatigue
6. Corrosion resistance – local corrosion
   – corrosion under pressure
   – corrosion fatigue
7. Erosion resistance

## 2 MATERIAL AND EXPERIMENTS

For the experiments the CrNiMoV steel, which is the equivalent to STN 41 6537, with the chemical composition in **Table 2**, was used.

The experiments were aimed at:

– the evaluation of the influence of temperature and time on the austenite grain size.
– the influence of cooling rate on the formation of the microstructure and the ARA diagram.

The experimental methods were:

– light microscopy
– differential dilatometry

## 3 RESULTS AND DISCUSSION

The diagrams showing the influence of reheating temperature and reheating time on the austenite grain size change are in **Figure 2** and **Figure 3**. From the dependencies in these two figures it was concluded that:

– the holding time at 1000 °C does not influence the austenite grain size. Thus it is possible to classify this temperature as "low-sensitive" to austenite grain size change.
– the reheating temperature of 1050 °C had a great influence on the austenite grain size, while, for holding times of 15 min and 30 min the difference in the austenite grain size is on average 8 μm, but for holding times of 45 min and 60 min this difference increases on average to 45,5 μm. It is possible to classify this temperature as sensitive to austenite grain size change.
– for reheating temperatures of (1100, 1150, 1200) °C, there is a slow increase in the austenite grain size for all the reheating times. It is possible to classify this

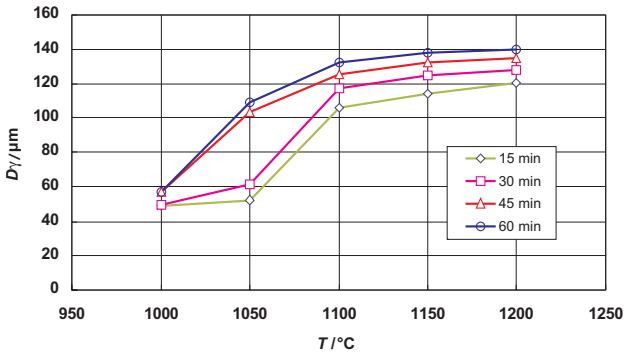


**Figure 2:** Dependence of AGS on reheating time
**Slika 2:** Odvisnost velikosti AGS avstenitnih zrn od temperature segrevanja

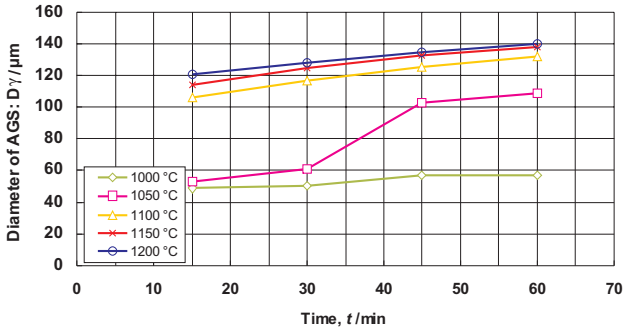


**Figure 3:** Dependence of AGS on reheating time
**Slika 3:** Odvisnost AGS od trajanja segrevanja

**Table 2:** Chemical analysis of the experimental steel
**Tabela 2:** Kemična sestava jekla za raziskavo

| C | Mn | Si | P | S | Cr | Ni | Cu | Mo | V | Al | As | Sn | Sb | Ca | H | N | O |
|---|---|---|---|---|---|---|---|---|---|---|---|---|---|---|---|---|---|
| *w*/% | | | | | | | | | | | *w*/(μg/g) | | | | | | |
| 0.29 | 0.04 | <0.01 | 0.003 | 0.003 | 1.57 | 2.84 | 0.010 | 0.39 | 0.11 | 0.004 | 11 | 8 | <5 | 20 | 0.5 | 44 | 25 |

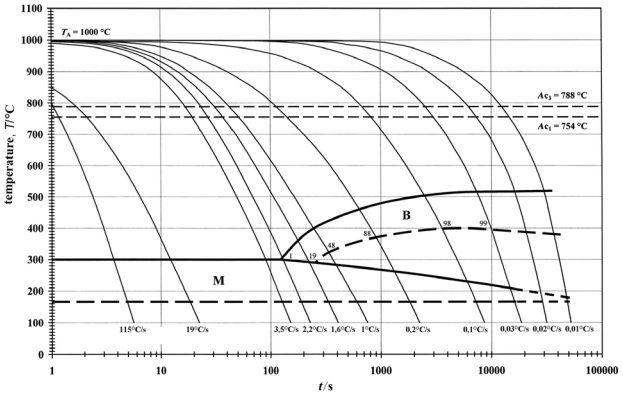


**Figure 4:** CCT diagram
**Slika 4:** CCT diagram

temperature interval as low-sensitive to austenite grain size change.

At the reheating temperature of 1050 °C a faster growth of austenite grain size is observed by increasing the reheating time. From 30 min to 45 min there is a loss of the hindering effect of carbide and nitride particles on the migration of austenite grain boundaries.

The solubility of the VC and VN precipitates for given contents of vanadium and carbon is calculated from Equations (1) and (2):

$$\lg (w(\mathrm{V})^{4/3} \cdot w(\mathrm{C})) = 7{,}06 - 10\,800/T \qquad (1)$$

$$\lg (w(\mathrm{V}) \cdot w(\mathrm{N})) = 3{,}02 - 7\,840/T \qquad (2)$$

The solubility is reached at 940 °C for vanadium carbide and 970 °C for vanadium nitride.

It is clear that the precipitates of vanadium carbide and nitride do not hinder the growth of austenite grains during the reheating time at 1050 °C.

The influence of cooling rate on the formation of the final microstructures can be evaluated by considering the dilatometry curves, the hardness and the microstructures after different cooling rates from a constant reheating temperature. In this way the transformation CCT diagram can be obtained **Figure 4**.

The obtained diagram shows that in the examined steel a real-time ferritic transformation of austenite does not occur and that only the formation of martensite, martensite + bainite, or bainite takes place. The investigated steel is thus a high-through-hardening steel.

## 4 CONCLUSION

From the results of the experimental work on a CrNiMoV steel it is possible to draw the following conclusions:

– for the reheating temperature $T$ = 1000 °C, the effect of reheating time is negligible and the austenite grain size remains in the interval $\delta$ = 49–57 μm. This reheating temperature ensures the fine-grained austenitic structure, which is a good starting point for achieving a fine-grained secondary structure, also in cases without plastic deformation after reheating. This is also valid for 15 min or 30 min reheating at 1050 °C when the diameter $\delta$ = 52–61 μm is obtained.
– for the reheating temperature of 1050 °C and reheating time $t$ = 45 min and 60 min an increased sensitivity to austenite grain growth is found and the size of $\delta$ = 103–109 μm is obtained. Similar characteristics are also observed for the reheating conditions $T$ = 1100–1200 °C and $t$ = 15 min or 60 min when the size of $\delta$ = 106–140 μm is obtained. If the reheating conditions are chosen considering the mentioned intervals, a controlled forging and controlled cooling regime will be required for achieving a fine-grained secondary structure.
– the CCT diagram obtained shows that the investigated steel is self-hardening.

## Acknowledgement

This research was carried out within the scope of the EUREKA E!3192 ENSTEEL project.

## 5 REFERENCES

[1] Kvackaj, T.: Entry opponency of project EUREKA E!3192 ENSTEEL

[2] Sheng, S., Kern, T. U.: High strenght cast and forged materials for application in steam turbine design, In: PARSONS 2000 Advanced materials for 21st century turbines and power plant, 3–7 July 2000, Cambridge

[3] Mayer, K. H., Kern, T. U., Staubli, M., Tolksdorf, E.: Long-term investigation of specimens of 24 production components manufactured from advanced martensitic 10 % Cr steels for 600 °C steam turbines, In: PARSONS 2000 Advanced materials for 21st century turbines and power plant, 3–7 July 2000, Cambridge

[4] Scarlin, R. B.: Improved materials for high efficiency steam turbines, In: Advances in turbine materials, design and manufacturing, 4-6 November 1997, Newcastle upon Tyne

# MLADI RAZISKOVALCI – NAGRAJENCI 15. KONFERENCE O MATERIALIH IN TEHNOLOGIJAH, PORTOROŽ, 8.–10. OKTOBER, 2007

## YOUNG SCIENTISTS AWARDS, 15th CONFERENCE ON MATERIALS AND TECHNOLOGY, PORTOROŽ, 8–10 OCTOBER, 2007


## JURIJ GONTAREV

VALJI, d. o. o., Štore, Železarska cesta 3, 3220 Štore


Po zaključku dodiplomskega študija materialov na Fakulteti NTF Univerze v Ljubljani sem se zaposlil v livarni valjev Valji, d. o. o., Štore. Kot mladi raziskovalec sem vključen v bilateralne projekte med Valji, d. o. o., in IMT v Ljubljani kot tudi v projekte, ki jih sofinancira MG in MVZT.

### IDENTIFIKACIJA KARBIDOV V ZLITINI PLAŠČA VALJA ZA TOPLO VALJANJE JEKLENE PLOČEVINE


Jurij Gontarev[1], Mirko Doberšek[2]

[1]VALJI, d. o. o., Štore, Železarska cesta 3, 3220 Štore

[2]Inštitut za kovinske materiale in tehnologije, Lepi pot 11, 1000 Ljubljana


Proizvodnji program livarne je ulivanje in toplotna obdelava različnih vrst litoželeznih valjev. Livarna v Štorah ima 100-letno tradicijo. Izdeluje valje za toplo valjanje jekla (dolgi in ploščati program), valje za začetna ogrodja toplih valjarn v barvni metalurgiji (aluminij, baker, cink), votle valje za papirno in gumarsko industrijo, valje za mineraloško industrijo. Izdeluje enoslojne valje s klasično gravitacijsko tehnologijo ter večslojne valje s tehnologijo centrifugalnega litja. V zadnjem času je poudarek na razvoju srednje in močno legiranih litin z indefinitno izločenim grafitom. Za delovne plasti teh valjev se uporabljajo litine z nadevtektično sestavo od 0,8 % do 2,3 % C. Litine so legirane s karbidotvorci (Cr, W, Mo, V), zato se v njihovih mikrostrukturah pojavlja vrsta različni enostavnih in kompleksnih karbidov.

Ker sem v letu 2006 kot MR na konferenci o materialih in tehnologijah v Portorožu predstavil centrifugalno litje valjev, sem letos poročal o identifikaciji karbidov v mikrostrukturah centrifugalno lite litine z masno vsebnostjo ogljika med 0,8 % in 1,0 %.

V livarni Štore izdelujemo večslojne centrifugalno lite valje z oznako kvalitete S-HSS. Delovna površina (plašč) valjev je izdelana iz srednje legirane nadevtektične jeklene litine. V legiranih jeklenih litinah se pojavi vrsta karbidov tipa: $M_3C$, $M_{23}C_6$, $M_7C_3$, $M_6C$, $M_2C$ in MC, ki so po navadi še kompleksne sestave. V laboratorijsko izdelanih zlitinah in "in vivo" plašča valja smo identificirali karbide. Zaradi enostavnejše identifikacije karbidov v mikrostrukturah smo izvedli jedkalne študije z različnimi jedkali (Picral, Muracami in Groesbeck). V strjevalnih mikrostrukturah teh zlitin je prostorninski delež do 10 % vezanega evtektika s karbidi tipa $M_7C_3$ in $M_6C$. S selektivnim jedkanjem in mikrokemijsko analizo s SEM, EDS in WDS smo določili karbide, ki se tudi morfološko razlikujejo.

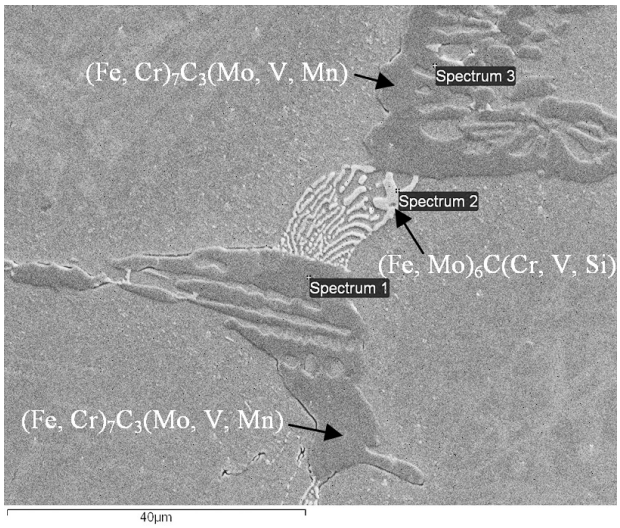


**Slika 1:** Dvojni vezani evtektik (SEI pos.)

V litih mikrostrukturah zlitine S-HSS so močno nehomogena primarna kristalna zrna avstenita, ki se pri danih pogojih ohlajanja transformirajo v martenzit. V meddendritnih prostorih sta kristalizirala dva tipa evtektikov: $\{\gamma + M_7C_3\}$ in $\{\gamma + M_6C\}$ (slika 1).

Z metodo SEM-EDS smo z analizo sekundarnih elektronov potrdili, da sta v mikrostrukturi dva tipa evtektikov z različnima karbidoma. Opaženi drobni karbidi v matrici so kromovi z raztopljenim vanadijem in molibdenom podobne vsebnosti kot v karbidih evtektičnega zloga. Menimo, da je prostorninski delež evtektika, bogatega s karbidom $(Fe_3Mo_3)C$, cca 15 % vsega evtektika v mikrostrukturi.

Ugotovili smo, da se silicij delno topi v karbidih, bogatih z molibdenom, medtem ko ga v kromovih karbidih ni. Mangan se delno topi v kromovih karbidih, medtem ko ga v karbidih, bogatih z molibdenom, nismo ugotovili. Po mejah kristalnih zrn avstenita smo našli drobna zrna kromovih karbidov tipa $M_7C_3$ in $M_{23}C_6$, ki so primarnega in sekundarnega izvora. Opazili smo, da so karbidi tipa $M_6C$ bolj kompaktno vezani z matrico, medtem ko smo na mejah $M_7C_3/\gamma$ opazili razpoke.

Zanimivo je, da smo v mikrostrukturah ugotvili vanadijeve karbide $V_4C_3$ kljub nizki vsebnosti vanadija v zlitini. Ti karbidi so naloženi v evtektičnih območjih mikrostrukture, kar nakazuje njihovo strjevanje daleč pod temperaturo njihovega tališča, o čemer poročajo tudi nekateri tuji avtorji.

Z jedkalno študijo smo ugotovili, da lahko na enostaven način ločimo nekatere vrste karbidov, kar je pomembno za karakterizacijo mikrostrukture v neposredni proizvodnji (hitro in poceni), medtem ko so zahtevnejše mikrokemijske analize s SEM-EDS, -WDS potrdile prisotnost teh vrst karbidov in identificirale dvojni vezani evtektik.

## CARBIDE IDENTIFICATION IN ALLOY FOR ROLLS MADE FOR HOT STRIP MILL WORK ROLL

Jurij Gontarev[1], Mirko Doberšek[2]
[1]VALJI, d. o. o., Štore, Železarska cesta 3, 3220 Štore
[2]Institute of Metals and Technology, Lepi pot 11, 1000 Ljubljana

In foundry Štore we produce centrifugally casted multilayer rolls. Working layer (coat) of rolls is made from medium-alloyed hypereutectoid steel casting.

We identified present carbides in laboratory made alloys. Solidified microstructures contain about 10 vol.% of bonded eutectic with carbides type $M_7C_3$ and $M_6C$. With selective etching and microchemical analysis on SEM, EDS and WDS we determined present carbides that differentiate morphologically.

Kristina Žagar
Naslov: Mlinše 32, 1411 Izlake
Rojena 15. 8. 1981 v Trbovljah

Moje raziskovalno delo se navezuje na sintezo perovskitnih nanopalčk z metodo elektroforezne depozicije (EPD) solov v pore polikarbonatnih membran. Po opravljeni depoziciji je treba vzorec kalcinirati in odstraniti nosilec (polikarbonatno membrano). Za uspešno sintezo nanopalčk je treba pripraviti stabilne sole in optimizirati pogoje elektrodepozicije. Za karakterizacijo nanopalčk uporabljamo rentgensko difrakcijo (XRD), termični analizi (DTA, TGA), vrstični in presevni elektronski mikroskop (SEM in TEM).

## SINTEZA IN KARAKTERIZACIJA PEROVSKITNIH NANOPALČK

Žagar Kristina, Šturm S., Čeh Miran
Institut "Jožef Stefan", Jamova 39, 1000 Ljubljana

Z elektroforetsko depozicijo sol-gela v nano dimenzijske pore polikarbonatne membrane smo sintizirali perovskitne nanopalčke ($BaTiO_3$, $SrTiO_3$ in $CaTiO_3$). Rast nanopalčk je potekala na delovni elektrodi iz aluminija, na katero je bila pritrjena polikarbonatna membrana. Kot protielektrodo smo uporabljali mrežasto platinasto elektrodo. Kot nosilec za nanos depozita med elektroforetsko depozicijo smo uporabljali polikarbonatne membrane (PC) z debelino od 10 μm do 25 μm in s premerom por 200 nm. Elektroforetsko depozicijo smo izvajali 30 min pri različnih napetostih, in sicer pri 2 V, 5 V in 30 V. Po depoziciji je sledila kalcinacija vzorcev pri visokih temperaturah. Med toplotno obdelavo je PC-membrana zgorela, vzorec pa je kalciniral in se zgostil. Vzorce smo nato karakterizirali z naslednjimi metodami: z rentgensko praškovno difrakcijo (XRD), diferenčno termično analizo (DTA), vrstično (SEM) in s presevno (TEM) elektronsko mikroskopijo. Z rentgensko praškovno difrakcijsko analizo smo potrdili kristaliničnost perovskitov. SEM-preiskave so potrdile, da imajo perovskitne nanopalčke, ki rastejo v porah PC-membran enak premer po celotni dolžini. Ravno tako smo opazili nastanek plasti perovskita na površini membran, ki je nastal pod vplivom višje delovne napetosti. S TEM smo opazovali strukturo in premer nanopalčk, ki je bil med 50 nm in 180 nm (**slika 1**). **Slika 2** prikazuje povečano regijo nanopalčke, ki je polikristalinična z velikostjo zrn med 25 nm in 50 nm. Primerjava med eksperimentalnim in izračunanim difrakcijskim vzorcem je pokazala, da so zrna kubičnega $BaTiO_3$.

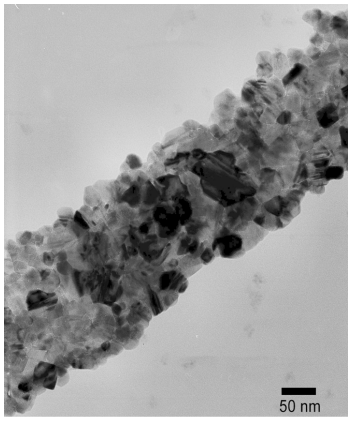


**Slika 2:** TEM-slika polikristalinične $BaTiO_3$-nanopalče z odgovarjajočim elektronskim difrakcijskim vzorcem

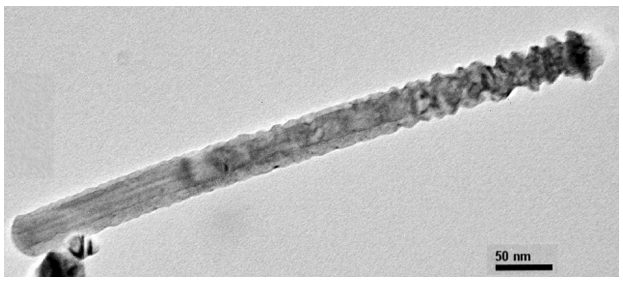


**Slika 1:** TEM slika $BaTiO_3$-nanopalčke

## SYNTHESIS AND CHARACTERIZATION OF PEROVSKITE NANORODS

Žagar Kristina, Šturm S., Čeh Miran
Jožef Stefan Institut, Jamova 39, 1000 Ljubljana

In our work we present the synthesis of perovskite nanorods ($BaTiO_3$, $SrTiO_3$ and $CaTiO_3$) by sol-gel electrophoretic deposition into template membranes. For that we used several processing methods: sol-gel processing, electrophoretic deposition and template-based growth. The growth of the nanorods occurred at a working electrode of aluminum, on which we attached a polycarbonate membrane. Pt mesh was used as the counter electrode. The track-etched hydrophilic polycarbonate (PC) membranes were used as template membranes, with pore diameters of 200 nm and a thickness of 10 μm. For the electrophoretic growth the potentials of 2 V, 5 V and 30 V were applied between the electrodes, and this was maintained for 30 min. After the deposition, the samples were annealed at elevated temperatures. This heating procedure was done in order to burn off the polycarbonate membrane and to make the nanorods dense and crystalline. The samples were then characterized by X-ray diffraction (XRD), differential thermal analysis (DTA), scanning (SEM) and transmission (TEM) electron microscopy. Crystalline perovskite phases were confirmed by XRD analysis. By using SEM we found that the perovskite nanorods grown in a PC membrane have a uniform diameter throughout their entire length. We also observed that higher potential leads to a layered formation of perovskite on the membrane surface after the pores are filled. By using TEM and electron diffraction analysis, we found that these nanorods are dense and polycrystalline, with the grain size ranging between 25 nm up to 50 nm. The size of nanorods is approximately 10 μm with a diameter of an individual nanorod in the range of 100 nm to 180 nm.

Blaž Brulc

## SINTEZA POLI(ß-BENZIL L-ASPARTATA) IN NJEGOVIH KOPOLIMEROV Z L,L-LAKTIDOM

Blaž Brulc, Maja Gričar, Ida Poljanšek, Ema Žagar, Majda Žigon
Kemijski inštitut, Hajdrihova 19, SI-1001 Ljubljana, Slovenija

**Biorazgradljive polimere** definiramo kot take, ki se razgrajujejo v naravnem okolju oziroma ki jih katabolizirajo mikroorganizmi (bakterije, glive...) ali pa se encimsko razgradijo *in vivo*. Če so njihovi razgradni produkti okolju neškodljivi (v idealnem primeru ogljikov dioksid in voda) ali se celo koristno izrabijo v svojem okolju (npr. mlečna kislina, aminokisline...), pa govorimo o **biozdružljivih polimerih**.

Omenjeni polimeri se v zadnjih 25 letih vse bolj uporabljajo kot **nosilci za nadzorovano sproščanje zdravilnih učinkovin.** To področje je eno od najhitreje razvijajočih se področij biokemijske znanosti. Sistemi za kontrolirano sproščanje zdravilnih učinkovin imajo številne prednosti pred konvencionalnimi sistemi doziranja zdravilnih učinkovin, kot so na primer: **izboljšana učinkovitost, zmanjšana toksičnost, zdravljenje, prijetnejše za pacienta** (manjše število administracij zdravila, manj izraziti stranski učinki).

V sintezi poliaminokislin so se kot primerni reagenti v preteklosti izkazali t. i. *N*-karboksianhidridi aminokislin (4-substituirani oksadolidin-2,5-dioni).

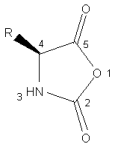

Najpogosteje uporabljeni iniciatorji polimerizacije *N*-karboksianhidridov so primarni in terciarni amini ter alkoksidi. Mehanizem iniciacije je močno odvisen od

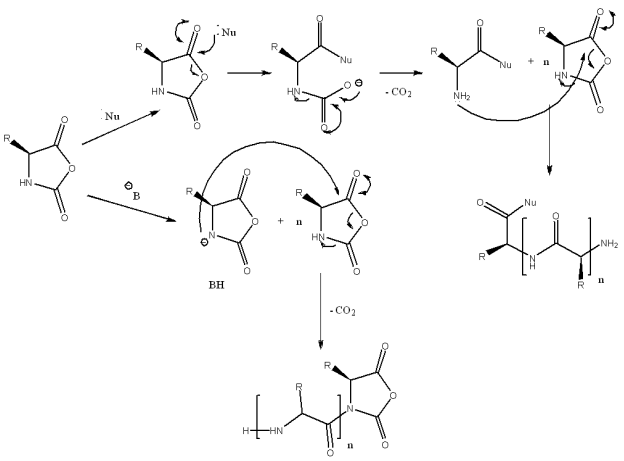

narave uporabljenega iniciatorja. Elektrofilni mesti **2** in **5** sta po eni strani občutljivi za napad nukleofilnih iniciatorjev (primarni amini, alkoholi), šibka kislost laktamskega protona na mestu **3** pa je razlog, da poteka iniciacija z bolj bazičnimi in nenukleofilnimi iniciatorji v smeri mehanizma "aktiviranega monomera".

Sintezo benzilno zaščitenega *N*-karboksianhidrida L-asparaginske kisline smo izvedli z reakcijo ß–benzil L-aspartata s trifosgenom kot acilirnim reagentom. *N*-Karboksianhidridi so zelo občutljivi predvsem za vlago pa tudi na prisotne nečistoče, zato jih je treba čistiti (večkratna kristalizacija), obvezna pa je tudi hramba v argonovi atmosferi pri nizki temperaturi.

Čeprav je bil že prekristaliziran produkt reakcije elementno čist, je bila za nadaljnje sintezne korake potrebna dodatna prekristalizacija, saj lahko v naslednjem koraku z neočiščenim *N*-karboksianhidridom sintetiziramo le nižjemolekularne homopolimere.

Iz večkrat prekristaliziranega *N*-karboksianhidrida L-asparaginske kisline smo pri sobni ali nekoliko zvišani temperaturi v *N*,*N*-dimetilformamidu z dobrim izkoristkom (> 95 %) sintetizirali poli(ß-benzil L-aspartate) s povprečjem molskih mas redov velikosti $10^3$–$10^4$ g mol$^{-1}$. Pripravili smo produkte z zelo ozko porazdelitvijo molskih mas (PDI = 1,00–1,09) Povprečja molskih mas polimerov so bila določena z metodo izključitvene kromatografije z detektorjem na sipanje svetlobe. Molska masa produktov ni bila odvisna od temperature, pri kateri smo izvajali reakcije (25–40 °C), močno pa je odvisna od uporabljenega iniciatorja polimerizacije (trietilamin *vs.* *n*-pentilamin) ter čistosti izhodnega monomera. Tako smo z uporabo trietilamina ob enakih reakcijskih pogojih iz trikrat prekristaliziranega monomera v primerjavi z le enkrat kristaliziranim pripravili poli(ß-benzil L-aspartat) s trikrat večjo molsko maso (9,2 × $10^3$ g mol$^{-1}$) Reakcija z *n*-pentilaminom prav tako poteče do praktično monodisperznih polimerov (PDI = 1,00), a so povprečja molskih mas za čas reakcije 24 h (nepopolna konverzija) nekoliko nižja.

Da bi se izognili potencialnim stranskim reakcijam in občutljivosti monomera za vlago, smo vse reakcije izvajali v suhi argonovi atmosferi.

Reakcijo kopolimerizacije z laktidom smo najprej izvajali v masi pri temperaturi 140 °C. A pri tej temperaturi prihaja do hidrolize benzilnih estrskih skupin na asparaginskih enotah. Iz tako sproščenih karboksilnih skupin na glavni verigi pa lahko rastejo stranske polilaktidne verige. Rezultat so kopolimeri s pripajanjem, katerih strukture ni mogoče nadzorovati, saj pri teh reakcijskih pogojih obseg hidrolize estrskih skupin ni kontroliran. Zato smo nadaljnje reakcije izvajali v različnih topilih (THF, dioksan, *N*,*N*-dimetilformamid) pri temperaturi 50 °C, saj smo z NMR spektroskopijo ugotovili, da so v teh topilih pri omenjenih temperaturah benzilne estrske skupine kvantitativno obstojne vsaj 24 h.

V prejšnji stopnji pripravljeni poli(ß-benzil L-aspartat) nam v tem koraku hkrati rabi kot reagent in skupaj s predestiliranim kositrovim(II) bis(2-etilheksanoatom) kot koiniciator polimerizacije z odpiranjem obroča laktida.

Tak način sinteze omogoča pripravo nizkopolidisperznih blokkopolimerov asparaginske kisline in laktida, v prihodnje pa bo potrebna optimizacija reakcijskih parametrov sinteze.

## SYNTHESIS OF POLY(ß-BENZYL L-ASPARTATE) AND ITS COPOLYMERS WITH L,L-LACTIDE

Blaž Brulc, Maja Gričar, Ida Poljanšek, Ema Žagar, Majda Žigon
National Institute of Chemistry, Hajdrihova 19, SI-1001 Ljubljana, Slovenia

In our work poly(ß-benzyl L-aspartate)s and their block copolymers with L,L-lactide with varying molar mass averages and low polydispersity indices (PDI = 1.00–1.09) were prepared. NMR and FT-IR spectroscopy was used to elucidate the products' chemical composition, and size-exclusion chromatography coupled to multi-angle laser photometer (SEC-MALLS) was used for the determination of the absolute molar mass averages of the products.

Polymerizations of aspartic acid *N*-carboxyanhydrides were carried out in dry *N*,*N*-dimethylformamide at room temperature and at slightly elevated temperatures (up to 40 °C) in a dry argon atmosphere using triethylamine or *n*-pentylamine as the initiatior. The polymerization mechanism is strongly dependent on the nature of the initiator used, both mechanistic pathways giving practically monodisperse products. Homopolymers synthesized in the described way were further used as macrocoinitiators in the ring-opening polymerization of L,L-lactide using stannous(II) octoate as the catalyst.

NMR spectra and SEC-MALLS chromatograms showed that copolymers synthesized in this manner were linear, but those prepared at higher temperatures exhibited some degree of branching due to partial hydrolysis of pendant benzylic ester groups. Deprotected carboxylic groups act as reactive sites for either grafted polyaspartate or lactide side chains.

Nataša Drnovšek

## DVOPLASTNA PREVLEKA NA ZLITINI Ti6Al4VZA BIOMEDICINSKO UPORABO

Nataša Drnovšek[1], Nina Daneu[1], Saša Novak[1], Katja Rade[1], Janez Kovač[2]
[1]Odsek za nanostrukturne materiale, IJS, Ljubljana, Slovenija
[2]Odsek za tehnologijo površin in optoelektroniko, IJS, Ljubljana, Slovenija

Titanove zlitine se zaradi svojih dobrih lastnosti, kot so relativno nizek elastični modul, visoka trdnost, korozijska odpornost in biokompatibilnost, široko uporabljajo za kostne vsadke. Kjub dobrim lastnostim pa klinični rezultati kažejo, da se določen delež vsadkov razmaje, kar je delno pripisano nezadovoljivi pritrditvi vsadka. Zato sta za trajne vsadke potrebni dobra pritrditev in stabilnost, torej dobro vraščanje kostnega tkiva v vsadek, kar lahko dosežemo z modificiranjem površine zlitine.

Oseointegracijo vsadka in tkiva je možno izboljšati z bioaktivnimi prevlekami, ki omogočijo neposredno povezavo vsadka s kostjo. Takšni bioaktivni prevleki sta hidroksiapatit in biosteklo. Pri naših raziskavah smo uporabili bioaktivno steklo. Na vsadek smo najprej nanesli tanko prevleko iz $TiO_2$, ki izboljša adhezijo bioaktivne prevleke na podlago iz Ti-zlitine, prav tako izboljša biokompatibilnost, korozijsko odpornost ter prepreči difuzijo kovinskih atomov v telo.

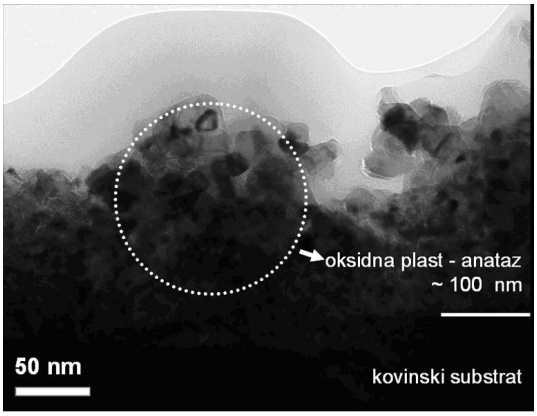


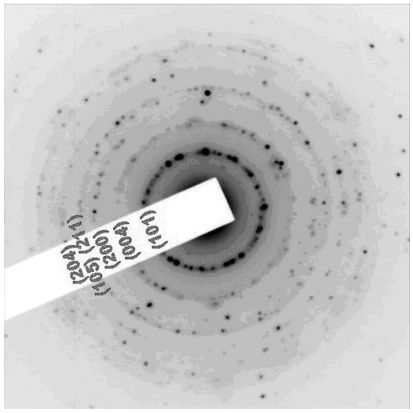


**Slika 1:** a) TEM-posnetek $TiO_2$-plasti na Ti6Al4V in b) elektronska difrakcija te plasti, ki potrjuje, da je oksid anataz

V tem delu smo plast $TiO_2$ na površini Ti6Al4V pripravili s hidrotermalno obdelavo. Da bi dobili približno 100 nm debelo oksidno plast $TiO_2$-strukture anataz, ki je bolj bioaktiven od rutila, smo spreminjali pogoje obdelave, kot so temperatura, tlak, čas in pH suspenzije. Preučili smo tudi, kako dodatna toplotna obdelava, ki je potrebna za sintranje zgornje bioaktivne prevleke, vpliva na že s hidrotermalno obdelavo nastalo plast $TiO_2$. Z analizami XPS, AES, SEM in TEM smo preverili debelino, strukturo in proces nastanka oksidne plasti. 100 nm debelo oksidno plast iz $TiO_2$ anataza (**slika 1**) smo dobili pri dovolj visokem pH suspenzije ($\approx$8) z dodatkom ionov $Ti^{4+}$ po 24 h hidrotermalne obdelave pri 150 °C. Dodatna toplotna obdelava je povečala debelino oksidne plasti, vendar so visoke temperature (750 °C) povzročile, da je oksid začel odpadati od podlage.

Na $TiO_2$-plast smo nato z elektroforetsko depozicijo nanesli še prevleko iz bioaktivnega stekla in že po eni minuti smo dobili 150 μm debelo plast, ki se je po

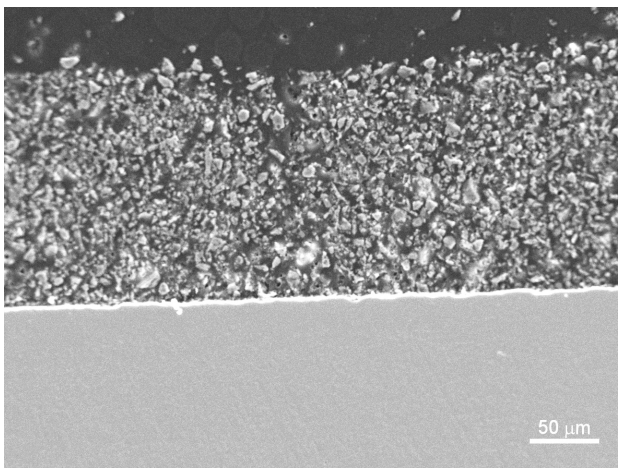


**Slika 2:** Prevleka iz biostekla na zlitini Ti6Al4V po sintranju

sintranju dobro držala podlage iz Ti-zlitine in ni imela razpok (**slika 2**).

## A DOUBLE-LAYER COATING ON A Ti6Al4V ALLOY FOR BIOMEDICAL APPLICATIONS

Nataša Drnovšek[1], Nina Daneu[1], Saša Novak[1], Katja Rade[1], Janez Kovač[2]
[1]Jožef Stefan Institute, Department for Nanostructured Materials, Ljubljana, Slovenia
[2]Jožef Stefan Institute, Department of thin films and surfaces, Ljubljana, Slovenija

Titanium alloys are widely used as implant materials because of their good properties, such as a relatively low elastic modulus, a high specific strength, good corrosion resistance and superior biocompatibility. Clinical results, however, reveal a certain percentage of loosening of hip prostheses, partly ascribed to insufficient fixation. Hence, in order to improve the fixation and stability of an implant, a surface modification of the alloy is needed.

Implant-tissue osseointegration can be enhanced by bioactive coatings, such as hydroxyapatite or bioactive glass, which are able to provide direct bonding of an implant to the host bone. According to literature data, a thin $TiO_2$ layer at the surface of the Ti-alloy improves the corrosion resistance, prevents the diffusion of metal ions in the body as well as providing better adhesion of the bioactive coating to the alloy substrate.

The main goal of our studies is to improve the bone-implant bonding ability and to enhance the osseointegration of the implant by forming a functionally graded bioactive coating on the Ti-alloy substrate. In this particular work, the $TiO_2$ layer was formed on the surface of Ti6Al4V by a hydrothermal treatment of the alloy under various conditions. The thickness of the $TiO_2$ layer was further increased by thermal treatment. Then, a bioactive layer was deposited over the $TiO_2$ layer using a dip-coating method. The microstructural properties of the coating were studied using SEM, TEM and XPS analyses.

Jakob König, univ. dipl. ing. kem., rojen 23. 8. 1979 na Jesenicah.
Zaposlitev: Institut "Jožef Stefan", Odsek za raziskave sodobnih materialov
V študijskem letu 2007/08 študent 4. letnika podiplomskega študija na Mednarodni podiplomski šoli Jožefa Stefana
Področje dela: materiali, elektronska keramika

Zaradi povečane skrbi za varovanje zdravja ljudi in ohranitev okolja se je v zadnjih letih močno povečalo število raziskav alternativnih materialov. Tako se na področju feroelektričnih materialov razvijajo materiali, ki ne vsebujejo svinca ("lead-free materials"). Mednje spada tudi $Na_{0,5}Bi_{0,5}TiO_3$, katerega lastnosti so odvisne od zunanjih pogojev (npr. od zunanjega električnega polja ali od aksialne tlačne obremenitve). Ta odvisnost nam daje možnost prilagajanja lastnosti materiala ("tunable materials") in s tem odziva komponente oz. naprave. V našem delu raziskujemo vpliv aksialne tlačne obremenitve na dielektrične lastnosti materialov na osnovi $Na_{0,5}Bi_{0,5}TiO_3$.

## POVEČANJE VPLIVA AKSIALNE TLAČNE OBREMENITVE NA DIELEKTRIČNE LASTNOSTI $Na_{0,5}Bi_{0,5}TiO_3$ Z DODAJANJEM $NaTaO_3$

Jakob König, Boštjan Jančar, Danilo Suvorov
Odsek za raziskave sodobnih materialov, Institut "Jožef Stefan", Ljubljana

Študije vpliva zunanjih mehanski sil na dielektrične lastnosti $Na_{0,5}Bi_{0,5}TiO_3$ so pokazale, da se vrednost dielektrične konstante pod vplivom aksialne tlačne obremenitve znižuje. To znižanje je največje v območju maksimuma dielektrične konstante pri 320 °C, medtem ko je pri sobni temperaturi ta vpliv veliko manjši. To je posledica velikega mehanskega koercitivnega polja, ki ga lahko približno ocenimo iz električnega koercitivnega polja (73 kV/cm). Cilj našega dela je bilo povečanje vpliva tlačne obremenitve na dielektrične lastnosti $Na_{0,5}Bi_{0,5}TiO_3$ pri sobni temperaturi, kar smo dosegli z dodatkom ustreznega materiala ($NaTaO_3$).

Z dodatkom $NaTaO_3$ se vpliv tlačne obremenitve na dielektričnost poveča, saj dodatek $NaTaO_3$ pomakne dielektrični maksimum k nižjim temperaturam (slika 1) in zniža električno koercitivno polje. Vpliv aksialne tlačne obremenitve je največji pri vzorcu s 15 % $NaTaO_3$, kjer je relativna sprememba dielektričnosti 14 % (slika 2). Dielektrične lastnosti niso reverzibilne s prenehanjem tlačne obremenitve, vendar v primeru, ko vzorec segrejemo na 600 °C za 30 min, ponovno dobimo začetne dielektrične lastnosti materiala.

## INCREASING THE EFFECT OF AXIAL PRESSURE ON THE PERMITTIVITY OF $Na_{0.5}Bi_{0.5}TiO_3$ BY ADDING $NaTaO_3$

Jakob König, Boštjan Jančar, Danilo Suvorov
Advanced Materials Department, Jožef Stefan Institute, Jamova 39, Ljubljana

$Na_{0.5}Bi_{0.5}TiO_3$ is one of the most studied lead-free ferroelectric materials. Studies of the influence of

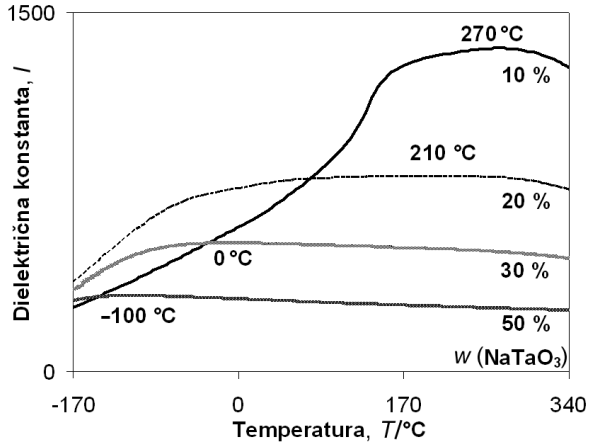


**Slika 1:** Premikanje dielektričnega maksimuma k nižjim temperaturam (10 % dodatka → 270 °C, 30 % dodatka → 0 °C).

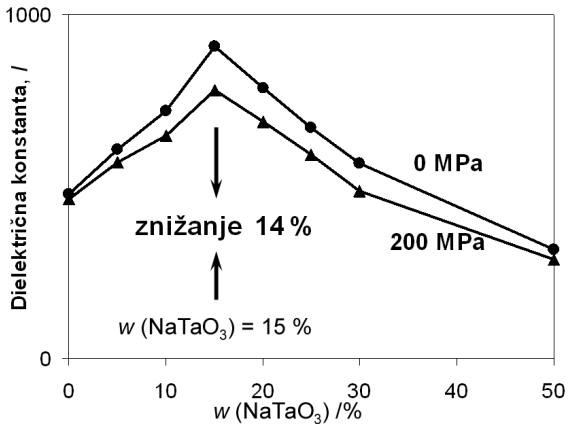


**Slika 2:** Vrednost dielektrične konstante brez obremenitve in pri tlaku 200 MPa za različne dodatke $NaTaO_3$ (merjeno pri sobni temperaturi).

mechanical forces on the electrical properties of $Na_{0.5}Bi_{0.5}TiO_3$ have shown that the dielectric constant decreases under an applied axial pressure. The reduction of the permittivity is the largest in the region of the dielectric maximum and is much smaller at room temperature, which is connected with the large mechanical coercive field, closely linked with the electrical coercive field (73 kV/cm). The pressure's influence on permittivity at room temperature can be increased by an appropriate choice of modifying material. In our study we investigated the influence of $NaTaO_3$ additions on the properties of $Na_{0.5}Bi_{0.5}TiO_3$.

The axial pressure dependence of permittivity at room temperature of the materials from the $Na_{0.5}Bi_{0.5}TiO_3$-$NaTaO_3$ solid-solution system will be presented. With the addition of $NaTaO_3$ the pressure dependence of the permittivity increases as the dielectric anomalies are shifted towards lower temperatures and the coercive field is lowered. The maximum of the pressure dependence of the permittivity was achieved in a sample with 15 % of $NaTaO_3$. The dielectric properties of the materials are time dependent, and are not fully reversible when the pressure is removed. However, after annealing the samples at 600 °C for 30 min the initial dielectric properties are recovered.

Katja Rade

## ŠTUDIJ POLIMETAKRILNE KISLINE V PRISOTNOSTI RAZLIČNIH KATIONOV V VODNEM MEDIJU

Katja Rade[1], Ksenija Kogej[2], Saša Novak[1]
[1]Institut "Jožef Stefan", Odsek za nanostrukturne materiale
[2]FKKT, katedra za fizikalno kemijo

Polimetakrilna kislina (PMA) je najpreprostejša polimerna kislina, ki je izpostavljena konformacijskemu prehodu, posledično pa je dobra modelna spojina za razumevanje npr. denaturacije molekul proteinov. Zaradi svoje sposobnosti ohranjanja kompaktne oblike pri nizkih pH-vrednostih (kot je v želodcu) in prehodu v obliko naključnega klobčiča pri višjih pH-vrednostih (debelo črevo) je uporabna tudi za ciljano dostavo zdravilnih učinkovin, ki so občutljive za kislo okolje. Za uporabo PMA v te namene je potrebno podrobno poznanje vedenja spojine. Zaenkrat še ni veliko znanega o konformacijskem prehodu spojine v prisotnosti kationov različnih valenc. S potenciometričnimi, kalorimetričnimi in fluorimetričnimi titracijami smo opazovali obnašanje PMA v prisotnosti ionov $Li^+$, $Mg^{2+}$ in $La^{3+}$ (v 0,1 M raztopinah kloridov). Čeprav je proces s termodinamskega stališča neugoden, razvijanje molekule poteče v vseh primerih, vrednost Gibbsove proste entalpije pa se z naraščajočo valenco prisotnega kationa manjša. V navzočnosti lantanovih ionov zaradi visokih nabojev verjetno nastane tudi medmolekulska asociacija.

Ataktično PMA smo preizkusili tudi kot dispergant za suspenzijo prahu aluminijevega oksida ($Al_2O_3$). Izkaže se, da je PMA ustrezen dodatek, ki zaradi svoje polimerne narave in negativno nabitih karboksilatnih ostankov deluje kot elektrosterični stabilizator, vendar se njegovo vedenje razlikuje, če titracijo izvedemo iz kislega v bazično pH-območje kot nasprotno. Pri nizkih pH-vrednostih se PMA veže na pozitivna mesta na delcih $Al_2O_3$, s tem nevtralizira neto naboj in posledično zniža vrednost zetapotenciala (ZP). Pri višjih pH-vrednostih se negativno nabita PMA veže na preostala pozitivna mesta na večinoma negativno nabitih delcih $Al_2O_3$ in s tem še poveča absolutno vrednost ZP. V območju zelo visokih pH se ZP zaradi prisotnosti ionov $Na^+$ in $Al^{3+}$, ki interagirajo z negativno nabitimi karboksilatnimi ostanki, ponovno zmanjša in je celo nižji kot v primeru suspenzije brez dodatkov. Poleg tega k zmanjšanju ZP izdatno pripomore povečana prevodnost, ki je posledica dodajanja močnih elektrolitov (HCl, NaOH); hipotezo smo preverili z dodajanjem nevtralnega elektrolita (NaCl) suspenziji $Al_2O_3$.

Z našim delom smo želeli pokazati, da bolj poglobljen princip in opazovanje vedenja dispergantov lahko prispeva dodatne informacije in s tem prispeva k uspešnejši pripravi suspenzij z želenimi lastnostmi.

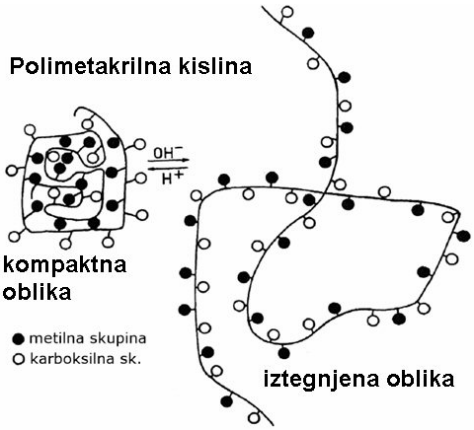


**Slika 1:** Polimetakrilna kislina v kompaktni in iztegnjeni obliki

## STUDY OF POLYMETHACRYLIC ACID IN PRESENCE OF VARIOUS CATIONS IN AQUEOUS MEDIA

Polymethacrylic acid (PMA) is an interesting compound for various reasons. It is the simplest polymeric acid that is subjected to conformational transition

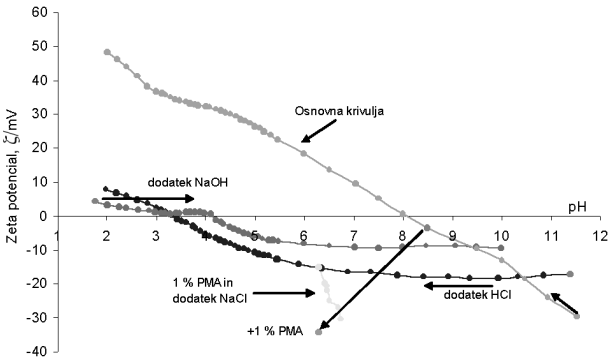


**Slika 2:** Vedenje suspenzije $Al_2O_3$ ob dodatku PMA pri titraciji v kislo ali bazično ter pri dodatku nevtralnega elektrolita

and so it appears very useful in understanding of conformational transitions of proteins. Because of its ability to stay in compact form at lower pH values (stomach) and transition into extended conformation at higher pH values (gall bladder) it can also be used in targeted drug delivery system. In order to use PMA in such ways it is very important to know its behaviour in details. There were no studies yet made about its conformational transition in the presence of cations of different valencies. We made comparison of PMA behaviour in the presence of $Li^+$, $Mg^{2+}$ and $La^{3+}$ ions (all in 0.1 M solution of chloride salt) by means of potentiometric, calorimetric and fluorimetric titration. The unfolding occurs although it is thermodynamically unfavourable. The Gibbs free energy reduces from the case without added electrolyte to solutions with added lanthanum ions. In the latter case there is also a strong indication of intermolecular association because of triple charge of lanthanum ions and high negative charge on PMA.

Atactic PMA was also used as a deflocculant in case of submicrometer sized aluminium oxide. It appears that PMA can be successfully used (because of its polymeric nature it acts as electrosteric stabilizer) but shows different behaviour if titrated from acidic to basic pH than vice versa. At lower pH PMA binds to positive sites onto alumina particles, neutralizes the net charge and therefore decreases average zeta potential (ZP). At higher pH the negatively charged PMA binds onto the positive sites on particles' surface which is mainly negatively charged and increases the absolute value of ZP. In comparison to the case with no added PMA The ZP is again decreased at very high pH values because of the presence of $Na^+$ and $Al^{3+}$ ions in the solution (these interact with negatively charged carboxylic groups).

Ines Bračko, univ. dipl. inž. kem., rojena 24. 4. 1977 v Mariboru
Zaposlena na Institutu "Jožef Stefan", Odsek za raziskave sodobnih materialov
V študijskem letu 2007/08 študentka 2. letnika doktorskega študija na Mednarodni podiplomski šoli Jožefa Stefana
Področje dela: 1D-nanostrukturni materiali

V zadnjih desetih letih je bilo veliko pozornosti namenjene raziskavam in sintezi 1D-nanostrukturnih materialov (nanocevke, nanopalčke, nanožičke). Zaradi unikatnih električnih, mehanskih, magnetnih in optičnih lastnosti, ki so posledica velikosti (majhnosti) in velikega razmerja med površino in volumnom teh nanostruktur, so ti materiali zanimivi za številne aplikacije v nanonapravah prihodnosti. Hidrotermalna sinteza je obetajoča tehnika za sintezo različnih perovskitov z 1D-nanostrukturo. Vendar pa je o reakcijskih mehanizmih, ki potekajo med takšno sintezo in so ključnega pomena za pripravo želenih produktov, malo znano. V naši študiji uporabljamo kot modelni sistem kalcijev titanat – $CaTiO_3$.

## RAZUMEVANJE NASTANKA NANOSTRUKTURNEGA PEROVSKITA $CaTiO_3$ POD HIDROTERMALNIMI POGOJI

Ines Bračko[1], Boštjan Jančar[1], Sašo Šturm[2], Danilo Suvorov[1]
[1]Odsek za raziskave sodobnih materialov, Institut "Jožef Stefan", Ljubljana, Slovenija
[2]Odsek za nanostrukturne materiale, Institut "Jožef Stefan", Ljubljana, Slovenija

V raziskavi smo za pripravo nanostrukturnega kalcijevega titanata pod hidrotermalnimi pogoji uporabili vodno raztopino kalcijevega acetata in titan(IV)izopropoksida v močno alkalnem mediju. Za karakterizacijo produktov smo uporabili različne tehnike, povezane s presevno elektronsko mikroskopijo (TEM). V študiji predstavljamo:

- nanostrukturni kalcijev titanat v obliki plastovitih monokristaliničnih dobro kristaliziranih kristalov (slika spodaj);

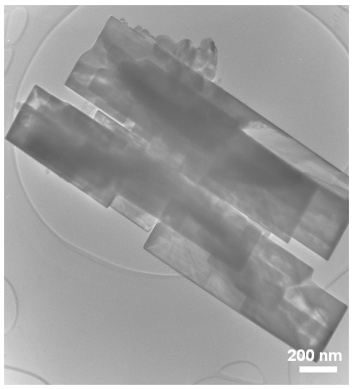


- vmesne nanostrukturne faze: nanocevke, amorfne nanodelce, tanke plastovite nanostrukture in nanožičke (slika spodaj).

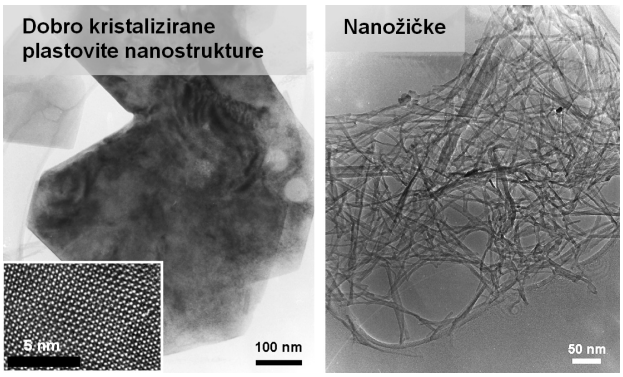


Z uporabo spektroskopije merjenja izgub energije elektronov (EELS) in z analizo finih struktur Ti-$L_{2,3}$ in ionizacijskih robov O-K (ELNES) smo ugotovili, da so nanocevke po sestavi in strukturi blizu rutilni fazi $TiO_2$. EELS analiza je nadalje pokazala, da je vgrajevanje Ca možno v drugem sklopu vmesnih faz (amorfni nanodelci, plastovite nanostrukture in nanožičke), ki se sicer razlikujejo po sestavi, morfologiji in kristaliničnosti. Menimo, da je možno te vmesne faze Ca–Ti uporabiti kot matrico za sintezo 1D-nanostrukturnega perovskita $CaTiO_3$ in da je s kontroliranjem nastanka metastabilnih faz mogoče kontrolirati morfologijo nanostrukturnega $CaTiO_3$.

# UNDERSTANDING THE FORMATION OF NANOSTRUCTURED PEROVSKITE $CaTiO_3$ UNDER HYDROTHERMAL CONDITIONS

Ines Bračko[1], Boštjan Jančar[1], Sašo Šturm[2], Danilo Suvorov[1]

[1]Advanced Materials Department, Jožef Stefan Institute, Ljubljana, Slovenija

[2]Nanostructured Materials Department, Jožef Stefan Institute, Ljubljana, Slovenija

One dimensional nanostructures such as nanotubes and nanowires are attracting great interest of research community due to their potential applications, which arise from their unique optical, mechanical and electrical properties. Over the past decade many techniques have been developed and applied for the synthesis of one dimensional nanostructured materials. Employment of hydrothermal method for preparation of nanostructured materials enables one to synthesize different nanostructured perovskites. Several successful syntheses of perovskite nanostructured materials and also suggestions to apply hydrothermal condition for preparation of nanowires of any tetragonal perovskite have been reported in the literature. However, there is still little known about the reaction mechanisms present in the hydrothermal synthesis.

In order to understand the formation mechanisms that occur during synthesis of perovskite-based nanowires via hydrothermal route we studied formation of nanostructured $CaTiO_3$ from Titanium(IV) isopropoxide and Calcium acetate aqueous solution. Low temperature reactions were performed in a Teflon autoclave in a highly alkaline environment. In our study, we present different intermediate phases taken from various reaction steps during hydrothermal synthesis, which differ in morphology, crystal structure and composition. High-Resolution Transmission Microscopy (HRTEM), Energy Dispersive X-ray Spectroscopy (EDS) and Electron Energy-Loss Spectroscopy (EELS) analyses revealed presence of at least four phases. Morphologically the most interesting phases important for formation of perovskite one dimensional nanostructures were single-crystalline sheets and nanowires. Nanowires with Ca:Ti ratio 1:3 and diameter of about 10 nm were 100 nm long. Single-crystalline sheets were 35nm thick and dimensions of about 500 nm × 500 nm with the Ca:Ti ratio approximately 0,5. Further analysis of EEL spectrum, introduction of the X-ray Powder Diffraction (XRD) and Differential Thermal Analysis (DTA) revealed that the crystal structure of single-crystalline sheets can be interpreted as a layered structure similar to either kassite – $CaTi_2O_5(OH)_2$ or cafetite – $Ca[Ti_2O_5](H_2O)$. We believe that these phases can be employed as a template precursor for synthesis of one-dimensional nanostructured $CaTiO_3$ based perovskites and that by controlling the formation of the metastable phases with high aspect ratios under hydrothermal conditions the morphology of $CaTiO_3$ nanostructures can be controlled.

# DOKTORSKA, MAGISTRSKA IN DIPLOMSKA DELA – DOCTOR'S, MASTER'S AND DIPLOMA DEGREES

## DOKTORSKA DELA – DOCTOR'S DEGREES

Na Naravoslovnotehniški fakulteti Univerze v Ljubljani je dne 9. 11.2007 pred komisijo v sestavi: izr. prof. dr. Jakob Likar kot predsednik in člani: red. prof. dr. Ladislav Kosec, red. prof. dr. Franc Vodopivec, red. prof. dr. Savo Spaić, red. prof. dr. Radomir Turk

mag. Franc Tehovnik, univ. dipl. inž. metal. zagovarjal doktorsko disertacijo z naslovom:

**Preoblikovalna sposobnost avstenitnih nerjavnih jekel**
**Workability of austenitic stainless steels**

Doktorska disertacija je bila izdelana pod mentorstvom red. prof. dr. Ladislava Kosca ter somentorstvom red. prof. dr. Franca Vodopivca.

### PREOBLIKOVALNA SPOSOBNOST AVSTENITNIH NERJAVNIH JEKEL

UDK: 669.14.018.8:621.771

POVZETEK

Delo obravnava pregled strokovne literature o strjevalni mikrostrukturi in preoblikovanju v vročem avstenitnih nerjavnih jekel, legiranih z molibdenom. Strjevanje se začne v odvisnosti od vsebnosti glavnih legirnih elementov, s primarno kristalizacijo $\delta$-ferita ali avstenita. Preoblikovalnost jekla s strjevalno mikrostrukturo v vročem je boljša pri primarni kristalizaciji $\delta$-ferita, ker ta prepreči koncentracijo nečistoč v preostali meddendritni talini. Mehanizma mehčanja med preoblikovanjem v vročem avstenitnih nerjavnih jekel sta dinamična in statična rekristalizacija.

Vpliv pogojev deformacije na procese sproščanja deformacijske energije v povezavi s kemijsko sestavo jekla in vsebnostjo $\delta$-ferita smo ugotovili na podlagi nateznih preskusov v vročem, ki pa niso omogočili ocene, kako se v začetnih valjarniških prehodih vede jeklo s strjevalno mikrostrukturo.

Avstenitna nerjavna jekla do volumenskega deleža $\delta$-ferita 12,5 % v strjevalni mikrostrukturi pri upogibni deformaciji do 28 %, niso izpostavljena nastanku razpok na površini in na robovih preskušancev. $\delta$-ferit ni zmanjšal deformabilnosti jekla v temperaturnem območju med 1050 °C in 1250 °C, ne glede, ali je bil pri nižji temperaturi razporejen v obliki zvezne ali deloma prekinjene mreže okoli zrn avstenita, in pri višji

### WORKABILITY OF AUSTENITIC STAINLESS STEELS

UDC: 669.14.018.8:621.771

ABSTRACT

In the first part of this thesis a survey of the solidification structure and hot workability of austenitic stainless steels alloyed with molybdenum is presented. The solidification occurs, depending on the content of the main alloying elements, with the primary solidification of $\delta$-ferrite or austenite. The hot workability of the as-solidified microstructure is better in the case of the primary solidification of $\delta$-ferrite, because it prevents the concentration of impurities in the residual interdendritic melt. The mechanisms of softening during the hot working of austenitic stainless steels are dynamic and static recrystalization.

In the experimental work the influence of deformation on the processes of the relaxation of deformation energy, related to the composition of the steel and the quantity of $\delta$-ferrite, was determined with hot tensile tests. These tests did not allow to evaluate the behaviour of as-cast steel during the first rolling passes.

Austenitic stainless steels with a solidification microstructure of up to 12.5 % of $\delta$-ferrite were not sensitive to hot cracking of the surfaces or edges during hot bending tests with 28 % of deformation, in the temperature range from 1050 °C to 1250 °C. At lower temperatures the $\delta$-ferrite was in the form of a continuous or discontinuous layer at the austenite grain

temperaturi, ko je ferit v ovalnih delcih, ki so ločeni s široko plastjo avstenita.

Nerjavno jeklo z masnim deležem svinca 0,0082 % s strjevalno mikrostrukturo je občutljivo za nastanek razpok po interdendritnih površinah, na katerih je večje število zrn svinca, ki jih je na meje odrinila napredujoča fronta strjevanja.

Z vročim valjanjem klinastih preizkušancev smo ugotovili temperaturo in stopnjo deformacije, pri kateri je jeklo občutljivo za nastanek valjarniških napak. Med vročim valjanjem je $\delta$-ferit enako duktilen kot avstenit. Pri temperaturah preoblikovanja 1100 °C in 1150 ° in pri okoli 30-odstotni stopnji deformacije se na robovih vzorcev pojavijo prečne razpoke, v notranjosti vzorcev pa mikrorazpoke med avstenitom in $\delta$-feritom, ki so posledica izcejanja žvepla.

Ključne besede: avstenitna nerjavna jekla, kontinuirno litje, strjevalna mikrostruktura, $\delta$-ferit, interkristalne razpoke, preoblikovalnost v vročem, vpliv nečistoč, mikrorazpoke

boundaries, while at higher temperatures the $\delta$-ferrite was in the form of rounded particles surrounded by the austenite matrix.

The as-cast stainless steel with 0.0082 wt. % of lead was sensitive to interdendritic crack formation as the number of insoluble lead particles was increased at the dendritic surface, when the particles were pushed by the solidification front.

With hot rolling of a wedge sample the temperature and the deformation step when the steel became sensitive to hot cracks were determined. Edge cross cracks appeared in the temperature range between 1100 °C and 1150 °C at around a 30 % step of deformation. Inside the hot-rolled samples microcracks were observed at the austenite and $\delta$-ferrite boundaries, where the segregation of sulphur was observed, also.

Key words: austenitic stainless steel, continuous casting, solidification microstructure, $\delta$-ferrite, grain-boundary cracks, hot workability, influence of impurities

# MATERIALI IN TEHNOLOGIJE

MATERIALS AND TECHNOLOGY

Letnik / Volume 41 2007

ISSN 1580-2949


IMT Ljubljana, Lepi pot 11, 1000 Ljubljana, Slovenija

# MATERIALI IN TEHNOLOGIJE / MATERIALS AND TECHNOLOGY

## VSEBINA / CONTENTS
## LETNIK / VOLUME 41, 2007/1, 2, 3, 4, 5, 6

# MATERIALI IN TEHNOLOGIJE / MATERIALS AND TECHNOLOGY

## AVTORSKO KAZALO / AUTHOR INDEX

## LETNIK / VOLUME 41, 2007, A–Ž

# MATERIALI IN TEHNOLOGIJE / MATERIALS AND TECHNOLOGY

# VSEBINSKO KAZALO / SUBJECT INDEX

# LETNIK / VOLUME 41, 2007

### Jubileji – Jubilee



### Kovinski materiali – Metallic materials

LETNO KAZALO – INDEX

**Anorganski materiali – Inorganic materials**



**Vakuumska tehnika – Vacuum technique**



**Gradbeni materiali – Materials in civil engineering**

**Informatika – Informatics**